Creating Warm Dense Matter and Studying Structural Properties

Nicholas John Hartley

St. Cross College

University of Oxford

A thesis submitted for the degree of

Doctor of Philosophy

Hilary term, 2015

Dedicated to the memory
of Molly Hartley

Creating Warm Dense Matter and Studying Structural Properties

Nicholas John Hartley

St. Cross College, University of Oxford

A thesis submitted for the Degree of Doctor of Philosophy

Hilary term, 2014

Abstract

Warm dense matter is an area of the phase diagram between solids and classical plasmas, but poorly described by theoretical descriptions of both. Collective oscillations and quantum effects all play significant roles in its structural behaviour and equations of state. Aside from its complexity, work on this state is significant as a stepping stone towards achieving energetically viable nuclear fusion, as well as representing a laboratory analogue for planetary cores and other astrophysical phenomena.

X-ray scattering, using beams from X-ray free electron lasers, is used to probe the structure of samples in this state, and is shown to compare well to theoretical descriptions. Angle-resolved scattering showed sharper than expected peaks, suggesting stronger interparticle correlation than expected. Using the beam in self-seeded mode, scattering from ion acoustic waves in warm dense matter was observed for the first time, confirming theoretical descriptions of the phenomena but raising further questions due to an elastic peak in the spectra. Similar experiments in the future will allow models of ionic behaviour to be tested directly, and potentially determine the source of this feature.

X-ray diffraction was used to study the evolution of samples heated by proton, electron or photon irradiation, with the aim of resolving the temperature evolution of the species within the sample. The results suggest that, although the behaviour in metallic samples is well described by low-temperature approximations, that of graphite is more complex and does not agree with the models available.

Acknowledgements

First and foremost my thanks must go to my supervisor, Gianluca Gregori. The opportunites that he has afforded me during my time as a DPhil student have been immensely valuable, and it is only with his help and support that the work I have carried out has been possible.

I would also like to thank Tom White; I can honestly say that, without your presence in the group, the previous three years would have been less enjoyable and this thesis would be significantly shorter. Similarly, my gratitude to my postdocs Chris and Hugo, who taught me many of the things I should probably already have known before starting a practical DPhil course. My thanks also to my fellow students, both those in the same research group - Paul, James, Joe, Jena and Pawel (and Alex and Matt, however briefly I worked with you) - and not - Shamim, Paul, Dave, James, Chris and the Davids M and R. I have enjoyed working with all of you, and your knowledge and help has been valuable throughout my time at Oxford.

Much of this work has been carried out as part of collaboration, and so my thanks go to the many scientists around the world that I have been fortunate enough to work with. Special thanks to Paul Neumayer, who led my first collaborative experiment, and Siegfried Glenzer, with whom I first worked on LCLS, but also to all the others that are too numerous to list here.

Finally, my thanks to my family for their unfailing love and support throughout my university career and beyond.

Role of the author in this work

The work in this thesis comprises experimental and theoretical results relevant to the state of warm dense matter, and high energy density physics in general. Much of the work has been carried out as part of callaborative efforts, and so this section will endeavour to clarify the extent of the author's contributions to the work presented.

Chapter 1 is an introductory chapter, reviewing the physics background to some of the work contained in the thesis. It is consequently not novel, and sources used are identified in the text.

Chapter 2 is a largely theoretical chapter, and the definitions for the structure factors are taken from the identified sources, as is the description of molecular dynamics. The final part of the chapter, looking at memory functions, was carried out with the help of J. Mithen and B. Crowley, under the guidance of G. Gregori, and comprises work carried out by the author in evaluating dynamic structure factors under this approach and comparing it to others.

Chapter 3 presents results from two experiments on the Linac Coherent Light Source. The first, looking at the static structure factor, was proposed by P. Neumayer, who was principal investigator for the experiment. The author was a collaborator on the experiment and carried out analysis on the diffraction and scattering data as it was collected, with further analysis after the experiment led by P. Neumayer. The second measured the ion fluctuations in a dense plasma for the first time, in an experimental campaign conceived by G. Gregori and proposed by J. Hastings. The campaign was led by J. Hastings and G. Monaco, with the author participating as part of a significant international collaboration. Analysis of the data has been led by G. Monaco, with work in Oxford centring on reproducing the data obtained with theoretical approaches including OF-DFT, by T.White, and with hydrodynamics, which the author has carried out for this thesis.

Chapter 4 is again theoretical, presenting results from different cited sources relating to the rate of electron-ion energy exchange in energetic samples. These were used to develop computational methods to analyse experimental data, specifically that from the Titan experiment presented in Chapter 5.

Chapter 5, after describing well-known methods using a variety of cited sources, presents results from four experiments:

- Temperature equilibration in proton-heated graphite. This experiment, conceived by G. Gregori and performed on the Titan laser, took place in 2011 and consequently before the author joined this research group. The analysis

was performed by T. White, and published in Scientific Reports (White *et al.* [170]); it is included here as context for the following experiments.

- Temperature equilibration in electron-heated graphite. This experiment was conceived by G. Gregori, P. Neumayer and T.White, aiming to follow on from the Titan experiment. It was performed on the PHELIX laser in 2012, with the author working as part of the experimental team led by P. Neumayer, being responsible for target construction. The author also participated in the analysis, led by T. White, which was published in Physical Review Letters (White *et al.* [167]).

- Temperature equilibration in laser-irradiated gold nanofoils. This experiment was conceived by A. Higginbotham and carried out on the TW Ti:Sapphire laser in the HEDP laboratory in Oxford in 2013, with an experimental team consisting primarily of the author and T. White. The author also participated in the analysis published in Physical Review B (White *et al.* [168]).

- Temperature equilibration in proton-heated tantalum. This experiment was conveived by G. Gregori, T. White and the author, and performed on the Titan laser. The experimental team of seven people was led by the author, who also performed the analysis published in HEDP (Hartley *et al.* [73]).

As part of the research culminating in this thesis, the author has had the opportunity to participate in a number of further experimental campaigns, leading to co-authorship of a number of other articles. A complete list of publications involving the author is given in Appendix C.

Contents

1 Introduction **1**

1.1 Warm Dense Matter 2

1.1.1 Laser Developments 5

1.2 X-ray Diagnostics 7

1.3 Structure of the Thesis 11

2 Ion Dynamics **13**

2.1 Introduction 13

2.2 Distribution Functions 13

2.2.1 Time Dependence 15

2.3 Molecular Dynamics 18

2.3.1 Concepts of MD 18

2.3.2 Choice of Potential 20

2.3.3 Density Functional Theory 21

2.4 Memory Functions 23

2.4.1 Modelling the Memory Function 26

2.4.2 Memory Functions - Results 30

2.5 Conclusions 33

3 FEL Results **35**

3.1 Introduction 35

3.2 XFELs and LCLS 35

3.3 MEC L592 - Static Structure Factor 39

3.4 MEC L708 - Dynamic Structure Factor 45

3.4.1 MD Analysis 48

3.4.2 Hydrodynamic Analysis 51

3.5 Conclusions 55

4 Temperature Equilibration **57**

4.1 Context . . . 57
4.2 Two Temperature Model . . . 58
4.3 Forms for $G(T_e)$ . . . 60
4.3.1 Metallic Relaxation . . . 60
4.3.2 Landau-Spitzer Theorem . . . 63
4.3.3 Quantum Statistical Approaches . . . 66
4.4 Conclusions . . . 69

5 Equilibration Results **71**
5.1 Experimental Methods . . . 71
5.1.1 X-ray Line Radiation . . . 71
5.1.2 Target Normal Sheath Acceleration . . . 72
5.1.3 Debye-Waller Effect . . . 74
5.2 Experiments . . . 80
5.2.1 Titan - August 2011 . . . 80
5.2.2 PHELIX - May 2012 . . . 83
5.2.3 Oxford Lab - October 2012 . . . 85
5.2.4 Titan - August 2013 . . . 90
5.3 Conclusions . . . 100

6 Conclusions and Further Work **103**

A Thermostats in Molecular Dynamics **106**
A.1 Velocity Rescaling . . . 106
A.2 Nosé-Hoover Thermostat . . . 108
A.3 Langevin Dynamics . . . 111

B Laser Driven Compression **113**

C List of Publications **115**

Chapter 1

Introduction

The mid-1990s saw a milestone in laser technology; for the first time, a beam with a peak power exceeding the entire global power output was fired. Focussed down onto micron sized spots, this allowed conditions otherwise only found in the interiors of massive planets or in the heart of nuclear explosions to be created and studied in the laboratory. Even now, nearly two decades on, the physics and behaviour of such systems is poorly understood and there is still a huge amount to learn.

The extreme conditions generated by the interactions of such high power beams with matter are now generally considered to be part of a broad area of research known as High Energy Density Physics. This is encompasses physics from fields as diverse as plasma physics, condensed matter, astrophysics, fusion energy and laser physics among others. One definition [127], from the National Plasma Science Committee, puts it as referring to any system or material with an energy density above 10^{11} J m^{-3}, equivalent to a pressure on the order of 1 Mbar. Such pressures are comparable to the internal energy of a hydrogen atom, and so it is at this energy that solid density matter begins to show significant compression.

The impetus for studying such systems comes a variety of sources. Since the partial adoption of the comprehensive nuclear test ban treaty, nuclear detonations as a way to study generate these conditions are not possible and so using other methods to probe the behaviour of matter under these conditions, and benchmark computational codes, has been eagerly seized upon[119]. Many of the largest laser facilities, such as the Orion laser at AWE, LMJ in France and the NIF in California, were funded partly or primarily with the goal of stockpile maintenance.

Another rapidly growing area within HEDP is the study of laboratory astrophysics. Much of this relies on using scaling laws [28] to relate high energy phenomena in the laboratory to astrophysical analogues - this can include shocks [51], supernovae

[132], magnetic fields [103] and many more. Work can also be carried out to better understand the behaviour of the matter inside stars and exoplanets [104] [112]. With thousands of planets already found [142], but generally little more than their mass and radius known, being able to take their densities and extrapolate the possible behaviour of the material within them gives a far greater insight than is otherwise possible.

Perhaps most excitingly, though, work is ongoing to create energetically viable nuclear fusion as a source for energy generation. Work at the National Ignition Facility has seen results edge ever closer to the break even point [81], and much of the progress has been through the greater understanding of the material behaviour [88] under the phenomenal energy flux of the 192 beamlines.

1.1 Warm Dense Matter

The work in this thesis is largely concerned with a particular state within the more general definition of high energy density physics, known as warm dense matter (WDM). The properties, both equilibrium and dynamic, have been studied throughout this work, and so before proceeding a definition of this state will be attempted. Such a definition is complicated by the fact that is is generally described negatively, in that it is neither a solid nor a plasma. We can consider the coupling constant Γ for a sample to be the ratio of the Coulomb potential between the ions to their kinetic, or thermal, energy [37], such that:

$$\Gamma = \frac{\text{PE}}{\text{KE}} = \frac{Q^2}{4\pi\varepsilon_0 a} \times \frac{1}{k_B T} \tag{1.1}$$

with Q the charge on an ion in the sample, ε_0 the permittivity of free space and a the average ion separation.

Using this expression, we can see that a solid will have $\Gamma \gg 1$ as the interionic potential energy is much greater than the ion kinetic energies. At the other extreme, an ideal gas or plasma assumes no interaction between the constituent particles, giving $\Gamma \ll 1$ for the sparse samples that these models reproduce well. Between these extremes, we find the warm dense state. With densities ranging from 0.1 - 1000 g/cc, and temperatures within a factor 10 of 1 eV, it has $\Gamma \sim 1$, meaning that the simplifying assumptions that are so important for describing solid and gaseous samples are no longer valid. Instead, entirely different approaches are needed, with neither energy

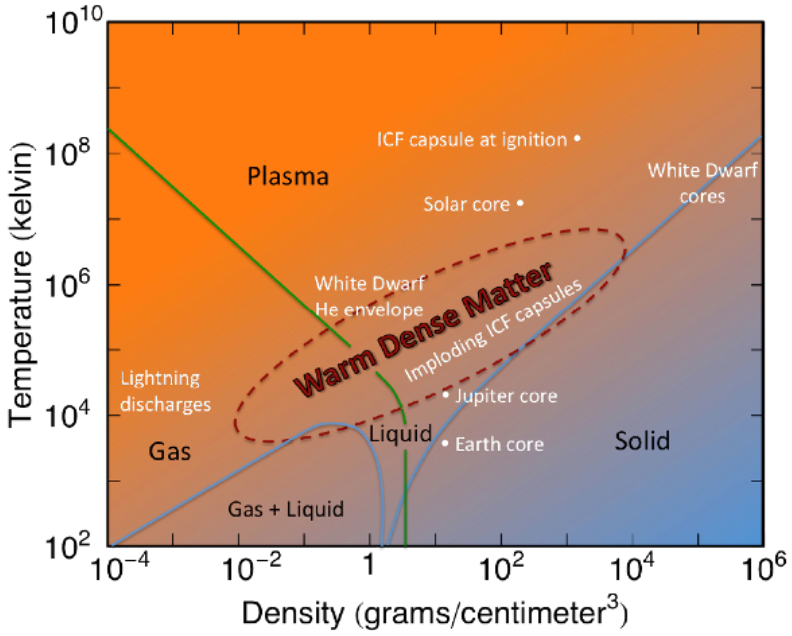

Figure 1.1: Temperature-density phase diagram, showing the relationship of warm dense matter to other well-known states. Reproduced from Los Alamos National Laboratory (lanl.gov).

treated perturbatively, and with electron degeneracy and non-equilibrium species temperatures properly dealt with. For these reasons, much of the most successful work has been computational rather than analytic [16].

Figure 1.1 shows how this state relates to better understood states, and indicates some of the systems that the results are relevant to. We can see that planetary cores, especially of larger, Jovian planets, fall within this range, motivating the study of iron [165] and silicates [147], as well as lighter elements [174][113] found in the gassy envelopes about the high density cores in white dwarf stars and other stellar remnants. In inertial confinement fusion experiments, the deuterium-tritium capsule passes through the warm dense state *en route* to potential ignition in a 'hot dense' state [97], and so understanding WDM is important for modelling the instabilities and energy transfer in this transient state [93].

The warm dense states studied here are, without the mass of a planet or similar to contain it, naturally going to expand or explode outwards, and so creation of the samples has to happen over very short timescales, which is generally done either by compression or heating. Much of the work on (cold) compressed matter uses diamond anvil cells, or other static compression techniques. These techniques, however, cannot reach the pressures of HEDP and so instead, dynamic compression techniques using an

intense shock driven into the material must be used; early experiments used gas guns and flier plates to reach pressures approaching 10 Mbar, and underground nuclear tests created matter with pressures up to 100 Mbar. Now, however, such shock driven experiments typically use energetic laser pulses to drive a shock through a sample. Similar sources can also be used to directly heat a sample, or to create charged particle beams to give secondary heating, methods which are described in more detail later.

Within samples like this, where there is a significant degree of ionization, the behaviour of the electrons relative to the ions is worth considering. Outside of the very hottest samples, or lightest elements, many of the electrons will remain bound to the ions in their orbitals, a complication rarely considered in plasma theory and a source of complexity in modelling the electron-ion interaction, as we will see when we look at density functional theory and molecular dynamics in Chapter 3.

The complexity of the free electrons is very different again. The first quantity to define is that of the plasma frequency, this being the frequency of collective excitations set up due to instantaneous electric fields within the plasma. Such a field will displace electrons from their equilibrium positions, driving a harmonic oscillation with characteristic frequency

$$\omega_{pe} = \sqrt{\frac{n_e e^2}{m_e \varepsilon_0}} \tag{1.2}$$

Before going further into the electronic behaviour, we will note that such an oscillation also exists from the ion species, with a correspondingly lower frequency equal to

$$\omega_{pi} = \sqrt{\frac{n_i (Z_f e)^2}{m_i \varepsilon_0}} \tag{1.3}$$

with Z_f the degree of ionization of the ions. In the section on ion dynamics, this quantity is sometimes referred to as ω_p in the assumption of the one-component plasma.

Apart from the collective oscillations, the other primary driver of the electron behaviour is the presence of the ions. While the ions can, under the Born-Oppenheimer assumption, be considered to be stationary on the timescale of the electron motion, the field surrounding them exerts a great effect, unlike in an ideal plasma where there is considered to be no direct interparticle interaction. The effect of the ion fields is to cause the electrons to cluster around the ions, screening the Coulomb force between the charges over long distances. The length scale above which such an effect is

significant is the Debye length, equal to

$$\lambda_D = \sqrt{\frac{\varepsilon_0 k_B T_e}{n_e e^2}} \tag{1.4}$$

The corresponding Debye number, N_D, equal to the average number of electrons within a sphere of radius λ_D centred on a given ion, serves as another measure of the extent to which a plasma can be approximated as an ideal plasma. For an ideal plasma, $N_D \gg 1$, as they have heavily populated Debye spheres, meaning that there is almost no Coulomb interaction between the ions due to the electronic screening, an effect known as quasi-neutrality. The dense plasmas considered here, on the other hand, have very few electrons within this radius such that significant interionic forces remain. The electrons do still exert some screening, however, and so the interaction is often described by a Yukawa potential:

$$V_{scr} = \frac{Z_f e^2}{4\pi\varepsilon_0 r} e^{-r/\lambda_D} \tag{1.5}$$

Potentials of this form appear again in the discussion on classical molecular dynamics, as ways to better approximate WDM behaviour within those models.

1.1.1 Laser Developments

Much of the work in this field relies on very high energy and intensity laser sources. These generally fall into one of two broad categories, both of which are relevant for the work presented in this thesis:

- high energy lasers, with long (ns) pulse lengths, used for shock compression of samples
- high power lasers, amplified by CPA with ps-fs pulse lengths, used to drive charged particle beams or atomic transitions as X-ray sources

As the development of laser technology played such an important role in allowing access to the systems studied here, a brief overview of some of the developments in laser technology will be given.

Since the first laser was built in 1960 by T H Maiman [100], the technology has advanced in leaps and bounds, with the peak intensities reaching 10^{19} in the mid-1990s [9] and now even exceeding 10^{20} W/cm^2, as shown in Figure 1.2. Early improvements included Q-switching [101] and modelocking [71], both of which allowed systems to

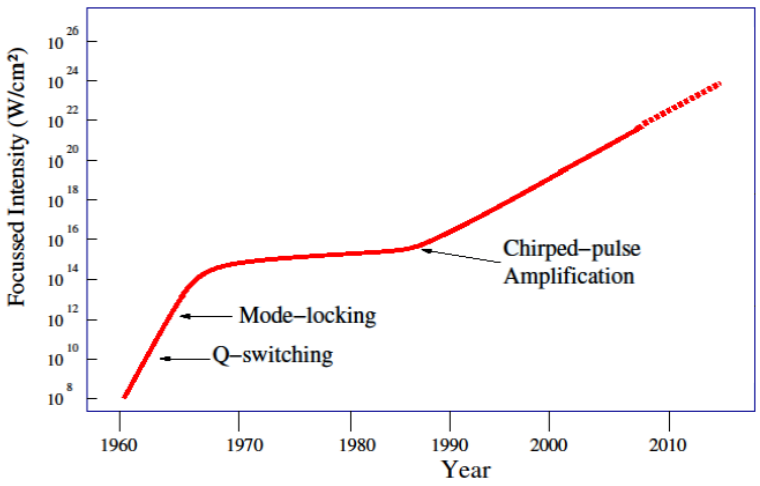

Figure 1.2: History of peak laser intensity, with significant developments highlighted. The continuing rise from the development of CPA is clear. Figure reproduced from [91].

move away from continuous wave (CW) laser operation to pulsed power, allowing access to irradiance on the order of 10^{13} W/cm^2.

Possibly the biggest breakthrough, though, was the development of chirped pulse amplification. Prior to this, reaching higher laser intensities was inhibited by the effects of non-linear processes such as self focussing in the gain medium, which would both damage the laser and ruin the beam quality. Originally used for increasing the power of radar, CPA works by stretching the beam in time. This can be done with prisms or gratings, giving an optical element with different path lengths for different wavelengths, giving a typical increase in pulse length of $\sim 10^4$ from the original. For a fs beam, stretching to $\sim$ 100 ps requires a path difference on the order of cm to give the required 'chirp'.

This longer pulse can be amplified, with the beam able to contain much more energy without reaching the intensities that causes self-focussing and other non-linear effects. After amplification, it can be passed through a compressor, with the opposite path difference to the stretcher, to reproduce the original fs beam duration with far more energy, and consequently power, than is otherwise possible[150]. Such approaches are now used in almost all of the largest laser systems, and are continuing to allow access to ever higher peak laser powers.

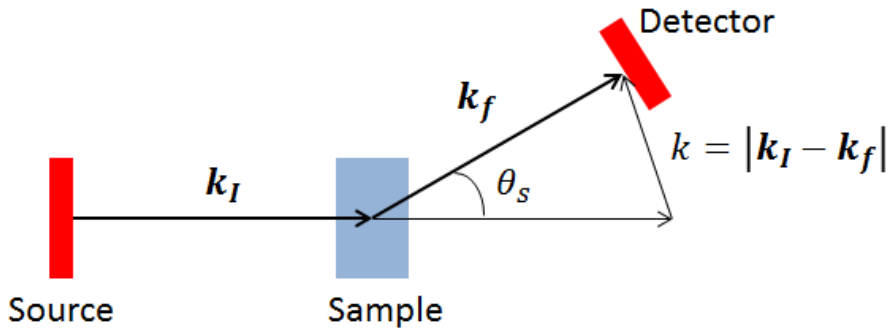

Figure 1.3: Schematic of a typical X-ray scattering experiment.

1.2 X-ray Diagnostics

While high power optical lasers are necessary to create many the HED systems, much of the diagnostic workload, at least in the work of this thesis, relies on X-rays. The utility of X-rays for probing matter in the warm dense state comes from the fact that their wavelengths, on the order of 0.1-10 Å, are comparable to the inter-ionic distance. Consequently, the X-ray Thomson Scattering (XRTS) diagnostic described here is frequently in experiments on dense plasmas [89] and compressed matter [87]. For the same reason, energetic neutrons with de Broglie wavelengths on a similar scale are frequently used, and much of the early work on the structure within liquids was derived for work on neutron scattering, see e.g. [69].

For the experiments considered here, a schematic of which is shown in Figure 1.3, the x-rays are generated by either an X-ray free electron laser (XFEL) or a laser driven source, the details of which will be given later in Chapters 3 and 5, respectively.

An incoming beam of X-rays of energy E_0, wavelength λ_0 and wavevector $k_I = 2\pi/\lambda$ are incident on a sample, and are scattered through an angle θ_s, being left with energy E_F and wavevector k_F. The values that control the scattering are then the transferred energy and momentum: $E = E_0 - E_F = \hbar\omega$ and $\hbar k = \hbar|\,\mathbf{k}_I - \mathbf{k}_F|$, where the vector nature of k can be ignored for warm dense samples because they are isotropic. In the low energy (non-relativistic) limit, there is a simple relationship between the momentum transfer and scattering angle such that:

$$\hbar k = 2\hbar|\mathbf{k}_I| \sin\left(\frac{\theta_s}{2}\right) \tag{1.6a}$$

$$= \hbar\frac{4\pi}{\lambda_0} \sin\left(\frac{\theta_s}{2}\right) \tag{1.6b}$$

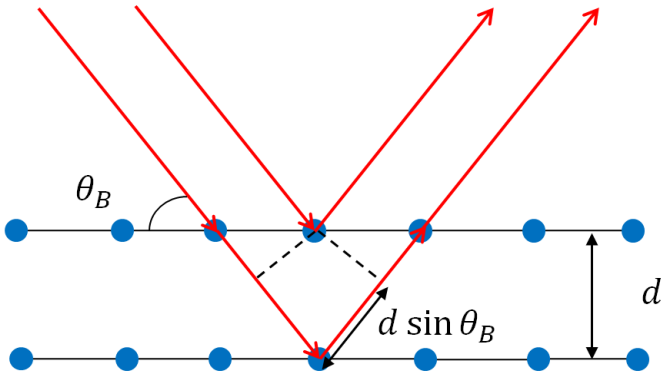

Figure 1.4: Representation of Bragg diffraction. For the scattered rays to interfere coherently, the paths must satisfy the Bragg relation $n\lambda = 2d \sin \theta_B$.

Scattering occurs when an electron is accelerated by the electric field on an incoming photon, causing it to oscillate and emit light with, to a first approximation, the same energy. If the frequency of the incoming photon is significantly higher than any characteristic resonance frequencies of the atom, which is true for the 'hard' X-rays ($E_0 \gtrsim 1$ keV) which are used here, the scattering cross section per unit solid angle $d\Omega$ is:

$$\frac{d\sigma_T}{d\Omega} = \left(\frac{e^2}{4\pi\varepsilon_0 m_e c^2} \right)^2 \frac{1 + \cos^2 \theta_s}{2} \tag{1.7}$$

Integrating over the solid angle gives an expression for the Thomson cross section value:

$$\sigma_T = \frac{8\pi}{3} \left(e^2 4\pi\varepsilon_0 m_e c^2 \right)^2 \tag{1.8}$$

$$= \frac{8\pi}{3} r_e^2 \tag{1.9}$$

$$= 6.652... \times 10^{-25} \text{cm}^2 \tag{1.10}$$

which can be seen to be proportional to the square of the classical electron radius r_e. With such a low cross section, obtaining sufficient signal is difficult, even with the very bright sources available from free electron lasers.

A much simpler case, and one that gives a much brighter signal, is from the interaction of X-rays with a crystalline solid. In this case, the scattering from the bound electrons will, at particular angular displacements, interfere constructively to give a very strong signal. In the simplest formalism, we merely require that the path difference between the scattered light from the top layer of a crystal, and that of the next layer, shown in Figure 1.4, is equal to an integer number of wavelengths such

that they waves intefere constructively:

$$n\lambda = 2d\sin(\theta_B) \tag{1.11}$$

with d the lattice parameter and n the order of the diffraction. Other properties of the signal derived from Bragg diffraction will be discussed at the start of Chapter 5, as it is an important diagnostic for the experiments described there.

Returning to the general case, we want to know how to link the scattering spectrum to the structure of the sample that is being probed. We first note that the scattered power is proportional to the structure factor of the electrons in the material [145]:

$$\frac{d^2\sigma}{d\Omega d\omega} \propto S_{ee}(k,\omega) \tag{1.12}$$

The precise definition of the structure factor will be given later in the thesis, but in qualitative terms it is given by the Fourier transform of the time-dependent positions of the particles in the sample. In the case of the Bragg diffraction given above, the positions are a series of δ-functions and so the Fourier transform is similarly restricted to sharp peaks at particular values.

We are interested in the electron structure factor (rather than that of the ions, or of the entire sample) because the strength of scattering from a particle is inversely proportional to its mass, and so the effect of the ions is negligible. A widely used approximation for the quantity has it split into three separate terms, as described by Chihara [25]:

$$\begin{aligned} S_{ee}(k,\omega) =& |f(k)+q(k)|^2 S_{ii}(k) + Z_f S^0_{ee}(k,\omega) \\ &+ Z_b \int S_{ce}(k,\omega-\omega')\, S_s(k,\omega')\, dw' \end{aligned} \tag{1.13}$$

This gives the electron correlations in terms of three distinct effects. The first term describes the electrons whose movement is correlated with that of the ions, as the term $S_{ii}(k,\omega)$ is the ion-ion structure factor. The prefactor consists of the form factor $f(k)$, describing the reciprocal positions of the bound electrons around the nucleus, and the screening factor $q(k)$ describing the effect of the screening cloud. One assumption which is frequently made in work using this expression [61, 65] is to assume that this term is entirely elastic and that therefore $S_{ii}(k,\omega) = S_{ii}(k)\delta(\omega)$. However, the work on warm dense matter described in this thesis is primarily concerned with ion motion and dynamics, and so this term will prove to be of most interest to us.

The second term describes the dynamic structure factor of the free electrons in the system, with Z_f the average degree of ionization. The main feature of this is the

collective oscillations, known as plasmons, at frequency ω_{pe} as explained earlier. These give rise to up- and down-shifted energy peaks in scattered spectra as the incoming photon scatters from a collective mode. The height of these peaks is modified by the effect of 'detailed balance': the occupation of electron modes in the sample follows a Bose-Einstein distribution, and at the temperatures considered in the warm dense regime the higher energy states are likely to be sparsely occupied. Consequently, there are few excited plasmons which could potentially lose energy in a scattering interaction, but many possible zero-energy states which can be excited, giving a much stronger down- than up-shifted signal.

The final term describes transitions between bound states and the free electrons, with the quantity Z_b the average number of bound electrons in each ion. This term is frequently ignored in XRTS experiments, as it tends to be significantly smaller than the other two terms, or adds a small contribution to the downshifted peak. It does become more significant in denser plasmas, and plasmas of heavier ions, where there is a strong dependence on the degree of continuum lowering. This phenomenon, described by Stewart and Pyatt [149] and others [178], is still poorly understood, although there is increasing interest in research to better explain the behaviour[48],[26].

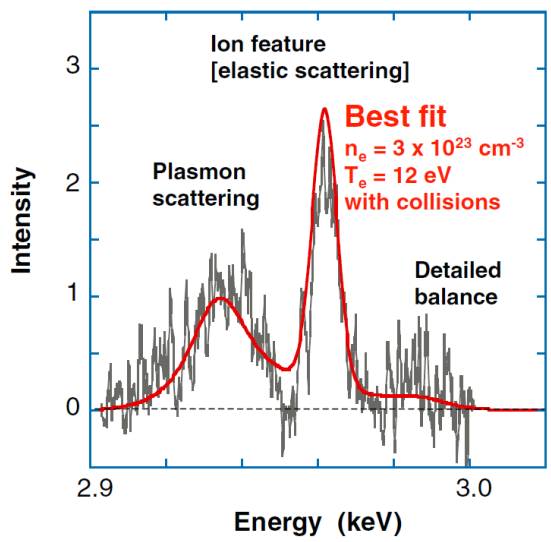

Figure 1.5: XRTS spectrum showing the pseudo-elastic central peak, from the ions, and the shifted plasmon peaks from the electron species.

An example of the kind of spectrum that Equation (1.13) describes is given in Figure 1.5, taken from the paper by S. Glenzer [59] which first demonstrated the observation of plasmons in warm dense matter. The central peak is scattering from the electrons that move with the ions, and does not exhibit any significant shift from the original Cl Lyman-α energy at 2.96 keV. The peaks on either side are due to interactions with the collective electron oscillations, with the down-shifted peak favoured due to the principle of detailed balance described above.

It is also interesting to look at the range of possible inelastic processes present in X-ray - matter interactions, which are shown in Figure 1.6. One further

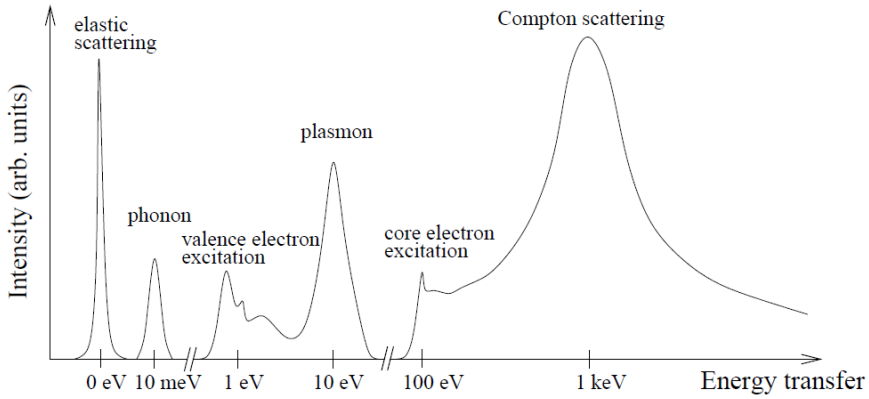

Figure 1.6: Inelastic interactions of X-rays with matter, with order of magnitude values for the energy shifts, taken from the thesis of S. Galambosi [55].

distinction to be made is how these different shifts depend on the angle of scattering being observed; in general, we can characterise a process as either collective or non-collective depending on the relationship between the length scale and the scattering k value [42]. Single-particle processes like Compton scattering become important for $ka > 1$, while the collective effects of plasmons and phonons are important for $ka < 1$, where a the Wigner-Seitz unit radius [171] for the system i.e. the average ion separation, taken as a typical length scale.

XRTS can be used as a diagnostic for the temperature and density of a sample ([58][56][77]). One such method, and that used in Chapter 3 of this work, is done by measurements of the Compton peak, the properties of which depend strongly on the temperature and density of the system [60].

1.3 Structure of the Thesis

The main body of the thesis is divided between two major themes. The first looks in much greater detail at the structural properties of warm dense matter, with Chapter 2 starting by deriving definitions for the structure factors, which were mentioned briefly above. Although such derivations are common to any work on fluids or liquids, their inclusion here is to highlight their significance in describing the equilibrium properties of warm dense systems. It continues with an introduction to molecular dynamics, an important method for modelling these systems and extracting computational values for the structure factors under a variety of different assumptions. It concludes with a very different approach to calculating structure factors, based on a wholly analytical

model originally developed for fluids but shown to work in dense plasmas such as those studied here.

The theme of ion dynamics and structure is continued in Chapter 3, which begins with an overview of the operation of X-ray free electron lasers, the development of which has revolutionised the study of solid density materials such as these. Results from two different experiments on the LCLS facility are then presented. One looks at the static structure factor resolved over a wide range of angles, as well illustrating how XRTS can be used as a diagnostic for the density and temperature of a sample. The other experiment studied the dynamic structure factor with unprecedented energy resolution, allowing the ion acoustic peaks to be resolved. This is in contrast to the pseudo-elastic assumption in the XRTS description above, and represents the first observation of such a phenomenon in warm dense matter. The chapter, and this section of the thesis, concludes by comparing the results to theoretical and computational values, and discussing possible sources of error.

The latter half of the thesis looks at temperature equilibration in solid and warm dense samples. Chapter 4 outlines the motivation for better understanding the temperature equilibration in such samples, then describes the formalism used to describe the temperature evolution in the samples studied, as well as the assumptions made in doing so, and their validity. It continues by giving the derivations for the rates of energy exchange and temperature equilibration under different methods, as well as discussing the materials and conditions for which they are appropriate.

Before presenting the results of the experimental campaign, Chapter 5 outlines some of the experimental and analytical methods used to obtain said results. The experiments themselves are then presented, in chronological order, with the campaigns on Titan (2011) and Phelix (2012) looking at results from graphite, and those at Oxford and Titan (2013) mainly concerned with metallic samples. Analysis is presented alongside each set of results, and the chapter culminates with some overall conclusions from the entire body of work.

Finally, the final chapter reviews the work presented, drawing final conclusions and suggesting possible directions for future work.

Chapter 2

Ion Dynamics

2.1 Introduction

As described in the Introduction, using X-rays to study systems with densities comparable to or greater than those of solid materials has a variety of advantages. In lower temperature cases, where the original solid crystalline structure is still intact, this is frequently done by diffraction. In higher temperature systems, the crystal structure has been lost and there is no long range order within the system and consequently we instead see incoherent scattering, with much lower intensity. The angular and spectral variation of the scattered radiation is then contained within the static and dynamic structure factors, respectively.

In this chapter, we will start by looking at the definitions and derivations of these values, to show how they relate the behaviour of the ions to the functions which can be measured in experiments. We will then look at ways of evaluating the structure factors, first using simulations of the particles within a system, and then using an analytic approach based around the memory function formalism for hydrodynamics.

2.2 Distribution Functions

What differentiates the states studied herein from those described by well understood classical plasma dynamics, and what is at the root of their difficulty to model, is the presence of short range order between the ions within the system. This is generally considered to be a defining property for liquid structures, and we will see that in fact many aspects of hydrodynamics are appropriate for these descriptions.

The level of structural order in a static system is contained within the radial distribution function $g(\mathbf{r})$ which, in isotropic systems, can be generalised to the pair

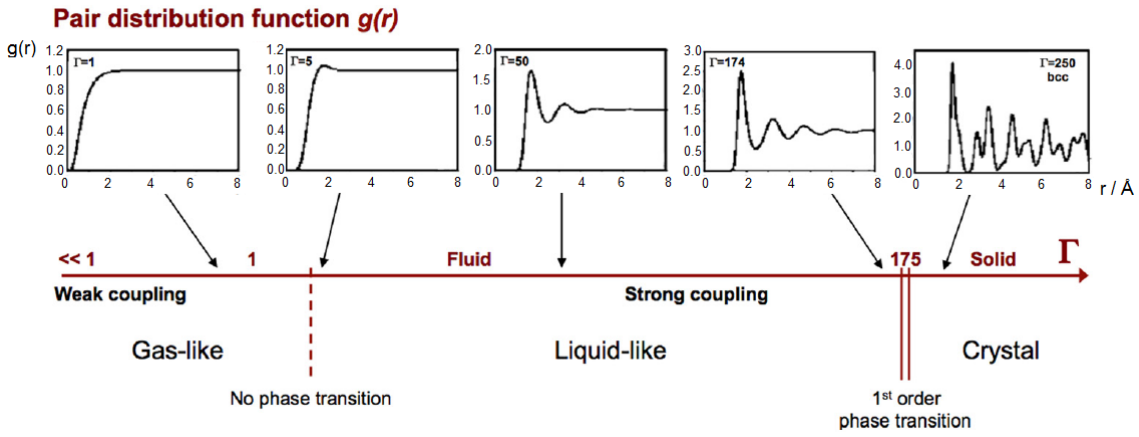

Figure 2.1: *Radial distribution functions from systems with increasingly strong inter-particle coupling. Reproduced from Ma et al. [98].*

distribution function $g(r)$. This quantity can be thought of as describing the probability of finding another ion at a distance r from a nominal reference ion at $r = 0$, although a fuller derivation will be given later in the chapter. The number of ions contained in a spherical shell of thickness dr is then:

$$N_{shell} = 4\pi n \int_{r}^{r+\delta r} r^2 g(r) dr \tag{2.1}$$

Distribution functions from systems with different coupling strengths are shown in Figure 2.1. The ones of greatest interest here are those in the strong coupled, liquid-like regime, which exhibit several significant characteristic features. What is perhaps easiest to explain is the zero-valued region at low values of r. Whereas in an ideal gas the function takes a constant value of unity for all values of r, as the positions of any two atoms exhibit no correlation, in this state the interionic interactions are significant, and so the repulsive Coulomb force means that the probability of two atoms being in close proximity is very small.

Moving to larger radii, we see a broad peak in the function, centred about the mean separation value. Here again, we can compare to an ideal state; in a zero temperature solid, the function would consist of a series of sharp peaks, with each atom found very close to its position in the crystal lattice. Instead, warm dense systems have much weaker correlations, which decrease to a gas-like constant value for large r, beyond a few times the mean separation. Indeed, this is very similar to a liquid structure, with broad peaks corresponding to loosely correlated 'shells' of ions, giving way to no correlation at all ($g(r) = 1$) at large r.

In general, the pair distribution function is important in describing such non-ideal systems because a variety of different thermodynamic quantities can be expressed as integrals over it. The simplest is, of course, the number of ions in the system which is fairly easily seen to be

$$N = 1 + \int_V g(\mathbf{r}) d\mathbf{r} \tag{2.2}$$

$$= 1 + 4\pi \int_V r^2 g(r) dr \tag{2.3}$$

However, similar expressions exist for the average energy of the ions, by integrating over a product of $g(r)$ with the potential $v(r)$, and for the pressure. Another quantity that can be calculated is the compressibility χ_T, defined as [22]:

$$1 + 4\pi\rho \int r^2 \left[g(r) - 1\right] dr = \rho k_B T \chi_T \tag{2.4}$$

The significance of this particular approach to describing non-ideal plasmas, as opposed to any other, is that $g(r)$ can be easily derived from experimental results, and so models of it verified. The quantity directly measured in x-ray or neutron scattering experiments is the static structure factor (SSF), which is the one-dimensional Fourier transform of the pair distribution function and therefore depends on $k = 2\pi/r$:

$$S(k) = 1 + 4\pi\rho \int r^2 g(r) \frac{\sin kr}{kr} dr \tag{2.5}$$

It can be seen that, if we obtain the values of this function over a range of k-values, this allows us to derive all of the macroscopic properties of the system, including that on the equation of state (EOS), one of the main drivers behind such experiments. We also note that the limit of $S(k)$ for $k \to 0$ can be derived from (2.4) and is [67]:

$$S(0) = \rho k_B T \chi_T = \chi_T / \chi_T^0 \tag{2.6}$$

where $\chi_T^0 = \beta/\rho$ is the compressibility of an ideal gas. This quantity, which is not easily estimated, can therefore be directly extracted from a measurement of the low-k limit of the static structure factor.

2.2.1 Time Dependence

While many properties of the system can be usefully studied in a wholly static case, it is only natural to try and extend our description to account for time dependence in the system. If the pair distribution function $g(r)$ described above is taken to describe

the correlations in the (point particle) density between two points in the system, it is easy to see that we can equally look for a similar function that describes density correlations at points separated by time instead. If we then take the Fourier transform of this, we would again expect to find a quantity that can be experimentally measured, as we did with the static structure factor before.

This extension of $g(r)$ to include both space and time is known as the Van Hove function [158]. If the Fourier transform of this is taken, now in time rather than space, we obtain the dynamic structure factor (DSF) which is a quantity of prime importance throughout this work. The additional frequency dependence of this quantity compared to the earlier static structure factor manifests as an energy shift in scattered light, which can be observed by spectral resolution.

To fully describe these quantities, we need to begin with the formal definition of a time correlation function for dynamical variables; that is, variables that are functions of any or all of the particle coordinates $\mathbf{r}_i$ and momenta $\mathbf{p}_i$. For this case, a time dependent correlation function C_{AB} is defined as

$$C_{AB}(t', t'') = \langle A(t')B^*(t'')\rangle \tag{2.7a}$$

$$C_{AB}(t) = \langle A(t)B^*(0)\rangle \tag{2.7b}$$

where $\langle\cdot\rangle$ denote an equilibrium, or thermal, average over the given ensemble, and the second expression is obtained by putting $t'' = t' + t$, which can be done as an equilibrium average is, by definition, invariant under time translation. For the correlation functions of interest here, we always have $A = B$ such that these are autocorrelation functions - we are, for instance, interested in how the density at one point in space and time changes and affects the density at another point.

If we now consider the simplest dynamical variable, the microscopic number density, we start by writing it as

$$n(\mathbf{r}, t) = \sum_{i=1}^{N} \delta(\mathbf{r} - \mathbf{r}_i(t)) \tag{2.8}$$

We can use this expression in (2.7a) to obtain an equilibrium density-density time correlation function

$$G(\mathbf{r}, \mathbf{r}', t) = \frac{1}{N}\langle n(\mathbf{r}' + \mathbf{r}, t)n(\mathbf{r}', 0)\rangle \tag{2.9}$$

As we are working in a homogeneous system, we can integrate over the variable $\mathbf{r}'$ with no loss of generality, obtaining the time and space dependent distribution

function - the van Hove function referred to above.

$$G(\mathbf{r},t) = \frac{1}{N}\left\langle \int n(\mathbf{r}'+\mathbf{r},t)n(\mathbf{r}',0)d\mathbf{r}' \right\rangle \tag{2.10}$$

$$= \frac{1}{N}\left\langle \sum_{i=1}^{N}\sum_{j=1}^{N} \delta[\mathbf{r}+\mathbf{r}_j(0)-\mathbf{r}_i(t)] \right\rangle \tag{2.11}$$

We can also look at the zero time value, which serves as a formal definition of the radial distribution function as it is the spatial correlation with no time difference.

$$G(r,0) = \frac{1}{N}\left\langle \sum_{i=1}^{N}\sum_{j=1}^{N} \delta[\mathbf{r}+\mathbf{r}_j(0)-\mathbf{r}_i(0)] \right\rangle \tag{2.12}$$

$$= \delta(\mathbf{r}) + ng(\mathbf{r}) \tag{2.13}$$

To move from the definition for density autocorrelation in real space to the values in experimental results, we know that we need to move to Fourier space. We begin by taking the Fourier components of the number density

$$n(\mathbf{k},t) = \int \exp(-i\mathbf{k}\cdot\mathbf{r})n(\mathbf{r})d\mathbf{r} \tag{2.14}$$

Returning to the definition of a general correlation function in (2.7a), we can choose

$$A = B = \frac{1}{\sqrt{N}}n(\mathbf{k},t) \tag{2.15}$$

Substituting this, we find:

$$F(\mathbf{k},t) = \frac{1}{N}\langle n(\mathbf{k},t)n(-\mathbf{k},0)\rangle \tag{2.16a}$$

$$= \int G(\mathbf{r},t)\exp(-i\mathbf{k}\cdot\mathbf{r})d\mathbf{r} \tag{2.16b}$$

The function $F(\mathbf{k},t)$ is the intermediate scattering function, and the relationship in (2.16b) can be shown for correlation functions in general by e.g. Hansen [69]. This quantity is of great significance, because it can now be related to the dynamic structure factor (DSF) which, as mentioned earlier, is the generalization of the static structure factor to include frequency dependence. We can now ignore the vector nature of $\mathbf{k}$, because the systems dealt with in this work are isotropic, so we find the following expression for the DSF:

$$S(k,\omega) = \frac{1}{2\pi}\int_{-\infty}^{\infty} F(k,t)\exp(i\omega t)dt \tag{2.17}$$

$$= \frac{1}{2\pi}\int d\mathbf{r}\int_{-\infty}^{\infty} dt\, G(\mathbf{r},t)\exp(-i\mathbf{k}\cdot\mathbf{r})\exp(i\omega t) \tag{2.18}$$

We have now defined the quantity that is of greatest importance to this section of the thesis, with this equation showing clearly how it is uniquely defined by, and uniquely defines, the density correlation function, and consequently the equilibrium behaviour of the system. However, it is also worth pointing out further properties before proceeding to look at models for calculating it. Integrating the DSF over all frequencies, which in an experiment would be equivalent to measuring the scattered light without spectral resolution, gives, by Fourier inversion of (2.17)

$$\int_{-\infty}^{\infty} S(k,\omega)d\omega = F(k,0) \tag{2.19}$$

We can then return to the general definition of a time correlation function in (2.7a) and, by taking a zero time value, obtain a new definition of the static structure factor.

$$F(k,0) = \frac{1}{N}\langle n(k,0)n(-k,0)\rangle \tag{2.20}$$

$$= S(k) \tag{2.21}$$

This shows that, as had previously been stated, the static structure factor is proportional to the total scattered light at a given angle.

2.3 Molecular Dynamics

One of the primary ways that values for the structure factors in this thesis have been calculated is through the use of molecular dynamics (MD) simulations. This allows the behaviour of a system at known density, pressure and ionization to be simulated and values for a variety of different material properties to be obtained [31]. This section will first qualitatively describe how such a simulation is carried out, and consider some of the ways in which it can be made to model physical systems.

2.3.1 Concepts of MD

In the simplest terms, modelling a material using an MD simulation consists of solving the equations of motion for N particles with defined masses and a given interaction potential. Although beguilingly simple, this method can reproduce much complex behaviour and allow insight into regimes which are difficult or even impossible to probe experimentally.

For an N-body system, the (Newtonian) equations of motion can be written as

$$\begin{aligned} m\ddot{\mathbf{r}}_i &= \mathbf{F}_i(t) \\ i &= \{1...N\} \end{aligned} \tag{2.22}$$

with the force dependant on the positions of all the other particles in the system and given by

$$\mathbf{F}_i(t) = -\nabla_i \sum_{i \neq j}^{N} v(r_{ij}) \tag{2.23}$$

where $v(r_{ij})$ is the interaction potential between the particles $\{i, j\}$. The idea behind such a process is diagrammatically explained in Figure 2.2, where the effect of the forces is used to evolve the position, which then causes the force between the particles to change.

For evolving the particle positions, the forces need to be converted into a motion with an integration algorithm. The simplest example would be an Euler method

$$\begin{aligned} \mathbf{r}_i(t + \Delta t) &= \mathbf{r}_i(t) + \mathbf{v}_i(t)\Delta t \\ \mathbf{v}_i(t + \Delta t) &= \mathbf{v}_i(t) + \frac{\mathbf{F}_i(t)}{m}\Delta t \end{aligned} \tag{2.24}$$

This is a first order method, such that the error scales as Δt - completely unsuitable for large-scale simulations which huge numbers of timesteps such as these. An improvement is the leapfrog method

$$\begin{aligned} \mathbf{r}_i(t) &= \mathbf{r}_i(t - \Delta t) + \mathbf{v}_i(t - \frac{\Delta t}{2})\Delta t \\ \mathbf{v}_i(t + \frac{\Delta t}{2}) &= \mathbf{v}_i(t - \frac{\Delta t}{2}) + \frac{\mathbf{F}_i(t)}{m}\Delta t \end{aligned} \tag{2.25}$$

Although similar, it is a second order method with error scaling as $(\Delta t)^2$, and is more suitable for oscillatory simulations. Instead, a more generalised version of methods such as this, known as Verlet integration, has been utilised in our MD simulations.

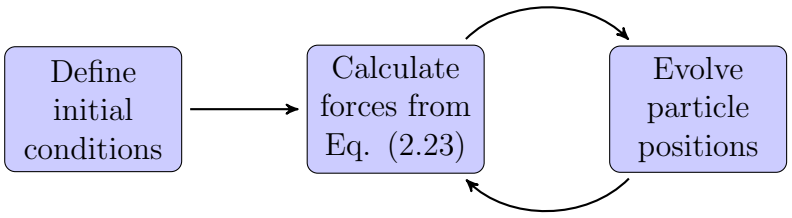

Figure 2.2: Diagrammattic representation of MD simulation

By considering a Taylor expansion in time around the particle position, we obtain the following expressions.

$$\begin{aligned}
\mathbf{r}_i(t+\Delta t) &= \mathbf{r}_i(t) + \mathbf{v}_i(t)\Delta t + \frac{\mathbf{F}_i(t)}{2m}\Delta t^2 + \frac{\dddot{\mathbf{r}}_i(t)}{3!}\Delta t^3 + \mathcal{O}(\Delta t^4) \\
\mathbf{r}_i(t-\Delta t) &= \mathbf{r}_i(t) - \mathbf{v}_i(t)\Delta t + \frac{\mathbf{F}_i(t)}{2m}\Delta t^2 - \frac{\dddot{\mathbf{r}}_i(t)}{3!}\Delta t^3 + \mathcal{O}(\Delta t^4) \\
\mathbf{r}_i(t+\Delta t) &\approx 2\mathbf{r}_i(t) - \mathbf{r}_i(t-\Delta t) + \frac{\mathbf{F}_i(t)}{m}\Delta t^2
\end{aligned} \tag{2.26}$$

Such a method is frequently used in simulations as a balance between speed of computation and fidelity to real systems.

Since these methods are based on the Newtonian equations of motion they will, by definition, maintain the total energy of the system. Although at first glance this seems both obvious and necessary, it in fact makes them a worse model in some cases. This is because many of the systems that are modelled using MD are not isolated systems, but can instead exchange energy, and often mass as well, with the surroundings. Consequently, a system at constant temperature, rather than energy, is frequently a better model. This can be achieved by applying a thermostat to the system. There are various models for this, which are discussed in Appendix 1, and results from them considered as part of the experimental analysis in the following chapter.

From the results of these simulations, values for the structure factors in which we are interested can be calculated. This was done using a program written in the Python scripting language by T. White as part of his thesis work. This evaluates the discrete Fourier transforms in space for each position timestep within the output from an MD simulation, giving the intermediate scattering function, then performs a discrete Fourier transform in time to obtain the dynamic structure factor. The presence of numerical noise at high time values in the ISF is generally smoothed out, a process which, as shown by Mithen [105], does not affect the final result but acts as a high frequency filter.

2.3.2 Choice of Potential

In modelling a dense plasma, the choice of interparticle potential makes a significant difference to the results obtained [82]. The simplest potential is the Coulomb potential - the point particles of the simulation are identical positive ions with charge $+Z_f e$, with e the charge on an electron, and mass M, such that the force between them is:

$$v(r_{ij}) = \frac{(Z_f e)^2}{r} \tag{2.27}$$

The most significant omission in this approach is, of course, the electrons, and consequently this approach is referred to as the one component plasma (OCP) model. To neutralize the positive ions, the electrons can be assumed to take the form of a uniform background which is not explicitly considered in the calculation. Such an approach is not, in most cases, realistic and the electrons can instead be assumed to cluster towards the positive ions, acting as a screening cloud around them. This adds an additional decay term to the potential, which now takes the form:

$$v(r_{ij}) = \frac{(Z_f e)^2}{r} e^{-\kappa r} \tag{2.28}$$

κ is a screening constant: it can take the value of the Debye length, in plasmas closer to ideal plasmas (low Γ), or the Thomas-Fermi screening length for more degenerate systems. Potentials of this form are described, in general, as Yukawa potentials, and plasmas modelled as such referred to as screened OCP (SOCP) or Yukawa OCP (YOCP).

One further modification suggested in recent work ([173]) is to use the Yukawa potential with an additional short-range repulsion term to account for the strong repulsive force due to overlapping $1s$ orbitals at small separations. This potential now also depends on the total nuclear charge Z_c, and takes the form

$$v(r_{ij}) = \left[\frac{(Z_f e)^2}{r} + \frac{(Z_c^2 - Z_f^2)e^2}{r} e^{-br} \right] e^{-\kappa r} \tag{2.29}$$

This has shown better agreement with full DFT simulations for calculating both static [173] and dynamic [159] structure factors, as well as agreeing with experimental results [98].

2.3.3 Density Functional Theory

Before looking at a very different approach to the calculation, the DFT calculations referred to in the previous section will be discussed in more detail. Although some such simulations have been run as part of this work, using the ABINIT software package [62][157], the lion's share have been of the simpler MD form with the potentials described. However, the use of DFT simulations to benchmark these simpler results is necessary for their use, and so a brief qualitative description of this method is given.

The basic idea behind the density functional theory method, when deployed alongside molecular dynamics, is that the potentials between particle pairs are recalculated at each time step, rather than taking fixed values as described above. This is done

by finding the approximate ground state solution of the Schrödinger equation for the many body electron system:

$$\hat{H}\Phi = \left[\hat{T} + \hat{V}_{ne} + \hat{V}_{ee}\right]\Phi \tag{2.30}$$

$$= E\Phi \tag{2.31}$$

with $\hat{H}$ the total energy operator, decomposed as the sum of the kinetic energy operator $\hat{T}$, the electron-nucleus interaction potential $\hat{V}_{ne}$ and the electron-electron interaction potential $\hat{V}_{ee}$. The expected value of the energy in a state Φ can then be written as

$$E = \frac{\langle\Phi|\hat{H}|\Phi\rangle}{\langle\Phi|\Phi\rangle} \tag{2.32}$$

In the ground state, this energy takes the minimum value with respect to allowed wavefunctions. Consequently, we can consider this in terms of the variational principle and look for the point at which $\delta E[\phi] = 0$. Such a minimization procedure, while technically possible, proves to be exceptionally difficult for any but the simplest system. In DFT, what is used instead of a wavefunction is a functional of the electron density.

Consequently, the operators for the kinetic energy and interparticle potentiasl can be written as functionals of the electron density with no loss of generality i.e. $\hat{T} = T[n_e]$, $\hat{V}_{en} = V_{en}[n_e]$. The simplest term is that due to the nuclear potential, $V_{en}[n_e]$, as under the Born-Oppenheimer approximation the nuclei are assumed to be static on the timescale of the electron motion, and so this is equivalent to a fixed background field.

In Kohn-Sham DFT [86] the kinetic energy term is expressed in terms of the wavefunctions of a fictitious system - the Kohn-Sham system - of non-interacting particles moving in an effective potential. Although these wavefunction solutions have little explicit physical meaning, it reduces the problem from a calculation in terms of 3N spatial coordinates to only 3 spatial coordinates.

The effective potential used in these calculations contains not only the effect of the (static) background ions, but also terms accoutning for the electron-electron effects. The inter-electron term can be further decomposed into a classical Coulomb interaction between the electrons $V_H[n_e]$, known as the Hartree energy, and the exchange correlation $V_{xc}[n_e]$ that includes all many-particle interaction contributions.

If an initial ansatz is taken for $n_e(\mathbf{r})$, the effective potential can be calculated, assuming an appropriate model for the exchange correlation term. This allows values for the occupations of thefictional Kohn-Sham orbitals to be found, yielding the total

energy and a new value for $n_e(\mathbf{r})$. This process is then iterated to find the minimum for the total energy.

This process does rely heavily on the form of the exchange correlation used, and models for this are still an active area of research [72]. The simplest form, known as the local density approximation (LDA), is exact for a homogeneous electron gas and assumes that the value on the functional depends only on the density at the point of evaluation:

$$E_{xc}^{LDA}[n_e] = \int \epsilon_{xc}(n_e) n(\mathbf{r}) d\mathbf{r}$$

This has shown significant success in modelling, despite the simple assumptions behind it, and is often the best approach to reproduce behaviour in solids.

Another broad group of approaches are the generalised gradient approximations (GGA) which, while still local, account for the gradient of the density as well as the value:

$$E_{xc}^{GGA}[n_e] = \int \epsilon_{xc}(n_e, \nabla n_e) n(\mathbf{r}) d\mathbf{r}$$

Such methods have shown significant improvements over the LDA for explaining, among other things, the binding energy and geometry of molecules, and consequently it enjoys a wide use in MD work on quantum chemistry.

While numerous functionals exist for such work, further discussion will be curtailed as the use of DFT in this work has been limited. A better review of exchange correlations in condensed matter systems can be found in Kurth, Perdew and Blaha [90].

2.4 Memory Functions

We now turn to a very different approach to describing the behaviour of ion dynamics in warm dense systems. Rather than modelling the behaviour of the electrons and ions in the system over an array of timesteps, we consider the system as a fluid, and apply a hydrodynamic description to it. This is most appropriate, in the nomenclature of XRTS, in situations where $ka \ll 1$ such that the length scales probed are much longer than the screening length. However, work by James Mithen [106] has suggested that such a description could remain valid for a wider range of k values.

The approach described here relies on memory functions. While these can, in principle, be used for any correlation function, we are concerned here with the behaviour of density correlation functions. For consistency of notation, therefore, we will follow the work of Ranganathan & Yip [129], itself based on the series of papers

by Hansen and others [54][68][128][70], and consider the behaviour of the intermediate scattering function $F(k,t)$, defined such that its Fourier transform is the dynamic structure factor. The Fourier transform can also be described as the real part of the Laplace transform $\tilde{F}(k,s)$ with an appropriate value for s

$$\begin{aligned} S(k,\omega) &= \frac{1}{2\pi}\int_{-\infty}^{\infty} dt\, e^{i\omega t}F(k,t) \\ &= \frac{1}{\pi}\Re\left[\tilde{F}(k,s)\right]_{s=-i\omega} \end{aligned} \tag{2.33}$$

We can define the memory function of $F(k,t)$, which we will call $M(k,t)$, by

$$\frac{\partial F(k,t)}{\partial t} = -\int_0^t dt' M(k,t-t')F(k,t') \tag{2.34}$$

with the intial condition required for closure found from the definition in (2.33)

$$F(k,0) = \int_{-\infty}^{\infty} d\omega S(k,\omega) \equiv S(k) \tag{2.35}$$

which is of course the static structure factor of the system. The definition of the memory function chosen in (2.34) shows that the instantaneous evolution of the system is entirely determined by a convolution of the historical states of the system with the memory function. It is also the case that defining either the memory function or the correlation function uniquely defines the other; a fact which becomes obvious when the equation is transformed into Laplace space using known identities, with the $\sim$ indicating transformed values:

$$\frac{\partial F(k,t)}{\partial t} = -\int_0^t dt' M(k,t-t')F(k,t') \tag{2.36}$$

$$s\tilde{F}(k,s) - F(k,0) = -\tilde{M}(k,s)\tilde{F}(k,s) \tag{2.37}$$

$$\tilde{F}(k,s) = \frac{F(k,0)}{s+\tilde{M}(k,s)} \tag{2.38}$$

This same definition for the memory function of a functional of the system can then be applied again, such that we take the memory function of $M(k,t)$ in the same way, giving a second-order memory function, defined as $N(k,t)$:

$$\tilde{M}(k,s) = \frac{M(k,0)}{s+\tilde{N}(k,s)} \tag{2.39}$$

with the closure condition found to be

$$M(k,0) = \int_{-\infty}^{\infty} d\omega M(k,\omega) \tag{2.40}$$

$$= \int_{-\infty}^{\infty} d\omega \frac{w^2 S(k,\omega)}{S(k)} \tag{2.41}$$

$$\equiv \frac{\Omega_2(k)}{S(k)} \tag{2.42}$$

This also serves as the definition of the general moment of $S(k,\omega)$ as

$$\Omega_n(k) = \int_{-\infty}^{\infty} d\omega\, \omega^n S(k,\omega) \tag{2.43}$$

By combining the definitions in (2.33),(2.36),(2.39) we can obtain an expression for the DSF in terms of either the first- or second-order memory function:

$$S(k,\omega) = \frac{1}{\pi} \frac{\frac{\Omega_2}{S(k)} N'(k,\omega)}{\left[\omega^2 - \frac{\Omega_2}{S(k)} - \omega N''(k,\omega)\right]^2 + \left[\omega N'(k,\omega)\right]^2} \tag{2.44}$$

$$= \frac{1}{\pi} \frac{M'(k,\omega)}{\left[\omega - M''(k,\omega)\right]^2 + \left[M'(k,\omega)\right]^2} \tag{2.45}$$

with the $'$ and $''$ indicating the real and imaginary parts of the Laplace transform, respectively. This equation is in fact identical to the generalised hydrodynamic description of the dynamic structure factor in a fluid, if we allow $N(k,\omega) = k^2\phi(k,\omega)$, motivated by the fact that such a substitution allows the memory function $\phi(k,\omega)$ to play the role of a 'generalised viscosity'. This can be shown using approaches to the DSF from the macroscopic Navier-Stokes equations, and can be seen in work by e.g. Mithen [108].

Before moving on to the specific description of the ansatz used in this work, and the approximations made to allow it to be analytically modelled, it is worth noting how the dynamic structure factor derived here relates to those derived from other approaches. Significantly, the same equation reproduced as (2.44) above can instead be found from the definition of the density response function (DRF) in the memory function approach:

$$\chi(k,\omega) = \frac{k^2 n/m}{\omega^2 - \frac{\Omega_2(k)}{S(k)} + i\omega k^2 \phi(k,\omega)} \tag{2.46}$$

dependant on the ion number density n and mass m.

This can then be used in the fluctuation-dissipation theorem, which links the response of the system and the DSF.

$$S(k,\omega) = -\frac{k_b T}{\pi n \omega} \Im(\chi(k,\omega)) \tag{2.47}$$

An alternative way to describe such systems, and one which has previously been used to some success in systems such as quantum electron gases, is to use local field corrections (LFCs) to extend the description of an ideal gas to include the non-ideal effects which play such an important role in these denser systems. In this approach, the response function is written as:

$$\chi(k,\omega) = \frac{\chi_0(k,\omega)}{1 - v(k)\left[1 - G(k,\omega)\right]\chi_0(k,\omega)} \tag{2.48}$$

$$\chi_0(k,\omega) = -\frac{n}{k_B T} Z\left(\sqrt{\frac{m}{2k_B T}}\frac{\omega}{k}\right) \tag{2.49}$$

Within this description, χ_0 is the density response function of an ideal gas and $Z(x) = [1 - 2xD(x)] + i\sqrt{\pi}x\exp(-x^2)$ with the Dawson function defined as $D(x) = \exp(-x^2)\int_0^x \exp(y^2)dy$. We also have $v(k) = 4\pi(Ze)^2/k^2$ is the Fourier transform of the Coulomb potential.

With $G(k,\omega) = 0$ you return to the mean field approximation, which only works well to describe systems with $\Gamma \ll 1$. Although models for $G(k,\omega)$ exist which allow it to better match observed results at higher Γ, they are generally significantly more complex than memory functions which produce similarly good results. Consequently, this line of enquiry was not pursued further in this work, and results using such methods are not presented.

2.4.1 Modelling the Memory Function

Returning to the memory function approach, we see in the work by Hansen that results from MD simulations of the one-component plasma are well-reproduced with a Gaussian second order memory function [70]. Due to the success of this approach, it has also been adopted here:

$$N(k,t) = N(k,0)\exp(-\pi t^2/4\tau_k) \tag{2.50}$$

$$= \left[\frac{\Omega_2}{\Omega_4} - \frac{\Omega_2}{S(k)}\right]\exp(-\pi t^2/4\tau_k) \tag{2.51}$$

For convenience, we will denote $\Omega_P^2 = \frac{\Omega_2}{\Omega_4} - \frac{\Omega_2}{S(k)}$

From this ansatz, we apply a Laplace transform to obtain values for the real and imaginary parts of the memory function.

$$N'(k,\omega) = \Omega_P^2 \tau_k e^{-\tau_k^2 \omega^2/\pi} \tag{2.52}$$

$$N''(k,\omega) = \frac{2\tau_k}{\sqrt{\pi}} \Omega_P^2 D(\tau_k \omega/\sqrt{\pi}) \tag{2.53}$$

where $D(x)$ is the Dawson function used in the LFC description at the end of the previous section.

This leaves us with two quantities as yet undefined: the fourth moment of the DSF, Ω_4, and the characteristic 'relaxation' time for the ansatz chosen, τ_k. The first of these is well-known[6], and is written as:

$$\Omega_4 = 3\Omega_2^2 + \Omega_2 \left[1 - I(k)\right] \tag{2.54}$$

An additional term due to quantum effects omitted here as the effect is negligible on the systems considered. The term $I(k)$ is the short wavelength (high k) limit of the local field correction mentioned before, and depends on the static structure factor $S(k)$:

$$I(k) = -\frac{Z}{4\pi^2 n_e} \int_0^\infty ds\, s^2 \left[S(s) - 1\right] \times \left[\frac{5}{6} - \frac{s^2}{2k^2} + \frac{(k^2 - s^2)^2}{4sk^3} \ln\left|\frac{k+s}{k-s}\right|\right] \tag{2.55}$$

The latter, the relaxation time τ_k, is constrained in order to be self-consistent within the model [66] to be:

$$\tau_k^2 = \frac{\Omega_P^2}{2\left(\frac{\Omega_6}{\Omega_2} - \frac{\Omega_4}{\Omega_2}\right)} \tag{2.56}$$

This now requires us to find an expression for the sixth moment, which is complex as exact forms are difficult to evaluate. Instead, we follow the work of Gregori & Gericke in taking an approximate form in terms of lower frequency moments [64]:

$$\Omega_6 \approx \frac{1}{3}\frac{\Omega_4^2}{\Omega_2}\left(2 + \frac{\Omega_4 \Omega_0}{\Omega_2^2}\right) \tag{2.57}$$

What we have now obtained is a description of the dynamic structure factor of a one component plasma in the memory function formalism. Unlike the work done by Mithen, we have used analytic, if approximate, expressions for the higher moments and for the relaxation time, rather than treating these as fitting parameters to match the results to those from MD simulations. However, there is still not a model included for the static structure factor $S(k)$, which is crucial not just for scaling the values in

(2.44), but also as a quantity that is integrated over in the correction factor $I(k)$ in (2.55).

From Debye-Hückel models we know that, in the small-k limit, the value of $S(k) \to 0$ as $\frac{k^2}{k^2+k_D^2}$, where k_D is the inverse Debye length. It is also the case that at large values of k the value must tend to 1. Clearly, the simplest form that fulfills both of these requirements is just the Debye model, which was derived for the long-wavelength, and therefore low-k, limit:

$$S_D(k) = \frac{k^2}{k^2 + k_D^2} \tag{2.58}$$

While this does meet both of the simple criteria, for any dense plasma the results from it are grossly inaccurate. As an additional computational difficulty, using it in the local field correction $I(k)$ gives an integrand which is proportional to k_D^2 as $k \to \infty$, and is consequently non-convergent. This problem can be overcome, without losing the correct behaviour in the low k limit, by adding an exponential term to the screening. This gives us the expression:

$$S_1(k) = \frac{k^2}{k^2 + k_D^2 \exp\left(-\frac{k^2}{k_D^2}\right)} \tag{2.59}$$

At low k the exponential term goes to 1, recovering the expression in (2.58). However, at large k the integrand decreases faster than the k^{-4} required for the term to converge. Since we maintain the low-k limit behaviour that defines the Debye model, this expression could be used without loss of generality.

We now have a convergent integral, and a model which works fairly well at small values of Γ, corresponding to large values for the Debye length and therefore smaller values of k_D. What it cannot do, however, is reproduce the static structure at high coupling strengths, where there is a characteristic peak in $S(k)$ due to the degree of order between the proximate ions. This can be added into the model with a further exponential term of the form:

$$\begin{aligned} f &= \left(\frac{k_D}{k}\right)^{2\alpha} * \left(1 - \exp\left(-\frac{k}{k_D}\right)^{2\beta}\right) \\ S_2(k) &= \frac{S_1(k)}{1 - f * S_1(k)} \end{aligned} \tag{2.60}$$

This expression produces results which agree in the low- and high-k limit, as long as $\alpha < (\beta + 2)$. In qualitative terms, as α increases the position of the correlation peak moves to small k, while increasing β gives a sharper and higher peak. However,

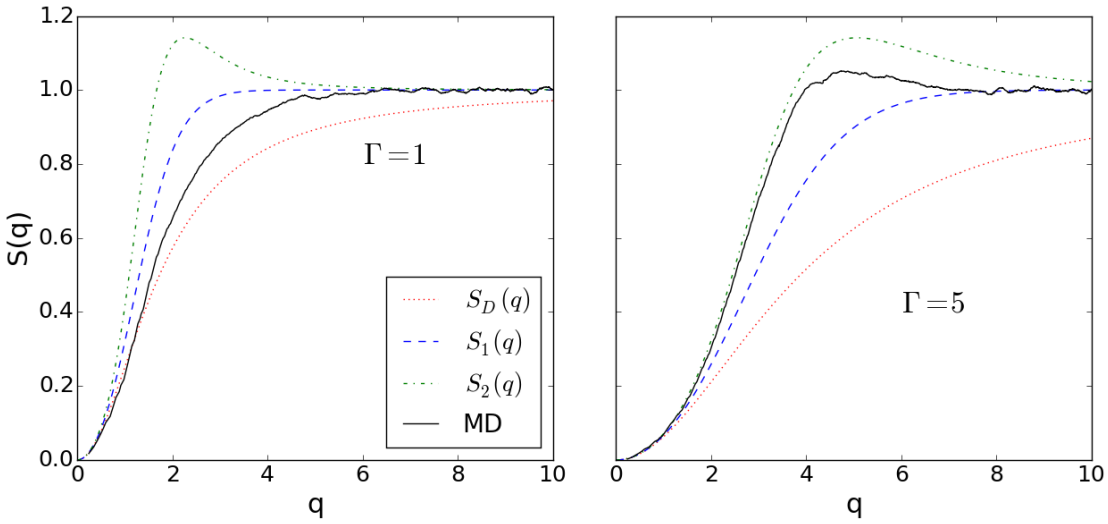

Figure 2.3: Values for the static structure factor, in terms of the dimensionless parameter $q = ka$, using the expressions in (2.58, 2.59, 2.60), with $\alpha = \beta = 1$, compared to those from MD simulations in the same coupling conditions with a Yukawa potential. It can be seen that none of the models accurately reproduce the observed shape.

the form is such that they will always contain a peak and consequently do not reduce to the simpler forms for any choice of α, β.

Results from these different approaches are given in Figure 2.3, with $\alpha = \beta = 1$ for the final model. It can be seen that at the moderate coupling values with which we are concerned it could be possible to vary the parameters to reproduce the results from MD, but that is not possible to find one single analytical model that reproduces the static structure factor in these systems, a fact which has been previously reported [14]. This is especially clear if one considers the models only in terms of the peaks in the system - none of the models presented here are capable of giving results both with and without a peak, depending on the Debye length, and consequently none are capable of spanning the entire range of conditions of interest. This problem would become even more pronounced at larger coupling strengths where the degree of interionic order results in multiple peaks.

Instead, we can still significantly reduce the computational load in calculating dynamic structure factors by using MD, or full DFT-MD, to find the static structure factor and then using this as an input for the analytic form of the dynamic structure factor obtained through the memory function formalism. This requires a much shorter simulation, as it is only needs to be sufficiently large in space to give small values of k, without also needing the long timescales to get to small w-values. We will see in

the next section that this has given good agreement with time dependent simulations with significantly higher computational cost.

Another approach to calculating structure factors analytically, which has not been considered here but is included for completeness, is using the HyperNetted Chain (HNC) equations, based on the Ornstein-Zernicke equation [120][8] for a two component plasma:

$$h_{12}(\mathbf{r}) = c_{12}(\mathbf{r}) + \sum_c n_c \int d\mathbf{r}' c_{13}(\mathbf{r}') h_{32}(|\mathbf{r} - \mathbf{r}'|) \tag{2.61}$$

with $h(r) = g(r) - 1$ the total correlation function for two particles and $c(r)$ the direct correlation function[1]. To be solved, it requires a closure relation, one choice for which is specified by the HNC approximation, giving a pair distribution function:

$$g_{ab}(r) = \exp\left(-\beta V_{ab}(r) + h_{ab}(r) - c_{ab}(r)\right) \tag{2.62}$$

Such an approach can effectively reproduce results from MD (see e.g. [13] [172], [144]) in an analytic formalism, with the same dependence on the choice on potential. HNC models were used in the following chapter for predicting the results from the experiment probing the static structure factor, but are otherwise not considered further here.

2.4.2 Memory Functions - Results

With the equations outlined in the previous section, we are now in a position to attempt to reproduce results from MD simulations. The calculations were performed in terms of dimensionless variables with $\omega' = \omega/\omega_p$ and $q = ka$, with the strong coupling constant determining the state of the system being probed.

the plasma frequency	$\omega_{pi} = \sqrt{4\pi(Ze)^2 n/m}$
the Wigner-Seitz unit radius	$a = (4\pi n/3)^{-1/3}$
the strong coupling constant	$\Gamma = Ze^2/ak_BT$

The first results give an overview of the typical values obtained, and are shown in Figure 2.4. As expected, the peak is generally centred around $\omega = \omega_p$, with a very sharp peak at small ka and broadening as it increases. The effect of the factor Γ is, in a one component plasma, mainly just to scale the variation in the k direction, as

[1] As this approach explicitly considers interparticle interactions, the term $c(r)$ describes the correlation due to direct interactions, while $h(r)$ includes the effect via through other particles in the system

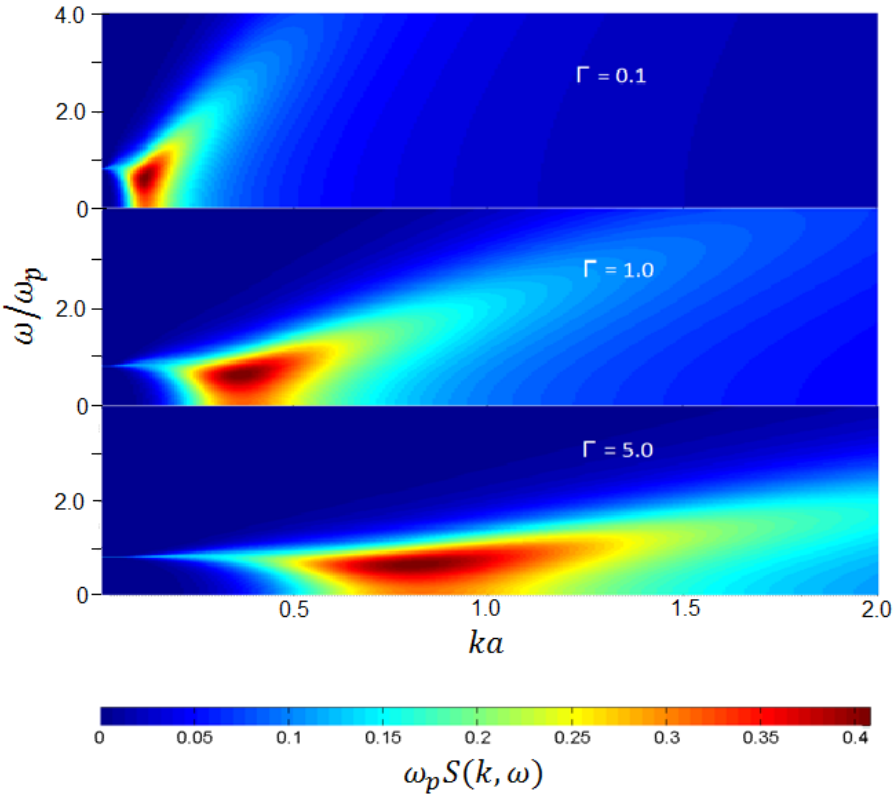

Figure 2.4: Results for the dynamic structure factor calculated using the memory function formalism described, from a range of k, ω values, with coupling strengths of $\Gamma = 0.1, 1, 5$.

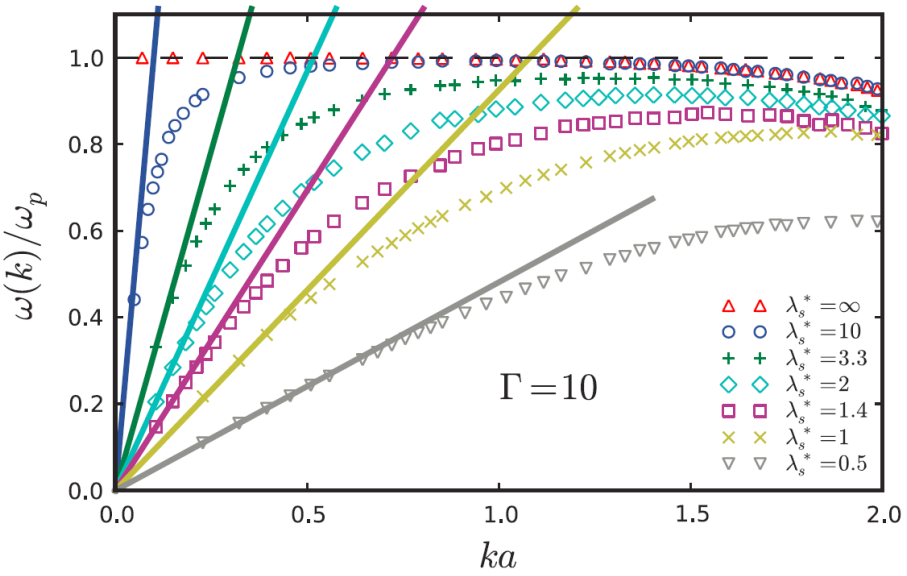

Figure 2.5: Ion acoustic peak position $\omega(k)/\omega_p$ as a function of ka in the low ka limit; symbol values are taken from MD simulations and lines from best fits for the sound speed. λ_s* is the screening length - for the OCP system considered in this work, this is infinite. Graph reproduced from Mithen [107].

there are no screening effects. For plasma models including screening effects, then as we approach $k \to 0$ we reach the limit $\omega = c_s k$ with c_s the sound speed in the material, as shown in Figure 2.5, a fact which we expect to also hold true in real WDM systems.

Although the OCP does have significant limitations for reproducing results in real systems, especially in terms of the acoustic wave behaviour at low k, it is still possible to results obtained with other systems that make the same assumption. Within an MD simulation, a purely Coulomb interionic potential can be used, and the results analysed to produce values for the DSF, as shown in Figure 2.6.

We can see that the memory function and MD results generally agree for lower ka values, and higher Γ values. As ka gets larger, the memory function continues to predict a peak which has already been lost in MD simulations. Similarly, at low Γ the results are better fitted by the random phase approximation[50], an approach which ignores strong coupling effects.

In the paper by Mithen [108] we see that with fitted values, the memory function approach can be made to agree with the results from MD simulations over a wide range of (Γ, ka) values, including those shown. What is clear from these results, however, is that the approximations made limit this range quite significantly and, not unexpectedly, work significantly better in the low-k, hydrodynamic limit. With

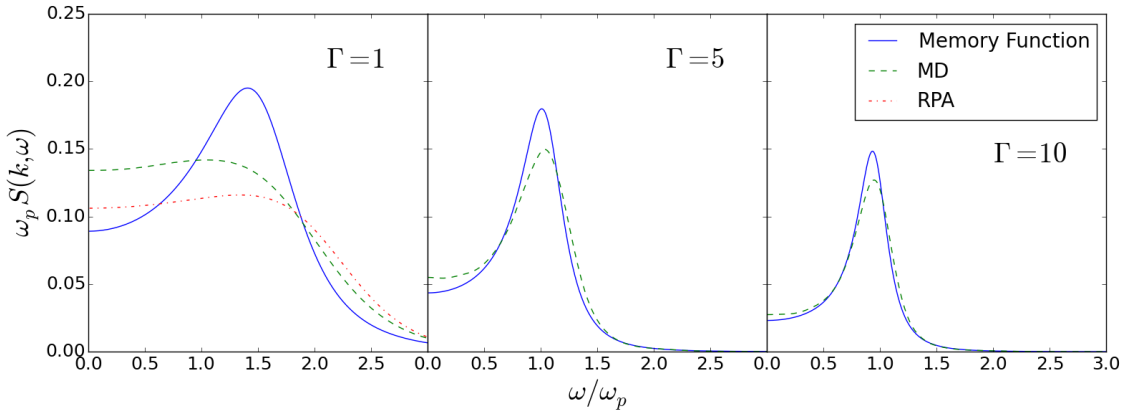

(a) Comparison of the DSF values from the memory function approach and MD calculation at the shown values of Γ, with $ka = 1.02$. Additionally, for the low coupling value $\Gamma = 1$ the random phase approximation is included for comparison.

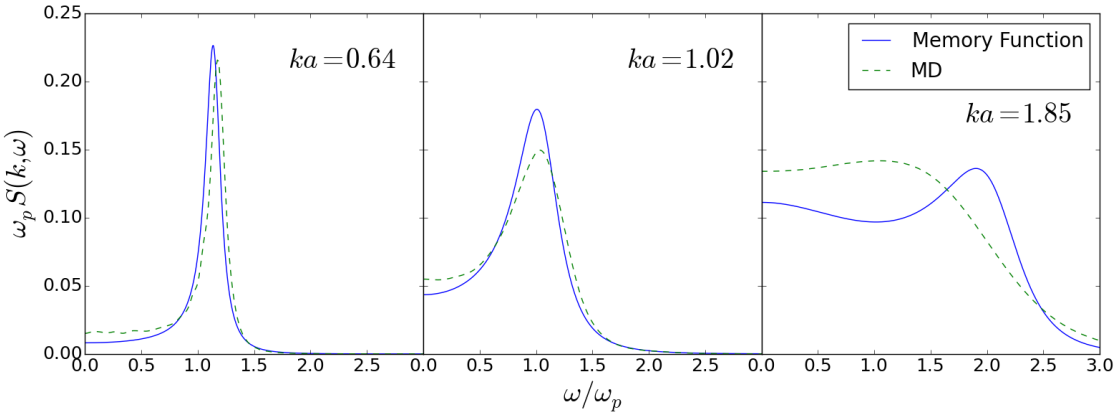

(b) Comparison of the DSF values from the memory function approach and MD calculation at the shown values of ka, with $\Gamma = 5$.

Figure 2.6: Comparison of MD and memory function results at (Γ, k) values relevant to warm dense matter.

appropriate approximations for the parameters, we would also expect to be able to obtain analytic expressions for the values with SOCP models, which would be more applicable to real systems.

2.5 Conclusions

This chapter has considered a variety of different concepts, united under the broad heading of ion dynamics. Firstly, definitions for the correlation functions in a system were derived and considered. These expressions which, although applicable to any physical system, are of interest in this work for describing the behaviour of strongly

coupled ions, codify the link between the microscopic behaviour and the spectra observed in X-ray Thomson scattering, as we will see in more detail in the next chapter.

One of the main ways in which values for these structure factors are predicted was then presented, in a description of molecular dynamics. This is a framework for modelling the behaviour of an atomic or ionic system computationally, with generally very high computational costs. This is due to the tracking and evolving of position of often very large numbers of particles, in order to probe long length scales, and many timesteps, to probe long timescales. In classical MD the interparticle interactions are described by a single potential, which can be purely Coulombic, in the case of the one component plasma, screened Coulombic, for the SOCP, or further screened with the addition of another repulsive term, which appears to give the best agreement with more comprehensive simulations.

Alternatively, DFT-MD recalculates the interparticle forces at each step as a functional of the electron density. Although significantly more accurate than classical MD, the calculation of orbital occupations increases the computational cost even further, which generally makes running sufficiently large simulations impractical.

Finally, a very different approach to calculating structure factors was described in the form of hydrodynamic memory functions. These treat the warm dense system as a liquid with the correlation functions evolving according to a convolution of their past states with the eponymous memory function. This has previously been shown to give relatively good agreement with MD results when various parameters of the model are used as fitting constants, but we saw that with models for these values chosen, agreement is restricted to a smaller area of the plasma phase space.

Chapter 3

FEL Results

3.1 Introduction

The previous chapter gave definitions for the structure factors of materials, and explained how they relate to the results obtained from XRTS diagnostics. In this chapter, results from experiments probing warm dense samples will be presented, and related to the quantities derived. Both of these experimental campaigns, one looking at the angularly-resolved static structure factor and the other at the dynamic structure factor with ultra-high energy resolution, were carried out on the LCLS facility in California. Therefore, we will start with a description of the physics of free electron lasers in general, as the advent of such sources has allowed previously impossible insight into the behaviour of dense materials (e.g. [46],[26],[75]). The results from the experiments will then be presented and discussed, and some of the attempts to model and explain the data observed will be described.

3.2 XFELs and LCLS

Prior to the development of free electron lasers capable of producing x-ray radiation, i.e. $E_\gamma \gtrsim 0.1$ keV, experiments probing structure factors in warm dense matter generally used laser produced x-ray sources. These are described in more detail in Chapter 4, as they were used for the experiments on temperature equilibration. For diffractive diagnostics these have been relatively successful, as the well-defined crystal structure allows signal to be built up coherently through Bragg diffraction. In warm dense systems, however, where there is little to no long range order, the signal from Thomson scattering is very much lower, and it is here that the radiation obtained from an XFEL is so revolutionary for this work. They can produce beams of coherent

x-rays, at a tuned wavelength and with little extra radiation or background noise. This alone gives a huge increase in contrast, but in addition the beams produced are orders of magnitude brighter than any other x-ray source available, as shown in Figure 3.1.

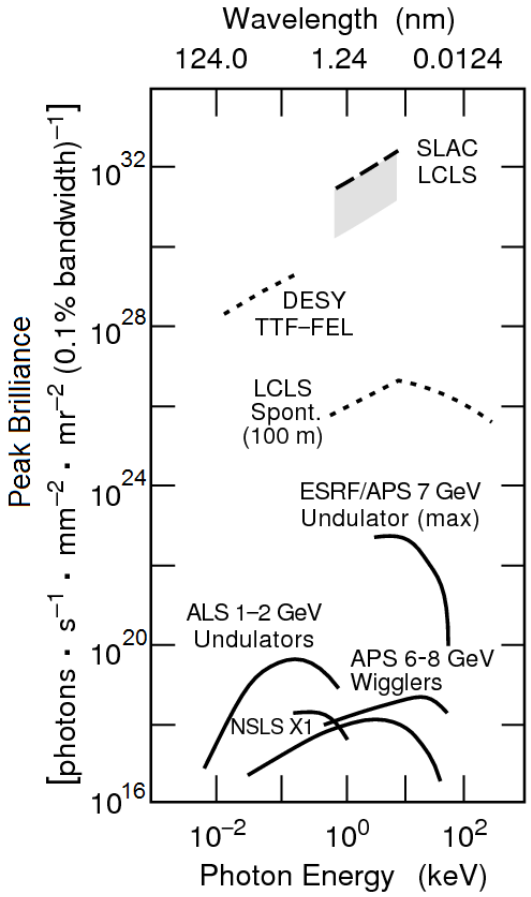

Figure 3.1: Comparison of peak spectral brightness (brilliance) - when it was first turned on, LCLS was around nine orders of magnitude brighter than any other source at x-ray energies.

Despite the name, it is not a 'laser' in the normal use of the word, as there is no gain medium from which a beam draws energy, and the stimulation of emission is radically different from that in a quantum laser. In addition, what makes the beam obtained coherent is the fact that the electrons are not 'free' at all.

However, the operation of a free electron laser is, at least in qualitative terms, relative easy to describe (a more detailed description can be found in Saldin *et al.* [138]). An electron bunch is accelerated to high energy before being passed into an oscillating magnetic field, known as an 'undulator' or 'wiggler'. This electron is forced to follow a sinusoidal path due to this field, and therefore emits energy as synchrotron radiation, as first observed in the 1940s [39]. The emission is incoherent, as the electrons are distributed randomly, but is the source of radiation in third generation light sources. The difference in FELs is that the electron beam interacts with a co-propagating photon beam of the desired wavelength, causing the electrons to form bunches with spacing equal to that of the wavelength. The radiation emitted by these electron bunches is then in phase, giving coherent radiation, like that from a conventional laser[139]. As the coherent intensity grows, it caused additional bunching, with the process continuing until it reaches saturation at a power many orders of magnitude higher than that from pure undulator emission.

The wavelength produced by an FEL, λ_0, depends on several parameters, and can be calculated by

$$\lambda_0 = \frac{\lambda_U}{2\gamma^2}\left(1 + \frac{K^2}{2}\right) \tag{3.1}$$

$$K = \frac{eB_U\lambda_U}{2\pi m_e c^2} \tag{3.2}$$

with λ_U, B_U the period length of the magnetic undulator and the peak magnetic field, respectively, and γ the relativistic factor of the electrons. The value K is known as the undulator parameter, and relates the length of the undulator period to the radius of the curve that the electron follows in the field.

It is clear from this that, by choosing the parameters of the electrons and the undulator, radiation at any desired wavelength can be produced, within the limits of the machine. In the case of optical light, the undulator can be between two mirrors, such that the light emitted is kept inside the cavity, seeding each new bunch of electrons such that the power grows to saturation over the course of multiple passes.

What we are interested in, however, is producing X-rays from such facilities. In this case, there are no effective mirrors that can be used and so the radiation much be produced over a single pass of the undulator system. This generally requires higher energies - in LCLS, the electrons are at around 10 GeV - and much longer undulator sections. In the simplest case, electrons are injected in and the initial noise from their entering the undulator is amplified over its length - so-called Self Amplified Spontaneous Emission (SASE)[3]. Although this does still produce X-ray bursts far brighter than any earlier facilities, the bandwidth is relatively large ($\sim 0.5\%$) and the temporal coherence correspondingly poor.

The challenge of producing a seed beam at such a high energy seemed immense - there were suggestions of using high harmonic generation (HHG) to produce a seed beam, which was successfully demonstrated for an FEL in the extreme ultraviolet

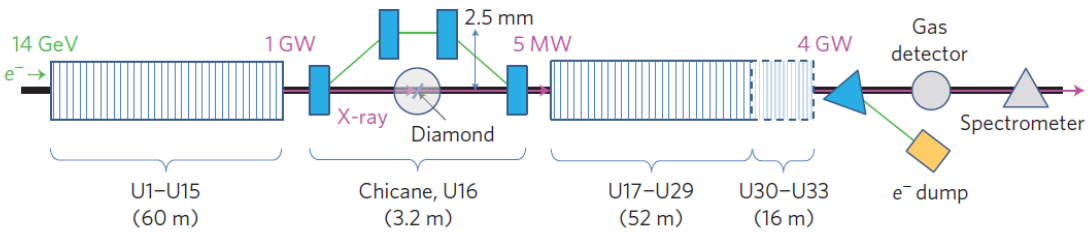

Figure 3.2: Schematic of the setup used at LCLS to give self-seeding in the hard x-ray regime. Diagram taken from [2].

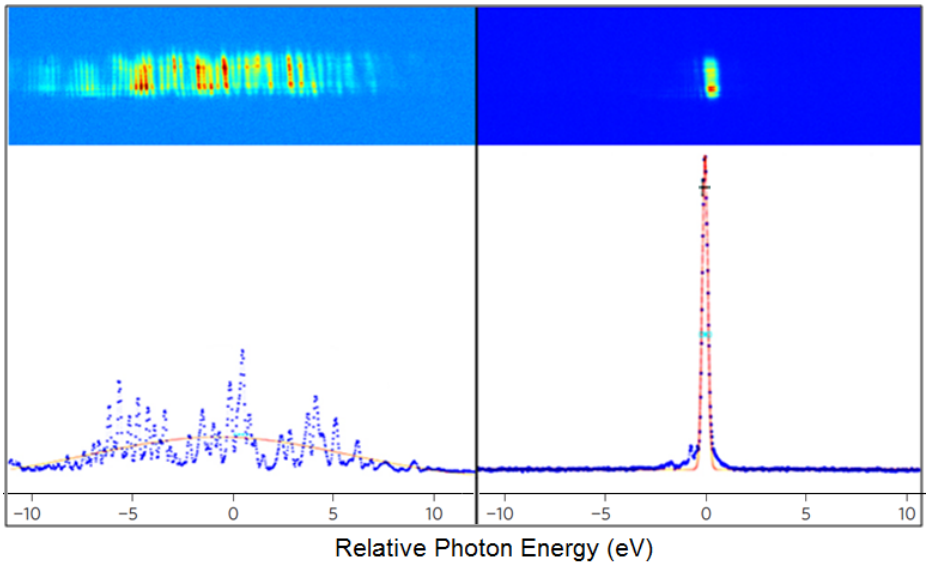

Figure 3.3: X-ray spectrum from SASE (left) and self-seeded (right). Data adapted from [2] by Greg Stewart, LCLS.

range [156]. However, work at the DESY facility in Hamburg demonstrated, for ultraviolet light, the possibility of self-seeding, where the SASE beam from the first half of the undulator is used as the seed beam for the latter half.

The full details are presented in Amann *et al.* [2], but the essential parts of the setup shown in Figure 3.2 are the diamond, which acts as an x-ray monochromator by diffracting only the x-rays within a small (chosen) energy range. To account for the delay that this induces in the X-ray path length, the electrons are deflected by magnets before the crystal to send them through a chicane, such that they remain temporally overlapped with the x-rays in the second half of the undulator. This remaining undulator section is still sufficiently long to allow the FEL to reach saturation, so that the beam produced is still exceptionally bright. The magnets after the undulator deflect the electrons into a beam dump, giving the desired x-ray beam onto target. This self-seeding reduced the bandwidth by a factor of 40-50, relative to that from SASE, as can be seen in Figure 3.3.

Having described the basic operation of an XFEL, we can now move on to seeing some of the results obtained from their application to studying structure factors in warm dense matter. Both of the experiments presented were carried out at the MEC endstation of LCLS - as well as the XFEL beam, available between 4 - 10 keV, this has a frequency doubled Nd:glass system, delivering ns long beams at 527 nm, with a power on the order of GW, as well as a short pulse Ti:Sapph laser giving $\sim$ 10 TW at 800nm. This allows the creation of the warm dense systems that we wish to probe.

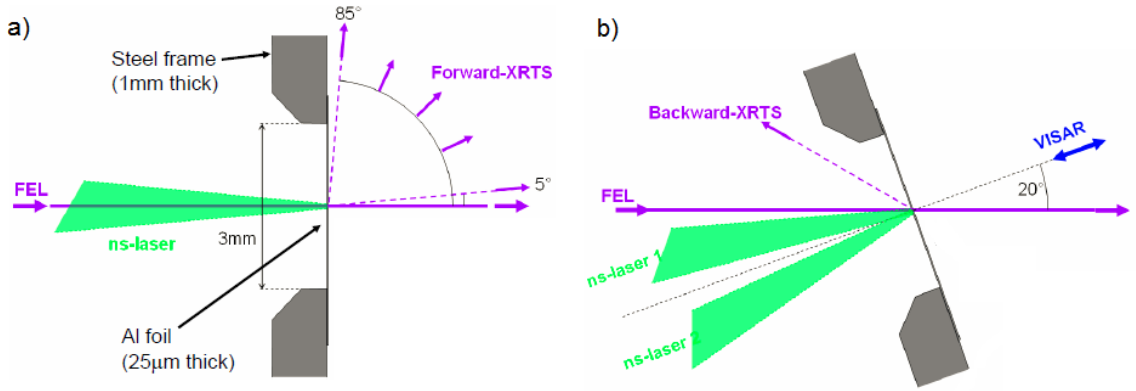

Figure 3.4: Arrangement of the diagnostics and beams for the experiment, in a) side and b) top elevation.

3.3 MEC L592 - Static Structure Factor

This experiment aimed to measure the static structure factor of warm dense aluminium over a wide range of scattering angles ($\theta = 5°$-$85°$), corresponding to a range of k-values up to and beyond the first peak in the structure factor. The novelty in this proposal came from the possibility to probe the low-k, and consequently long wavelength, region with greater fidelity than had been previously been possible, potentially giving much more accurate data on the compressibility of the material in the warm dense state. As it was only the static structure factor being measured, energy resolution was not important, giving a large integrated signal for measurement on this forward XRTS spectrometer.

The other diagnostics deployed were a VISAR (Velocity Interferometer System for Any Reflector) laser line to measure the shock breakout time (as in e.g. [18]), as well as a backward XRTS spectrometer, arranged as shown in Figure 3.4. We aimed to probe the sample at the breakout time, as at this point we have the most homogeneous sample, as can be seen in the simulated density in Figure 3.5.

In the experiment, we had two 3 ns beams with ∼16 J of energy in each, focused onto overlapping spots of 100 μm using phase plates, giving an incident laser intensity of approximately 50 TW/cm^2. These values were used in the 1-dimensional radiation dynamics code Multi to give expected values for the temperature and compression to be reached in the experiment. These results suggested that we would reach temperature of 3-5 eV with a maximum density of around 7 g/cc, corresponding to a compression ratio (ρ/ρ_0) between 2-2.5. It also predicted ionization of $Z_f \sim 3$, a value which is obviously important for evaluating the strong coupling parameter Γ and therefore determining whether we are probing a warm dense sample.

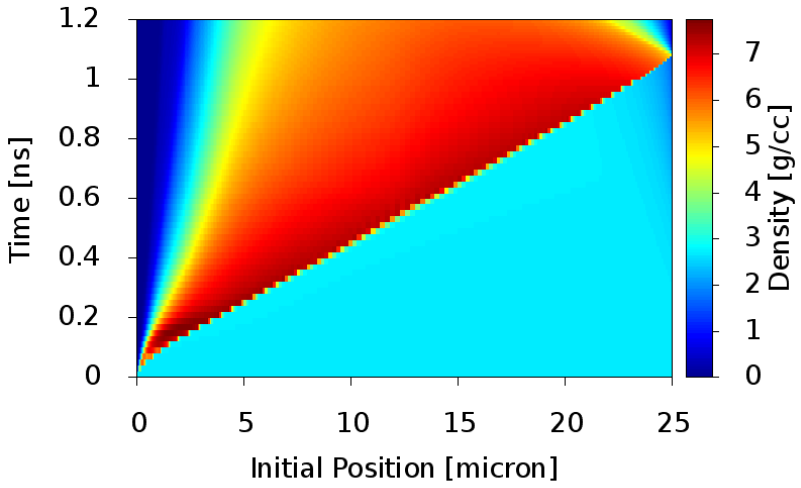

Figure 3.5: Results from 1-dimensional radiation hydrodyamics simulation (using the radiation hydrodynamics code Multi) of the density expected to be reached in the target due to the incident laser intensity (5.0×10^{13} W/cm^2). The corresponding temperature and ionization at the probe (shock breakout) time were $T_e = 5$ eV, $Z_f = 3$.

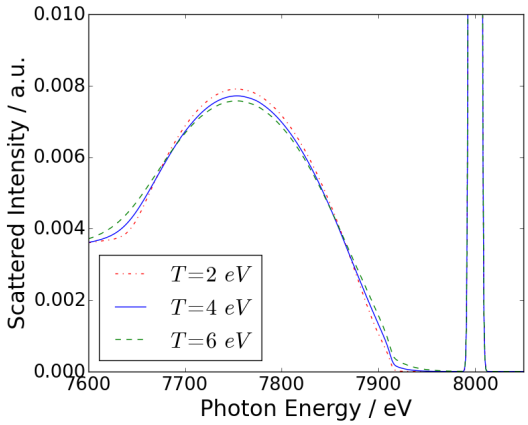

Figure 3.6: Modelled downshifted Compton peak from aluminium at ρ=5.4 g/cc, equivalent to $\rho/\rho_0 = 2$, with Z_{free}=3. Values are normalized to their respective Rayleigh (elastic) peaks.

The backward XRTS spectrometer was used to probe the conditions of the plasma created, as in earlier experiments on this facility e.g. [92][47]. This spectrometer was energy resolved and mainly focused on looking at the downshifted Compton peak. This is described as a Compton rather than plasmon peak as we are at a very large ($\theta = 150°$) scattering angle, giving a large k-value and consequently small length scale (non-collective effects).

In general, we would expect a Compton peak to broaden in width with increasing electron temperature, due to Doppler effects, an effect that can be exploited as a temperature probe [36]. However, we can see in Figure 3.6 that the change in peak width over a range of temperatures around the expected value of 4 eV is very small, according to modelled results from

the XRTS code of Gregori *et al.* [65]. This is due to the relatively low electron temperature, and high density, giving a high degree of electron degeneracy in the system. In such cases, increasing the temperature makes a much smaller difference to the electron velocity distribution than in a less dense plasma.

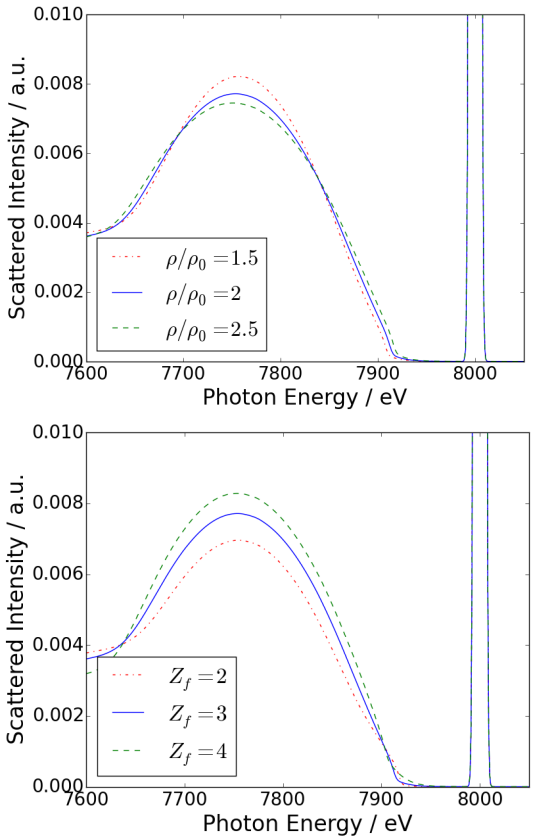

Figure 3.7: Modelled downshifted Compton peak from aluminium at $T = 4$ eV, varying either the level of compression, with Z_f fixed at 3, or the degree of ionization, with $\rho/\rho_0 = 2$. As before, the values are normalized to their respective elastic peaks at 8000 eV.

Now moving to look at the theoretical effect of density, we first note that the width of the Compton peak for a Fermi degenerate plasma scales with the Fermi energy [60]. Consequently, because the Fermi energy is related to the electron number density as $E_F \sim n_e^{2/3}$, and by ionization balance it is obvious that $n_e = Z_f n_i$, the width of the peak will change with both the sample density and the degree of ionization. The effects of these can be seen in Figure 3.7.

As expected, the width can be seen to increase with both the compression and the ionization, although the effect is significantly more pronounced in the case of higher average ionization. However, a much more noticeable change is observed in the ratio of the peak signal strength between inelastic and elastic with increasing ionization, as the height of the Compton peak increases when there are more free electrons from which to scatter. Consequently, this diagnostic was mainly used to characterize the ionization of the material.

While this backward spectrometer allows us to start diagnosing the plasma conditions reached in the experiment, it is the forward spectrometer that will probe the static structure factor that we are interested in. As can be seen in Figure 3.8, different models for the potential[1] give quite different forms of the structure factor under the

[1]In this case, the potentials were used in the HNC equations to obtain the SSF, but similar results would be found from MD simulations.

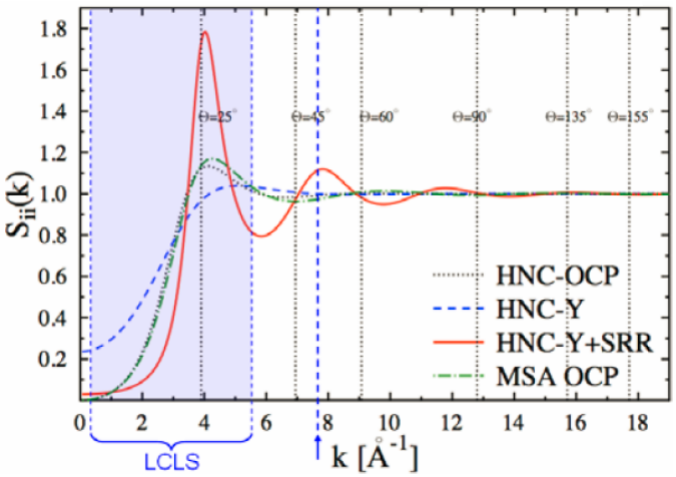

Figure 3.8: Modelled static structure factors for the predicted plasma conditions, with the range of k-vectors accessible in this experiment highlighted.

predicted conditions (equivalent to $\Gamma \sim 30$). These will then be modified by the form of the atomic form factor $f(k)$ and screening factor $q(k)$ as described above, and by Chihara [25]. This also allows us to constrain the density and temperature, as the static structure factor changes significantly with these - significantly, the position of the first peak is inversely proportional to the Wigner-Seitz unit radius ($a = (n_i)^{-1/3}$) and so gives a strong measure of the density.

The height of this peak is controlled by the coupling factor Γ and so, with the density and ionization constrained, we can also find a value for the temperature from this data. However, we also know that the temperature and density of a shocked material are constrained by the Hugoniot relations (see Appendix 2). Although these depend on the equation of state for the material, this is relatively well-characterised for aluminium and so provides another measure of the temperature.

Moving now to the results from the experiment, initial analysis by P. Neumayer, which is yet to be published, indicates a beam bandwidth of between 20 and 30 eV, corresponding to $\Delta E/E \sim 0.25$ %, in line with expected values. Early runs used a Cu target to cross-calibrate the spectrometers using Cu K-α, which is of almost the same wavelength as the XFEL beam (8047 eV vs. 8000 eV, respectively). After correcting for losses due to the finite thickness of the target, which significantly improved the fit of the models to the data, best agreement was found for a peak position of $(48 \pm 2)°$, as shown in Figure 3.9. This corresponds to $\rho = (5.2 \pm 0.6)$ g/cc, which is slightly lower than predicted but could be due to lower energy in the pump beams therefore driving a weaker shock.

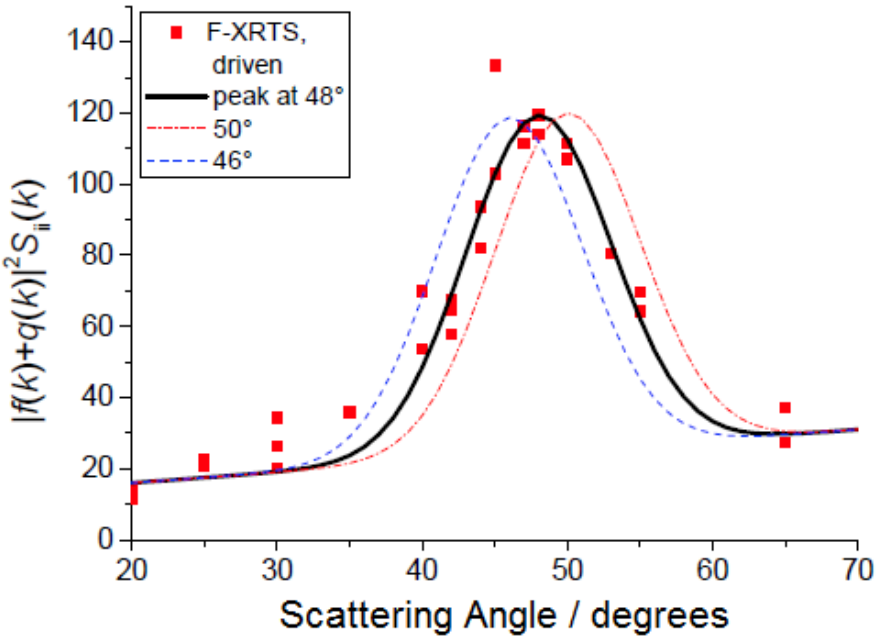

Figure 3.9: Experimentally obtained $S(k)$ values, demonstrating best fit to data at 48° scattering angle.

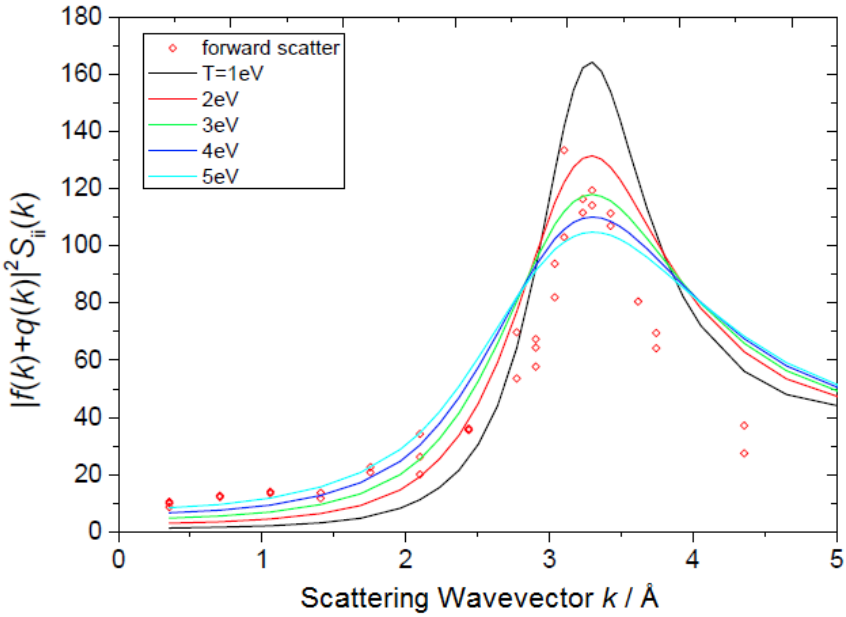

Figure 3.10: Experimentally obtained $S(k)$ values, compared to results from SOCP simulations at a constant density of $\rho = 5.2$ g/cc and temperature varying from $= 1 - 5$ eV.

Data on the Hugoniot in aluminium, taken from equation of state data in PROPACEOS, suggests that this corresponds to a temperature of $T = 3(+2/-1.5)$ eV. Results from SOCP at the measured density with a range of temperatures around this value are compared to the experiment results in Figure 3.10.

Calculations of the elastic/inelastic ratio in the backward spectrometer shows a large spread of values, with the best estimate of $Z_f = 2.8 \pm 0.6$. Although this does agree with the predicted value of $Z_f = 3$ it does not constrain it very well.

Although the height of the scattering peak is best matched by a temperature of 3 eV, the shape of the graph as a whole differs significantly from that expected, making a confident statement of the temperature difficult. The most striking result is that the peak is significantly sharper, with the structure factor decreasing after the peak much faster than any predicted results, and with a corresponding shallower slope at low k. The value at $k \to 0$ is also higher than the values predicted in the SOCP model, indicating a higher compressibility, and analysis is ongoing to quantify the uncertainty in this result.

In conclusion, this shows some of the capabilities of the LCLS platform. No previous experiments had measured the structure factor in warm dense matter over such a range of k values, as the collimation of the beam allowed probing at shallower angles, and so longer spatial scales, than any earlier work. There is significant scatter in the data, especially around the peak values, but this is not necessarily surprising as any shot-to-shot variation in the drive beam will change the degree of compression and hence the peak position. Further experiments have managed to measure a wide range of angles in a single shot [49], which could in future mitigate the reproducibility problem and allow greater confidence in observations of the ion-ion coupling strength in such samples.

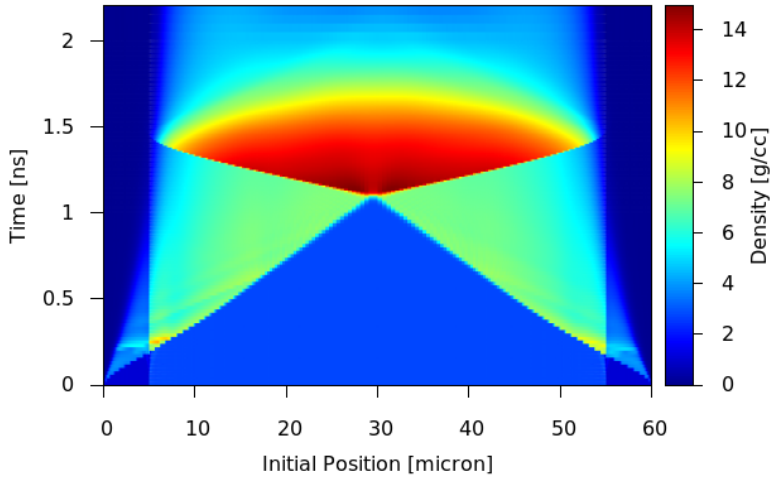

Figure 3.11: Results from 1-dimensional radiation hydrodyamics simulation (using MULTI) of the density expected to be reached in the target due to the incident laser intensity, with a corresponding electron temperature of ∼10 eV and ionization of 4 at the centre.

3.4 MEC L708 - Dynamic Structure Factor

As we saw in the computational work in the previous chapter, the ionic portion of the dynamic structure factor in warm dense matter has up- and down-shifted peaks due to collective oscillations of the ions. These are, in some ways, similar to the collective electron oscillations, known as plasmons, which were experimentally observed for the first time in 2007 [59]. This observation has allowed models for collisional damping[176], temperature relaxation[162][19] and many other properties to be tested.

Due to the high much higher ionic mass, however, the corresponding ion waves are much lower frequency and so result in much lower energy shifts - on the order of tens of meV, rather than tens of eV - meaning that measurements had not previously been possible. However, with the self-seeding upgrade at LCLS and the corresponding decrease in bandwidth with minimal photon number loss, photometric calculations suggested that observation of this phenomenom is now possible.

The setup for the experiment was similar to that of L592 described earlier, though with the two laser beams driving separate, coalescing shocks, rather than a single shock; the optical lasers, with energies of 5 J in 3 ns, are passed through phase plates to give a flatter spatial profile, and focused to 50 μm spots on either side of a 50 μm

thick aluminium target coated with a 2 μm thick plastic tamper layer. These launch converging shocks into the system, with the expected density and temperatures again modelled with a radiation hydrodynamics simulation package, in this case MULTI, with the results shown in Figure 3.11. With the spot size and target thickness for this setup being similar, the assumption that a one-dimensional simulation will be accurate is less valid, and so care must be taken in using these results.

The X-ray beam was incident on the now-compressed target 2 ns after the optical heating beams, to ensure that the shocks have coalesced but with the trade-off that we are not probing at the point of highest density. This is necessary since 1-D simulations tend to overestimate the shock speed, such that the coalescence time might be slightly later than predicted. Indeed, the results from MULTI gave faster shock speeds than those from Helios, and consequently higher ρ and T_e at the shock centre. However, both codes give similar predictions for the values at 2 ns, with $\rho \sim 7$ g/cc and $T_e \sim 5$ eV.

As described above, the X-ray beam in self seeded mode has a spectral resolution of $\Delta E/E \sim 10^{-4}$, equivalent to a width of around 1 eV. While this is a hugely less than the SASE spectrum, it is still not small enough to resolve the ion peaks, which we predict to be separated by just a few hundred meV at the predicted target conditions. To reduce the bandwidth further, the beam was passed through a Si (444) monochromator, used at a Bragg angle of nearly 90°. At such high orders and angles, the change in wavelength over the width of the crystal rocking curve is very low, giving a reduction in the bandwidth to around 50 meV, at the cost of a significant (approximately order of magnitude) drop in the photon number.

The spectrometer used to resolve the scattered light contained a spherical diced Si (444) crystal, shown in Figure 3.12. While in toroidally bent crystals, the strain from the bending can reduce the energy resolution of the crystal, the diced crystallites are arranged such that each produces the same spectrum, which then overlap on the detector to increase the signal. It was deployed in Johann geometry, such that each of the diced crystals lies on the Rowland circle. With the crystal placed at a distance of 1 m from the target, the maximum energy bandwidth from a single shot was 300 meV. Consequently, the crystal was rotated (by 0.2°) after each series of shots to allow observation of both the up- and down-shifted peaks.

The x-rays diffracted from the spectrometer crystal were detected using Cornell-SLAC Pixel Array Detectors (CS-PADs). Each 'pad' contains 2.3 million pixels, each 100 μm wide, in a 20.3 $\times$ 44.0 mm area. Using their high gain mode, they have

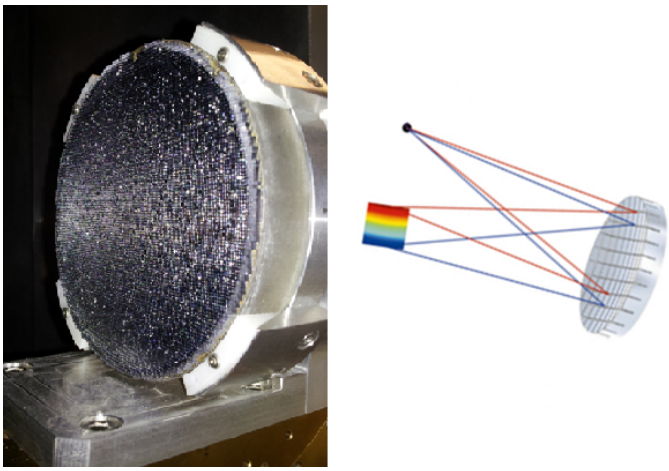

Figure 3.12: The Si (444) crystal used in the spectrometer for this experiment, and a schematic of how it can give the ultra-high resolution needed to observe the ion peaks.

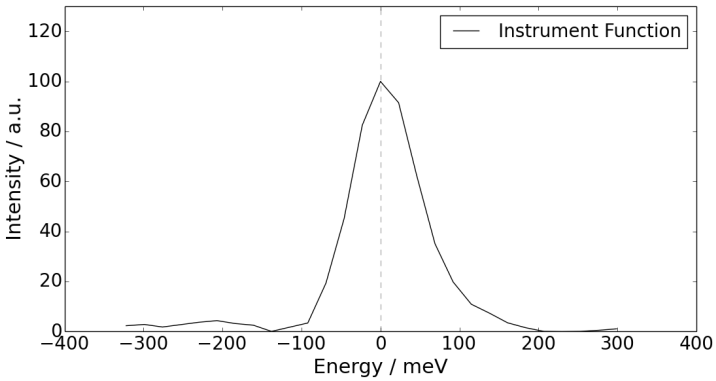

Figure 3.13: Instrument function of the spectrometer, measured from 500 shots of scattering from cold CH sample.

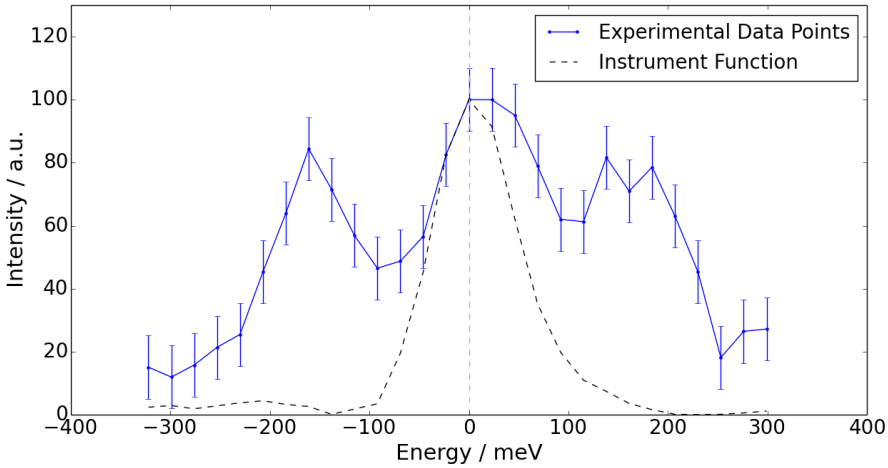

Figure 3.14: Energy resolved X-ray scatter from warm dense aluminium at $\rho = 6.3$ g/cc and $T = 3$ eV. Also shown, as the dotted line, is the instrument function with width 100 meV.

a signal-to-noise ratio of 6 and can detect single photons to give absolute photon numbers.

Initial measurements were taken from cold CH samples, built up over 5000 shots from the FEL, to give a measurement of the instrument function, shown in Figure 3.13. With a width of around 100 meV, this was low enough that we expected it to be capable of resolving the peaks due to ion-acoustic waves.

Shown in Figure 3.14 are the results obtained from the aluminium sample, centred on $E = 0$ being the incoming X-ray energy. The spectrum was obtained by averaging data taken from sixteen shots, eight each looking at the up- and down-shifted peaks, with the results stitched together. On either side of the central peak, peaks can be seen at ± 150 meV, corresponding to the ion acoustic waves, and representing the first experimental observation of such a phenomenon in warm dense matter.

3.4.1 MD Analysis

To compare the results to models from DFT-MD simulations, values for the temperature and density are needed. As has already been mentioned, one-dimensional simulations are not necessarily reliable for targets for a setup such as this, however a very similar experiment to this one had been carried out two months prior to this work with identical laser parameters and targets. Without the use of a monochromator, a wider bandwidth allowed the measurement of the SSF, obtaining values of temperature at 3 eV and density at 6.3 g/cc [49]. Although not exactly the same

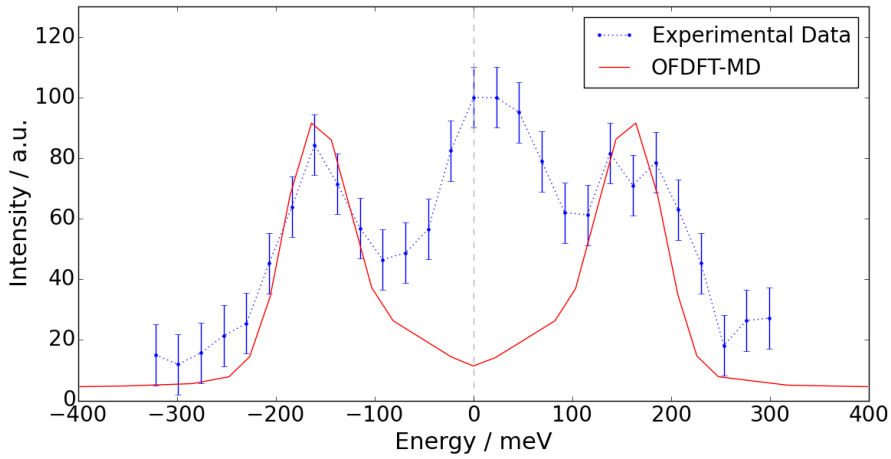

(a)

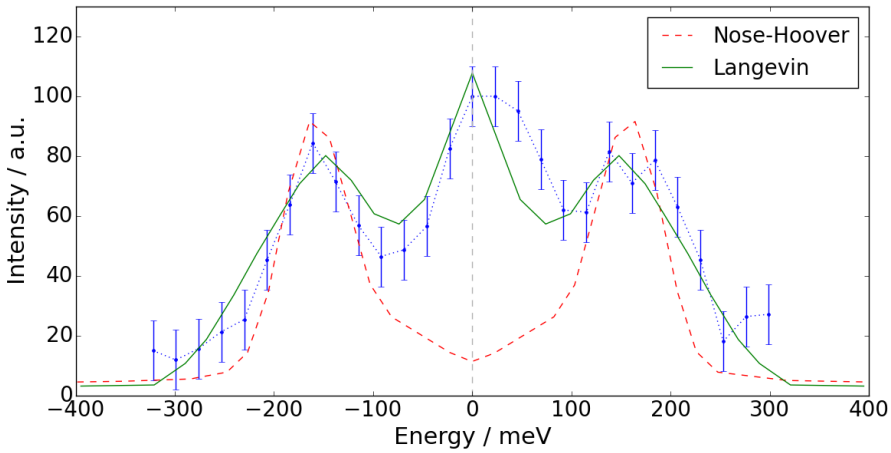

(b)

Figure 3.15: a) Experimental data of inelastic scatter, compared to results from MD simulation using OFDFT, with a Nosé Hoover thermostat. b) Comparison of OFDFT simulations with Nosé-Hoover and Langevin thermostats.

as those used in modelling, they were sufficiently close, especially in the case of the density that defines the positions of the peak, that the analysis carried out with the original values of 5 eV and 7 g/cc was used.

First, the results are compared to the OFDFT-MD work done by T. White. This reduces the computational cost of running DFT simulations by considering the electron energy functional to be described entirely by the electron number density. Rather than requiring the consideration of the Kohn-Sham orbitals, pseudopotentials for the electron interactions with the ions were found by inverting the Kohn-Sham equations. A fuller discussion of the derivation of this approach can be found in the excellent paper by T. White [169].

Using this approach to model the system, and calculating the dynamic structure factor extracted from the simulation, the results shown in Figure 3.15a are obtained. The simulated spectrum was scaled to fit the experimental spectrum, as the results are presented in arbitrary units. While we are confident in saying that the simulation fits the ion acoustic peaks, at least within the error of the experimental data, the central peak which is observed is not present in the OFDFT simulation.

Since these results were obtained, different suggestions have been put forward to explain the absence of the central peak in the MD simulations. The first was that it may be due to the ensemble used in the MD simulation, or the use of an unphysical thermostat. The thermostat is, as explained in Appendix 1, necessary to keep the 'temperature' of the MD simulation the same between timesteps, as the equations that govern such simulations only guarantee the conservation of energy. The Nosé Hoover thermostat used in obtaining the OFDFT results in Figure 3.15a restricts the possible phase space that can be reached by the system and, although its formulation should prevent low frequency dynamics being lost, it could be unrepresentative of the physical system it models in this respect.

This was tested by running an identical simulation with a Langevin thermostat. The random 'kicks' that change the velocity appear as the central peak in the DSF, as increasing the friction parameter caused the central peak to grow in size. By varying this parameter in ABINIT simulations a best fitted result can be obtained, shown in Figure 3.15b, with a friction parameter of 0.003 in atomic units ($\mathrm{Ha}/\hbar \approx 4.13 \times 10^{16}\mathrm{s}^{-1}$). This agreement is encouraging, and the viscosity obtained is comparable to that predicted, as we will see below. One possible explanation for the applicability of this method, which was formulated to describe the effects of a solvent on a dissolved sample, is that by treating the ions as static in the timeframe of the electrons, direct interaction between them is ignored. Consequently, the Langevin thermostat could model the effect of electron-ion collisions on the DSF, a possibility which is explored in a paper by Mabey et al. to be published later this year.

Although varying the thermostat can give a better agreement with the experimental data, another possibility is that simulations such as this should not be able to recreate this feature of the data. As increasingly low-frequency effects correspond to increasingly long timescales, it may be the case that this cannot be recreated without much longer simulations. Additionally, in the process of obtaining the DSF from the output of the simulation, the intermediate scattering function $F(\mathbf{k}, t)$ is smoothed at large t values to remove noise, but potentially also removing the low-frequency

behaviour. Further work, with increasing simulation lengths, has not yet shown a central peak appearing with the usual Nosé thermostat.

Finally, this may be due to the uncertainty with which the conditions are known. Although the results from Fletcher et al. suggest that at least some of the sample is under conditions close to what we expect, this does not preclude the possibility of the signal we obtain coming from both that and a region at a different density. A larger, lower density region (giving a similar total scattered flux) would give two peaks which much smaller energy shifts, which would possibly not be resolved and appear as the central peak in our results. Future experiments would therefore benefit from better diagnosed, and more uniformly generated, target conditions, to help rule out explanations such as this.

3.4.2 Hydrodynamic Analysis

As well as the MD approaches that have been mainly used to explain the observed experimental data, hydrodynamic approaches have also been suggested. Although such descriptions would only generally be relevant for liquid-like conditions, and consequently could only describe warm dense conditions when $k \gg \kappa$, the screening length, the work by Mithen et al. [107] referenced above suggests that the range of applicability could be greater.

A generalised form for the DSF in hydrodynamics can be taken, and the parameters varied to fit the experimental data. Although such an approach cannot be predictive, it does yield values for the thermodynamic and transport properties of the system. The equation for this generalised hydrodynamic DSF takes the form described by Schmidt *et al.* [141], with explicitly quantum terms ignored:

$$\begin{aligned}\frac{S(k,\omega)}{S(k)} =& \frac{\gamma-1}{\gamma}\frac{c_s^2k^2}{\omega_s^2+c_s^2k^2}\frac{2\varepsilon_Q a k^2}{w^2+(\varepsilon_Q a k^2)^2} + \\ & \frac{\gamma^{-1}c_s^2k^2+\omega_s^2}{c_s^2k^2+\omega_s^2}\left(\frac{\Gamma k^2}{(\omega+c_qk)^2+(\Gamma k^2)^2}+\frac{\Gamma k^2}{(\omega-c_qk)^2+(\Gamma k^2)^2}\right)\end{aligned} \tag{3.3}$$

This generalised description accounts for the screening effects of the electrons without explicitly needing to describe them, with κ the screening parameter in the system. In this case, w_s is the screened plasma frequency, c_q the peak position, ε_Q the peak width parameter and Γ the sound attenuation constant, all defined in Equation (3.4) below. Other parameters are the sound speed, c_s, the thermal diffusivity D_T, the ratio of heat capacities γ and the bulk and shear viscosities, η and ζ respectively.

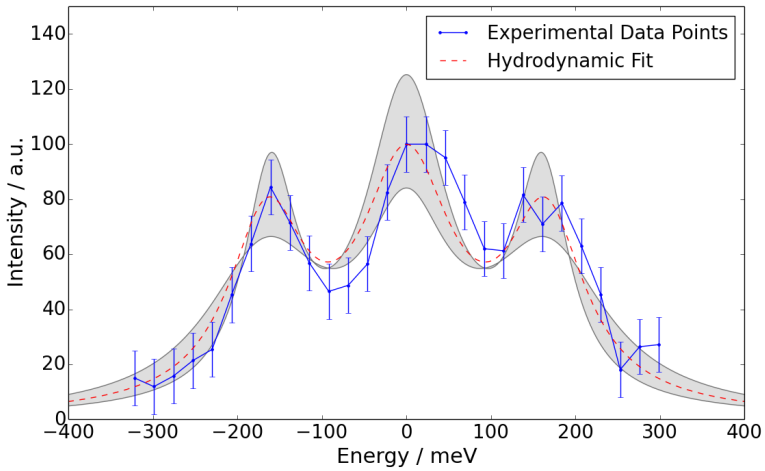

Figure 3.16: Experimental data spectrum with hydrodynamic fit, of the form described in Equation (3.3). Shaded region represents fit to experimental data ± experimental error.

$$c_q^2 = \omega_s^2 + c_s^2 k^2 - \frac{w_{pi}^2 k^2}{\kappa^2} \tag{3.4a}$$

$$w_s = \omega_{pi} \frac{k^2}{k^2 + \kappa^2} \tag{3.4b}$$

$$\varepsilon_Q = (\omega_s^2 + \gamma^{-1} c_s^2 k^2)/c_q^2 \tag{3.4c}$$

$$\Gamma = \frac{1}{2}\left[D_T \gamma (1 - \varepsilon_Q) + \frac{1}{\rho}\left(\frac{4}{3}\eta + \zeta\right)\right] \tag{3.4d}$$

In the expression (3.3) the first term broadly controls the middle peak, and the latter term controls the side peaks with c_q the position and Γ controlling the width. The wide range of parameters, combined with the error bars on the experimental data, means that there is a large degree of uncertainty in the fitted values.

To obtain the values, the difference between the experimental values and the hydrodynamic form was minimized in a Python program using a Nelder-Mead simplex algorithm over the variables in the model, plus a scaling constant to account for the fact that the values are in arbitrary units. This was repeated for the experimental data plus/minus the experimental error, to give the ranges of the fitted values.

The best-fit spectrum is shown in Figure 3.16, with the corresponding parameters given in Table 3.1. There is a range of earlier work looking at extracting values for the thermodynamic properties of systems described with a Yukawa potential from MD simulations, and some of the results for the quantities fitted for are given for comparison. The most significant deviation from modelled results is in the value γ,

	Units	Fitted value	Fitted range	MD Results
γ		1.88	1.43-2.29	1.08†, ~ 1‡
D_T	10^{-7} m^2/s	1.58	1.34-1.48	10.1 [35], 7 [118]
c_s	km/s	13.56	13.28-13.66	6.54† , 9.67 ‡
η	mPa s	1.038	0 - 2.417	2.97[137], 1.16 [140]
ζ	mPa s	0.859	2.45-0.854	[44]

Table 3.1: Thermodynamic properties obtained by fitting a generalised hydrodynamic form of the DSF to the experimental values for an aluminium plasma at T =5 eV and $\rho = 7$ g/cc. Also given are values for the quantities from molecular dynamics simulations.
Results marked † were calculated by White [166], using the Hamaguchi EOS for the internal energy and thermodynamic properties calculated as described by Mithen [105]. Those marked ‡ are taken directly from MD simulations Mithen [105]. Other values are taken from references given, except for the bulk viscosity ζ, as references including [44] generally only give it as being less than the shear viscosity η by factors of 1-2 orders of magnitude.

the ratio of specific heats, with the result here closer to that for an ideal monatomic gas ($\gamma = 5/3$) than that of a liquid ($\gamma \gtrsim 1$).

From Equation 3.3 it is obvious that, for a significant central peak to be present, we require $\gamma \neq 1$ such that the term $(\gamma - 1)/\gamma > 0$. While there is good agreement between the Hamaguchi model and the MD simulations, the significantly lower value for γ from the experiment is merely a restatement of the fact that previous work did not predict the existence of a central peak, and so returns to the question of whether this feature is due to the ion dynamics or is an artefact of the experiment.

The sound speed, c_s, also varies significantly from theoretical values obtained from MD simulations. Although previous work has suggested that the Hamaguchi EOS model does not recreate the value for systems with $\kappa > 1$ [105], the fact that the fitted value also exceeds that from explicit numerical evaluation is more concerning. While a further increase in theoretical models could be obtained from changing the Yukawa potential to a Yukawa + SRR potential [166], work similar to that of Mithen with this new potential has not yet been carried out.

The other three properties, best described as transport properties of the system, do not show particularly good agreement, although the uncertainty in their values is greater than that estimated in the table as they, broadly, control the width of the peaks. In this case, where the peak widths are comparable to that of the instrument function, the values obtained must be treated with a degree of caution. While papers such as Feng *et al.* [44] suggest that $\zeta < \eta$, which is not definitive in the values

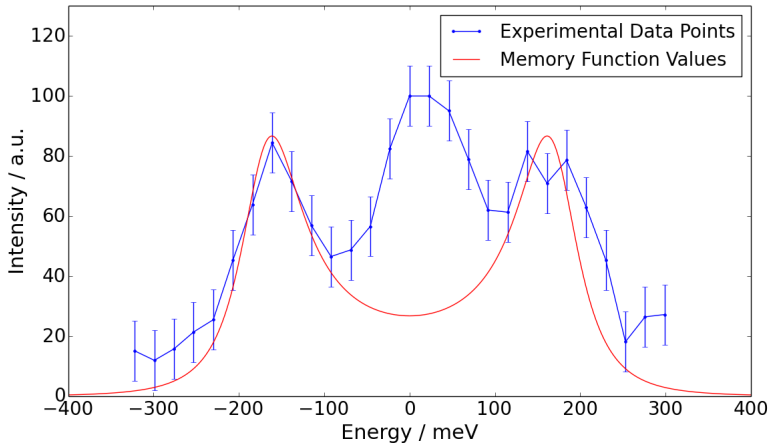

Figure 3.17: Experimental data spectrum with values calculated from the memory function approach in Equation (2.44). The dimensionless values obtained from that approach are then scaled to the peak position c_q from the generalised hydrodynamic description, defined in Equation (3.4a).

we have obtained, the fact that the only dependence of the fit on these quantities is through $(\frac{4}{3}\eta + \zeta)$ suggests that they can be varied with respect to each other with very little effect. Consequently, drawing any conclusions about the shear viscosity within the system is risky. We can note that the obtained value for the viscosity from Langevin dynamics (equivalent to 2.63 mPa s) does fall within the fitting range.

Another hydrodynamic approach is, of course, using the memory functions described in the previous chapter. Although these were formulated for a one component plasma and neglected the effects of screening, the fact that the values obtained are dimensionless means that we can choose to scale it by the peak position value in the generalised hydrodynamics approach c_q. This produces the results shown in Figure 3.17.

The positions of the peaks are, of course, correct, as we have chosen the scaling such that they agree. The shape of the peaks also seems to agree, which is more encouraging, although the width of the instrument function being comparable to the side peak widths means that this agreement is not necessarily significant. The other important feature to note is that, like the initial MD approach above, there is no central peak, although the value at zero energy shift is greater.

Given the lack of certainty about the physicality of the central peak, and the ease with which the memory function results can be obtained compared to the computational cost of even the relatively quick OFDFT-MD, this is an encouraging result for the use of memory functions in modelling warm dense matter. Without more

experimental validation in this regime, memory functions and hydrodynamic models in general should not be used as stand-alone predictors, but are not without their advantages in modelling ion behaviour.

3.5 Conclusions

This chapter has presented results from two experiments carried out on the MEC endstation of the LCLS XFEL facility, demonstrating some of the capabilities of this revolutionary new technology.

The first experiment looked at the angularly resolved scattering from warm dense aluminium, probing much smaller angle scattering than would be possible with other x-ray sources. Such scattering, corresponding to long length scales within the system and consequently highly collective effects, can potentially give a direct measurement of the compressibility at the low-k limit. The results do indicate that this is higher than that predicted from SOCP models, but are not clear enough to give an absolute value. The experiment also gave an example of how energy resolved XRTS can be used for diagnosing the temperature, density and degree of ionization in the plasma, especially in combination with measurements of the static structure factor. It suggests that being able to routinely measure static structure factors and test models for equilibrium behaviour in warm dense matter is within reach.

The second experiment used the beam in self-seeded mode with a Si (444) monochromator to obtain a previously impossibly narrow bandwidth, capable of resolving the scatter from a warm dense aluminium sample to unprecedented resolution. This allowed the observation of the ion acoustic modes in a warm dense sample for the first time, with the energies of the mode agreeing with predicted values. The experimental results were compared to molecular dynamics simulations, with a significant disparity in the matter of a large central (elastic) peak which was not present in any simulations.

Other approaches to analyzing the data came in the form of fitting the observed spectrum to a generalised hydrodynamic form, which accounts for the screening effect of electrons. This allowed values for a variety of thermodynamic quantities to be obtained. There were significant disparities between these obtained values and those predicted from simulations with a Yukawa potential, even accounting for large experimental errors in the data due to low photon flux.

Further analysis will seek to confirm whether the observed central peak is due to the ion dynamics or is from another phenomenon in the experimental technique.

Now that such a technique has been demonstrated successfully, we can also hope that similar experiments can be carried out again. Such campaigns could look at measuring the shift at a range of k-values, either on separate shots or by deploying multiple spectrometers. This would allow better characterisation of the dispersion function of the ion modes in and beyond the acoustic regime.

Chapter 4

Temperature Equilibration

4.1 Context

As seen in the previous chapter, warm dense matter can be created by using shocks to compress solid materials, with associated $P\,dV$ heating due to driving the sample along the Hugoniot. Many other techniques for creating such states, though, rely much more heavily on heating, whether through direct laser irradiation or heating by charged particle beams, a method pioneered by Patel *et al.*[124]. These allow access to a range of states not restricted by the Hugoniot relations, but can introduce other effects to be considered.

In the case of direct laser irradiation, a wide variety of effects inhibit the accurate characterization of the electron and ion species temperatures. In general, an optical pump will heat electrons in the first few nm of the material, setting up a non-thermal distribution which then transfers energy into the phonon modes of the ions. However, there are expected to be non-negligible contributions from direct coupling of the pump into phonon modes, as well as inhomogeneities in the initial heating profile.

An alternative method, and that used in most of the experiments described below, is to instead use the optical laser to drive a charged particle beam which then heats the sample. As with the optical pump, this will deposit energy into the electrons, but without the complicating factor of phonon coupling as the stopping power of the ions is much less than that of the electrons[1]. In addition, the heating is largely isochoric and, with appropriate charged particle spectra, able to deposit energy much more homogeneously throughout the sample.

Using such a heating mechanism, the 'initial state' of the heated system is very far from equilibrium, with an ionic lattice which is still near to room temperature,

[1]For example, in the experiments considered they generally differ by a factor of $\gtrsim$1000.

but an electron subsystem at a greatly elevated temperature. If results obtained are being assumed to represent those of long-lived warm dense states, then clearly it is necessary for the system to be allowed to reach equilibrium before being probed. There is a danger in assuming that the equilibration happens very quickly (∼ps or even less) as some of the results we have obtained suggest that such an assumption is not necessarily correct. Consequently, experiments are being carried out to measure the rates of temperature equilibration in strongly coupled plasmas both in the warm dense matter regime [24], and in low temperature plasmas [7].

However, work on such non-equilibrium systems also has merits of its own, beyond measurements of the equilibration rate. Such systems appear to exhibit unusual phase transition behaviour [5] and show significant changes to thermodynamic [10] and electrical [23][126] properties. Consequently, this an area of increasing theoretical and computational exploration (e.g. [32],[29],[78]) with applications ranging over many of the areas in which warm dense matter is significant, including in ICF [175].

This chapter looks at ways to model the rate of energy exchange in such systems. First, the two temperature model is briefly described, which treats the electrons and ions as separate systems, with a term to described the energy exchange between them. Different approaches to evaluating this exchange term are then described, with their relative merits considered. Results from these models are presented in the following chapter, alongside relevant experimental values.

4.2 Two Temperature Model

The energy exchange behaviour of the out-of-equilibrium states described above has, throughout the work discussed here, been modelled using the two-temperature model. This treats the electrons and ions as separate systems, linked only by an energy exchange term, and can be summarised by the coupled equations:

$$C_{ele}\frac{\partial T_{ele}}{\partial t} = \nabla \cdot (\mathbf{K}_{ele}) - G(T_e) \cdot (T_{ele} - T_{ion}) + S(\mathbf{r}, t) \tag{4.1a}$$

$$C_{ion}\frac{\partial T_{ion}}{\partial t} = \nabla \cdot (\mathbf{K}_{ion}) + G(T_e) \cdot (T_{ele} - T_{ion}) \tag{4.1b}$$

The use of this approach to such systems has been common since early work described by Elsayed-Ali *et al.* and others [40][4]. It relies on treating the electrons and ions as independent subsytems, with the only interaction taking place between them contained in the electron-ion coupling factor $G(T_e)$. Energy transfer within

the system is described by the conduction term $\nabla \cdot \mathbf{K}_a$, but in the systems studied here the time- and length-scales are sufficiently small that these terms can usually be ignored, as they take much smaller values than the electron-ion coupling term[2]. This means that, energy deposition from the source term $S(\mathbf{r}, t)$ is finished, the behaviour of the system is controlled solely by the electron-ion coupling factor $G(T_e)$.

Many models for the energy transfer take it to depend primarily on electron-ion collisions or electron-phonon interactions, and so the factor G is assumed to depend only on T_e [1]. However, an explicit dependence on T_i is found within models considering coupled electron-ion modes, as we will shortly see [33, 162, 161].

One significant assumption made in this two temperature model is that the sub-species have a well defined 'temperature'. This definition implies that the particles have had sufficient time to exchange energy with each other and reach an equilibrium distribution, whether this is Maxwellian, Fermi etc., with this process described as thermalization. As we have already said, the timescales of these experiments are very short and so assuming that the distributions are thermal at every point is not easy to justify. Interestingly, however, there is experimental evidence [53, 40, 143] from solid density systems that the two temperature model still gives physical results for non-thermal distributions, by assuming a thermal distribution at the same energy. Consequently the overall behaviour of the system is not likely to be significantly affected by small deviations from thermal distributions.

One other point to briefly consider is the behaviour in the limiting cases of high and low interspecies coupling, i.e. large and small values of $G(T_e)$. When it is very low, the initial heating of the system contained in the term $S(\mathbf{r}, t)$ occurs on a timescale over which almost no interspecies energy transfer has taken place. Consequently, the source term can be approximated as a δ-function, with the subsequent evolution of the system determined wholly by the coupling parameter. At the other extreme, however, with either high coupling or slow energy deposition, energy can be transferred between the species almost as fast as it is being deposited by the source term. In such cases, the electron and ion temperatures can remain almost identical throughout the energy deposition, with no initial highly non-equilibrium state. This makes finding an exact value for the coupling parameter much more difficult, as larger values will make increasingly little difference.

[2]As an example, the relevant energy transfer rates in the tantalum sample used at Titan were $\sim 10^3$ W for conduction, compared to $\sim 10^{10}$ W from the electrons into the ions

4.3 Forms for $G(T_e)$

We will now consider some of the approaches to obtaining values for the coupling parameter $G(T_e)$. Although they are, in general, appropriate for different systems, they will be presented for comparison and to illustrate the different ways that the physics can be approached.

4.3.1 Metallic Relaxation

This first model, that of Allen [1], was developed to describe the energy exchange between the electrons and lattice in metallic materials at low temperatures by considering electron-phonon collisions. We begin by taking the Bloch-Boltzmann-Peirels formulæ, the derivation of which can be found in e.g. Ziman [177]:

$$\begin{aligned}\left[\frac{\partial f_k}{\partial t}\right] = &-\frac{2\pi}{\hbar}\sum_Q |M_{k\,k'}|^2 \times \\ &\Big\{ f_k(1-f_{k'})\Big[(n_Q+1)\delta(\varepsilon_k-\varepsilon_{k'}-\hbar\omega_Q)+n_Q\delta(\varepsilon_k-\varepsilon_{k'}+\hbar\omega_Q)\Big] \\ &-(1-f_k)f_{k'}\Big[(n_Q+1)\delta(\varepsilon_k-\varepsilon_{k'}+\hbar\omega_Q)+n_Q\delta(\varepsilon_k-\varepsilon_{k'}-\hbar\omega_Q)\Big]\Big\}\end{aligned} \tag{4.2a}$$

$$\left[\frac{\partial n_Q}{\partial t}\right] = -\frac{4\pi}{\hbar}\sum_k |M_{k\,k'}|^2 f_k(1-f_{k'})\Big[n_Q\delta(\varepsilon_k-\varepsilon_{k'}+\hbar\omega_Q)-(n_Q+1)\delta(\varepsilon_k-\varepsilon_{k'}-\hbar\omega_Q)\Big] \tag{4.2b}$$

These describe the evolution of the distribution functions for the electrons (f_k) and phonons (n_Q) in terms of their quantum numbers k, Q, within one unit cell. $|M_{k\,k'}|$ are the electron-phonon matrix elements, which describe the probability of scattering an electron from the initial state k with energy ε_k to final state k' with energy $\varepsilon_{k'}$ by interaction with a phonon of energy $\hbar\omega_Q = \varepsilon_k - \varepsilon_{k'}$. The factor of 2 difference between the equations accounts for the electron spin degeneracy.

These equations fully characterise the future evolution of the distribution functions as long as three conditions are met: that diffusion due to spatial inhomogeneity, i.e. conduction, is negligible; that acceleration due to both external and internal fields is negligible; and that no other collision processes are important. The first, as mentioned above, is assumed to be true due to the short time- and length-scales of the systems probed, and the second is true after the initial heating is completed. For the third assumption, the only effect of other collisions (within, rather than between, species)

is to keep the individual distributions thermal (Fermi for the electrons, Bose-Einstein for the phonons), and characterised by a single temperature for each species T_e or T_i i.e.:

$$f_k = \{\exp[(\varepsilon_k - \mu)/k_B T_e(t)] + 1\}^{-1} \tag{4.3a}$$

$$n_Q = \{\exp[\hbar\omega_Q/k_B T_i(t)] - 1\}^{-1} \tag{4.3b}$$

with μ the chemical potential or, at low energies, the Fermi energy. As described above, the differences due to non-thermal distributions are relatively small, and so we will take this third assumption to be valid for the systems considered.

From Equation (4.2), a form for the rate of change on energy in the electrons due to electron-phonon scattering processes can be derived:

$$\left.\frac{\partial E_e}{\partial t}\right|_{ep} = \frac{4\pi}{\hbar}\sum_{k\,k'} \hbar\omega_Q |M_{k\,k'}|^2 \left[S(k,k')\right] \delta(\varepsilon_k - \varepsilon_{k'} + \hbar\omega_Q) \tag{4.4a}$$

$$[S(k,k')] = (f_k - f_{k'})\, n_Q - f_{k'}\,(1 - f_k) \tag{4.4b}$$

with $S(k,k')$ the so-called 'thermal factor' which accounts for phonon absorption and emission.

At low temperatures, the electron interactions will all take place near to the Fermi surface, and work done in superconductivity theory can be used to simplify the form of Equation (4.4), as is done by Allen [1]. This uses the Eliashberg spectral function α^2F:

$$\alpha^2 F(\varepsilon_k, \varepsilon_{k'}, \omega) = \frac{2}{\hbar g(\varepsilon_F)} \sum_{k\,k'} |M_{k\,k'}|^2 \tag{4.5}$$

with $g(\varepsilon_F)$ the density of electron states at the Fermi energy.

This function varies with $\varepsilon_k, \varepsilon_{k'}$ on much larger scales than the variation with ω, such that these can be neglected leaving $\alpha^2F(\varepsilon_k, \varepsilon_{k'}, \omega) = \alpha^2F(\omega)$. When substituted into Equation (4.4) we obtain, after performing the integrals over ε_k and $\varepsilon_{k'}$:

$$\left.\frac{\partial E_e}{\partial t}\right|_{ep} = 2\pi g(\varepsilon_F) \int_0^\infty \alpha^2 F(\omega)(\hbar\omega)^2 \left[n(\hbar\omega, T_i) - n(\hbar\omega, T_e)\right] d\omega \tag{4.6}$$

By Taylor expanding the Bose-Einstein distribution, this can be further simplified with the assumption that $\hbar\omega \ll k_B T_e$ and $\hbar\omega \ll k_B T_i$. This leads to:

$$\left.\frac{\partial E_e}{\partial t}\right|_{ep} \approx G_0(T_i - T_e) \tag{4.7a}$$

$$G_0 = \pi\hbar k_B \lambda \langle\omega^2\rangle g(\varepsilon_F) \tag{4.7b}$$

Comparing to the two-temperature model above, we see that the constant value G_0 is just the electron-ion coupling parameter already defined. The quantities $\langle\omega^2\rangle$ and λ are, respectively, the second moment of the phonon spectrum and the electron-phonon mass enhancement parameter. The former is defined by McMillan [102], again in work looking at superconductivity, while the latter is the first reciprocal moment of the spectral function defined above: $\lambda\langle w^2\rangle = 2\int_0^\infty d\Omega\,\Omega\,\alpha^2F(\Omega)$. Values for the product of these quantities can also be found in [102]. This means that we can calculate values for the strength of the electron-ion coupling under conditions with 'low' temperatures, such that the collisions occur near to the Fermi surface, but sufficiently high that the assumption made in expanding the distribution is justified.

To better account for the behaviour at high temperatures, electrons beyond the Fermi surface, i.e. with $\varepsilon > \varepsilon_F$, need to be accounted for, and therefore the energy dependence of $|M_{k\,k'}|^2$ needs to be calculated, or at least approximated. The work of Wang *et al.*[163] proposes an approach based on the assumption that the quantity is independent of electron states when summed over scattering angles. This leads to:

$$\alpha^2F(\varepsilon, \varepsilon', \Omega) = \left[\frac{g(\varepsilon)\,g(\varepsilon')}{g^2(\varepsilon_F)}\right] \alpha^2F(\varepsilon_F, \varepsilon_F, \Omega) \tag{4.8}$$

with $g(\varepsilon)$ the density of states at energy ε. Substituting this in, we obtain a relatively simple form for a temperature dependent version of the expression found in (4.7)

$$G(T_e) = \frac{\pi\hbar k_B \lambda\langle\omega^2\rangle}{g(\varepsilon_F)} \int_{-\infty}^{\infty} g^2(\varepsilon) \left(-\frac{\partial f}{\partial \varepsilon}\right) d\varepsilon \tag{4.9a}$$

$$= G_0 \int_{-\infty}^{\infty} \frac{g^2(\varepsilon)}{g^2(\varepsilon_F)} \left(-\frac{\partial f}{\partial \varepsilon}\right) d\varepsilon, \tag{4.9b}$$

Near to room temperature, where electrons above the Fermi surface can be ignored, $-\partial f/d\varepsilon \approx \delta(\varepsilon - \varepsilon_f)$ and the expression reduces to simply G_0. At higher temperatures, however, the term becomes non-negligible as electrons with energies significantly far from the Fermi level contribute.

In the original paper by Wang that proposed this method, this change in occupation levels was equivalent to d-band electrons being excited into the conduction band, giving a significant change in $g(\varepsilon)$ at the energies reached. This in turn led to an increase in $G(T_e)$ of around a factor of 6 between room temperature and $T_e = 1$ eV.

Further results using this approach are found in the paper by Lin *et al.* [96]. This gives examples of $G(T_e)$ increasing, decreasing or behaving non-monotonically with increasing electron temperature in different elements. What should be noted, though, is that these values are only reasonable while the ions in the materials still have a lattice structure; once it melts there are, of course, no longer phonons to interact with and other models must be sought to calculate the exchange rate.

4.3.2 Landau-Spitzer Theorem

While the model described above considers energy transfer due collisions between electrons and the lattice phonons, the collective oscillations of the ions in the material, at the opposite end of the spectrum of materials for consideration is Spitzer's theory[148]. In this model, the energy transfer occurs between the electrons and freely moving ions. Clearly, this is not relevant for the solid metallic elements described above, but rather, best describes the behaviour of ideal plasmas (or fully ionized gases, in the nomenclature of the time).

Following the original derivation of Spitzer, and working from the diagram of a pairwise collision given in Figure 4.1, the angle ϕ is given by $\tan\phi = \frac{Mpu^2}{ZZ_1e^2}$ with the reduced mass $M = (1/m + 1/m_1)^{-1}$, the relative velocity $\mathbf{u} = \mathbf{v} - \mathbf{v}_1$ and Z, Z_1 the respective charges on the particles. p, the impact parameter, is the distance of closest approach in the absence of interparticle forces.

Since we are looking at electron-ion energy exchange, we choose $Z = e$, $Z_1 = Z_i e$ and $M_1 \gg m$. We consider a significant deflection to be one where $\chi > 90°$, and find that maximum the impact parameter for such a 'close collision', defined as p_0, is:

$$p_0 = \frac{Z_i e^2}{m_e v^2} \tag{4.10}$$

with v the electron velocity throughout this derivation.

In this case, the potential energy at closest approach is twice the initial kinetic energy of the electron, and the cross section for the scattering is πp_0^2. We can then define the time interval between collisions as $t_c = (\pi n_i v_e p_0^2)^{-1}$ with n_i the ion number density. While this is a reasonably accurate model for gases, it is a very poor model for even ideal plasmas as the biggest effect on the electron paths is not infrequent,

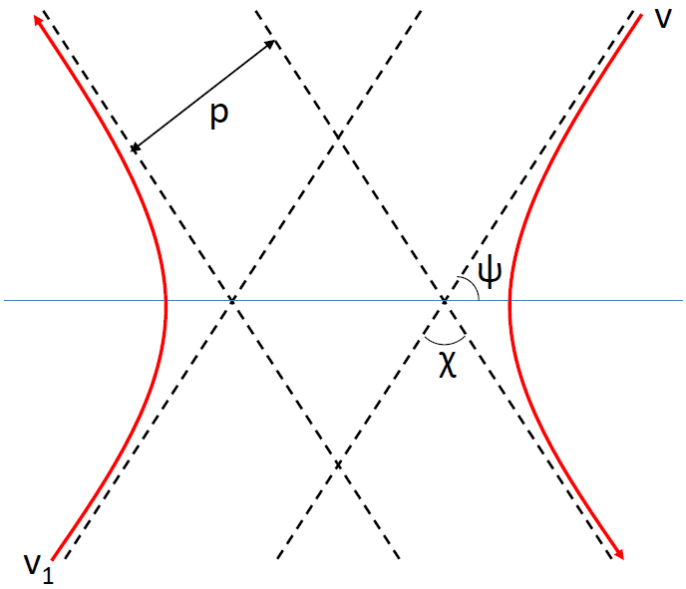

Figure 4.1: Values relevant for defining scattering of two particles, initial velocities v and v_1, due to Coulomb repulsion. The impact parameter p is the distance of closest approach in the absence of the repulsive force.

large-angle interaction, but instead large numbers of small angle deflections. This is because the potential between the electrons and ions in a plasma is much longer range than the Lennard-Jones potential that governs the interaction between neutral particles in a gas.

To describe the behaviour in a plasma, Spitzer uses diffusion coefficients which quantify the change in a test particle, i.e. electron, velocity due to cumulative interactions. If we consider the change in velocity perpendicular to the original direction, the average will, by symmetry, be 0, so instead we can calculate the average square change in the velocity:

$$\begin{aligned}(\Delta v_\perp)^2 &= v^2 \sin^2 \chi \\ &= v^2 \sin^2(\pi - 2\phi) \\ &= 4v^2 \sin^2 \phi \cos^2 \phi \\ &= \frac{4v^2(p/p_0)^2}{\left[1 + (p/p_0)^2\right]^2}\end{aligned} \tag{4.11}$$

To get an average value, we then integrate over the range of impact parameters, with the rate of impact per second between p and $p + dp$ being $2\pi v n_i dp$.

$$\langle(\Delta v_\perp)^2\rangle = 8\pi n_i v^3 p_0^2 \int_0^{p_m/p_0} \frac{x^3 dx}{(1+x^2)^2}$$
$$\approx 8\pi n_i v^3 p_0^2 \ln\left(\frac{p_m}{p_0}\right) \tag{4.12}$$

The full integral is in fact divergent, so a limit must be chosen for the value inside the logarithm, which is the ratio of the maximum and minimum impact parameters considered. Work by Cohen *et al.* [27] suggests that the Coulomb length λ_D is an appropriate choice for the maximum value, as beyond this point the repulsive force is screened by other charges in the system, an effect which is otherwise not accounted for here. The minimum is chosen here as p_0 as values below that lead to the large angle scattering which this model assumes to not contribute significantly (due to their infrequency). We also replace the kinetic energy with the average value, such that $mv^2 \to 3kT_e$. This gives a value for the quantity inside the logarithm:

$$\Lambda \equiv \frac{\lambda_D}{p_0} = \frac{3}{2Z_i e^3}\left(\frac{k^3 T_e^3}{\pi n_e}\right) \tag{4.13}$$

The quantity $\ln\Lambda$ is known as the Coulomb logarithm, and varying the minimum and maximum values to account for additional interaction effects is one of the primary ways to attempt extend the validity of this model beyond the ideal plasma regime.

However, we will remain within the intial ideal plasma assumptions, and reproduce the expressions for each of the dispersion functions of the velocity distribution. These are given in terms of the error function $\Phi(x) = 2\pi^{-1/2}\int_0^x \exp(-y^2)dy$, the derived function $F(x) = \left[\Phi(x) - x\Phi'(x)\right]/(2x^2)$ and the quantities $A_D = 8\pi e^4 Z_i \ln\Lambda/m_i^2$ and $x = \sqrt{mv^2/(2kT_e)}$:

$$\langle\Delta v_\parallel\rangle = -A_D \frac{m_e}{2kT_e}\left(1+\frac{m_e}{m_i}\right)F(x) \tag{4.14a}$$
$$\langle(\Delta v_\parallel)^2\rangle = \frac{A_D}{v}F(x) \tag{4.14b}$$
$$\langle(\Delta v_\perp)^2\rangle = \frac{A_D}{v}\left[\Phi(x) - F(x)\right] \tag{4.14c}$$

The first of these equations describes the change in velocity parallel to the initial direction - this is generally going to be negative, and describes the slowing, or viscous, effect of the plasma on the electrons. The other expressions govern the rate at which the electron velocity distribution approaches the equilibrium Maxwell-Boltzmann distribution.

Now, having expressions for the changes in velocity, we can calculate how much energy is being lost from the electrons due to these processes. From simple expressions for the kinetic energy we see that:

$$\Delta E = \frac{m}{2}\left\{2v\Delta v_{\parallel} + \left(\Delta v_{\parallel}\right)^2 + \left(\Delta v_{\perp}\right)^2\right\} \tag{4.15}$$

Expanding this equation and multiplying by the electron number density, we find an expression for the coupling constant G:

$$G = \frac{8(2\pi)^{1/2} n_e n_i Z_i^2 e^4}{3 m_e m_i}\left(\frac{kT_e}{m_e} + \frac{kT_i}{m_i}\right)^{-3/2} \ln\Lambda \tag{4.16}$$

We can see that, in this case, the dependence is on both the electron and ion temperatures, as both species are moving, although except in the case of systems with $T_i \gg T_e$ the inverse masses mean that the ion temperature makes a much smaller difference to the value.

Approaches to extending the validity of this model generally focus on varying the parameters in the Coulomb logarithm e.g. Brysk [15], Gericke *et al.* [57]. Values for these can be chosen to fit values obtained from molecular dynamics situations, but this is still limited to values of $\Gamma \lesssim 0.1$. Consequently, other models are still needed when attempting to describe the dense ionized systems that are considered in this work.

4.3.3 Quantum Statistical Approaches

The final models considered are significantly more complex that the previous ones, but are also the most relevant in the materials and under the conditions that are of the greatest interest. Rather than considering the motion of a single test particle, they treat the whole system quantum statistically to evaluate $\langle \dot{H}_e \rangle$, the rate of change of the expected value of the electron subsystem Hamiltonian. The linking between the electron and ion subsystems distinguishes the Fermi Golden Rule (FGR) and Coupled Mode (CM) approaches - in FGR, they are treated as weakly coupled such that the response function of one can be calculated without considering changes in the other. In CM, on the other hand, interactions between density fluctuations in each of the subsystems are considered dynamically.

These approach is fundamentally different from that using single-particle kinematics, although the values obtained will converge in appropriate limiting situations[21].

Results from the FGR and CM models tend to agree with each other, only diverging in extreme conditions where the effects of interspecies mode coupling become significant.

To obtain an expression for $\langle \dot{H}_e \rangle$, we take the commutator mean value:

$$\langle \dot{H}_e \rangle = \langle [H_e, H] \rangle \tag{4.17}$$

with H the Hamiltonian for the entire (electron and ion) system.

In the simplest evaluation, this become a FGR calculation, the derivation of which was first done by Dirac [34]. It says that, if a system described by a given Hamiltonian H in eigenstate $|i\rangle$ is perturbed by an additional Hamiltonian that oscillates with frequency ω, then the system can move to a state $|f\rangle \in |F\rangle$, where $|F\rangle$ is the set of states with energy $\pm\hbar\omega$ different from the original state. The probability per unit time of this occurring, to first order in the perturbation, is

$$P_{i \to f \in F} = \frac{2\pi\rho}{\hbar} |\langle f | H' | i \rangle|^2 \tag{4.18}$$

with ρ the density of possible final states per unit energy.

In the systems we are considering, the perturbing Hamiltonian can be an oscillation in either the ion or electron subsystem, with the frequencies for the possible collective modes being contained in the respective spectral functions $A_i(\mathbf{k}, \omega), A_e(\mathbf{k}, \omega)$. These spectral functions are defined uniquely by the dynamic structure factors for the electron and ion subsystems ($a = e, i$) through

$$S_a(\mathbf{k}, \omega) = \frac{1}{2\pi} N_B(-\omega, T_a) A_a(\mathbf{k}, \omega) \tag{4.19a}$$

$$A_a(\mathbf{k}, \omega) = -2 \operatorname{Im} \chi_a(\mathbf{k}, \omega) \tag{4.19b}$$

with a denoting the subsystem and $N_B(\omega, T_a)$ a Bose distribution describing the occupation of the possible spectral states at the temperature of the system [33]. The value $\chi_a(\mathbf{k}, \omega)$ is, as defined in Chapter 2, the density response function for the system being considered and so it can be seen that, at small ω then $N_B(\omega, T_a) \to k_B T_a / \hbar\omega$ and these expressions reduce to the fluctuation-dissipation theorem, Equation (2.47).

In the work by Dharma-Wardana and Perrot [33] they start by assuming an ion spectral function consisting of a single mode at frequency $w_{\mathbf{q}}$:

$$A_i(\mathbf{k}, \omega) = -2\pi \left[\delta(\omega - \omega_{\mathbf{q}}) - \delta(\omega + \omega_{\mathbf{q}}) \right]$$

This gives an expression for the energy exchange with the electrons due to this single mode, which is then integrated over the frequency range to give the full expression, which is reproduced here:

$$\frac{\partial E_{ele}}{dt} = \int_0^\infty \frac{\omega\, d\omega}{2\pi} \int \frac{dq^3}{(2\pi)^3} \left|U_{ie}(\mathbf{q})\right|^2 \Delta N_{ei} A_e A_i \tag{4.20a}$$
$$\Delta N_{ei} = [N_B(\omega, T_e) - N_B(\omega, T_i)]$$

with $U_{ie}(\mathbf{q})$ the electron-ion pseudopotential.

We can see that the rate of energy exchange is proportional to the population imbalance in modes that share an energy, and that we can therefore define a relaxation time for the population of each mode $P_{\mathbf{q}\omega}$ according to the rate equation

$$\frac{\partial P_{\mathbf{q}\omega}}{\partial t} = \frac{[N_B(\omega, T_e) - N_B(\omega, T_i)]}{\tau_{\mathbf{q}\omega}} \tag{4.21a}$$
$$\tau_{\mathbf{q}\omega} = \left[\left|U_{ie}(\mathbf{q})\right|^2 A_e\right]^{-1} \tag{4.21b}$$

In the limit where the energies of the modes $\hbar\omega$ are significantly smaller than the thermal energy $k_B T_a$, which is relevant for the dominant modes in the system, then the Bose distribution reduces to a fraction and the temperature difference can be factorised out, to give an expression in the form of the two temperature model

$$\Delta N_{ei} \to \frac{T_e}{\omega} - \frac{T_i}{\omega} \tag{4.22}$$
$$G \to \int_0^\infty \frac{d\omega}{2\pi} \int \frac{dq^3}{(2\pi)^3} \left|U_{ie}(\mathbf{q})\right|^2 A_e A_i \tag{4.23}$$

This expression can be used as a value for modelling or analyzing experimental data, with the additional assumption that G is constant throughout the experiment. Other approaches would be to recalculate the spectral function and pseudopotential as functions of temperature across the parameter space of the experiment, which would rapidly become computationally prohibitive for even a simple model.

Turning now to the case of considering the coupled modes within the system, we find an expression that is very similar to (4.20). However, instead of separate spectral function A_e, A_i coming from well-defined, non-interacting density response functions for each species, a DRF for the entire system has to be considered. Rather than the DRF, this is generally ([160],[21]) written in terms of the dielectric functions, both those for individual species, $\varepsilon_a(\mathbf{k}, \omega) \propto \chi_a^{-1}(\mathbf{k}, \omega)$, and that for the system as a whole $\varepsilon(\mathbf{k}, \omega)$, with a corresponding definition.

For comparison, we now have values for the rate of energy exchange under the FGR and CM approaches, written in comparable terms:

$$\left.\frac{\partial E_{ele}}{dt}\right|_{FGR} = \int_0^\infty \frac{\omega\, d\omega}{2\pi} \int \frac{dq^3}{(2\pi)^3} \left|U_{ie}(\mathbf{q})\right|^2 \Delta N_{ei}\ \mathrm{Im}\,\varepsilon_e^{-1}(\mathbf{k},\omega)\ \mathrm{Im}\,\varepsilon_i^{-1}(\mathbf{k},\omega) \tag{4.24}$$

$$\left.\frac{\partial E_{ele}}{dt}\right|_{CM} = \int_0^\infty \frac{\omega\, d\omega}{2\pi} \int \frac{dq^3}{(2\pi)^3} \left|U_{ie}(\mathbf{q})\right|^2 \Delta N_{ei} \frac{\mathrm{Im}\,\varepsilon_e(\mathbf{k},\omega)\ \mathrm{Im}\,\varepsilon_i(\mathbf{k},\omega)}{|\varepsilon(\mathbf{k},\omega)|^2} \tag{4.25}$$

Due to the presence of a peak when $\varepsilon(\mathbf{k},\omega) = 0$, corresponding to the plasmon peak in the DSF, calculating values using these expressions can be very computationally expensive. There exist a variety of approaches to simplifying the calculation, which are outlined in e.g. [20], but will not be considered further here. Suffice to say that, even with simplifying assumptions made, these approaches considering the dynamics of both the electrons and ions in the system are significantly more robust than earlier calculations for systems under warm dense conditions.

4.4 Conclusions

This chapter has presented the basic model used to describe temperature equilibration in the systems considered in this thesis. Although it is a relatively simple model, various different approaches to quantifying the rate of energy exchange produce results which agree with the basic premise that $\partial E/\partial t \propto (T_e - T_i)$.

These different approaches deal with very different situations and, as we will see in the next chapter, produce very different results. The metallic model is based on a low-temperature approach and, as it considers energy exchange between electrons and phonons, cannot be applied to materials outside of the solid state. However, one of the main temperature diagnostics used in the following chapter is diffractive, and consequently can also only be used when a crystalline lattice still exists. Consequently, this model is one of the easiest to test in the experiments carried out.

The Landau-Spitzer model quantifies the energy exchange between free electrons and ions, and so is relevant for low-Γ plasmas. Although this is not expected to produce meaningful results for the systems that have been studied, it is informative to see how the problem was approached by the earliest work on the subject. It is also the case that, in the ideal plasmas that it is most suited to, it produces results which agree well with experimental results.

Finally, quantum statistical models based on the structural properties described earlier in the thesis were presented. These have been shown to produce results which agree well with molecular dynamics simulations of warm dense systems. The maths

of calculating values through these approaches is more complex, but the range of validity is correspondingly much greater.

Chapter 5

Equilibration Results

In the introduction to the previous chapter we saw that, to study the properties of warm dense matter produced by charged particle heating, sufficient time must be allowed for the material to reach temperature equilibrium if the results obtained are to be related to natural cases. The chapter went on to outline models for describing the rate of energy exchange between the ion and electron species in the materials, and consequently the timescales needed for the material to reach equilibrium.

This chapter looks at the experiments we carried out to directly measure the rate of energy exchange, with the results compared to some of the models described. We begin with descriptions of some of the experimental methods used to study these phenomena, including the method used to generate proton beams, and how x-ray diffraction can be used to measure the temperature of the ion subsystem.

We then move onto the experiments themselves; the first two campaigns studied graphite, using first proton heating, on the Titan laser, and then electron heating, on the PHELIX laser. The next was carried out on a smaller facility, in our own lab in Oxford. This used direct laser irradiation and only probed very weak sample heating. The final experiment was again on the Titan laser, looking at a variety of materials, but with quantitative results only obtained for tantalum.

5.1 Experimental Methods

5.1.1 X-ray Line Radiation

In the description of FELs we noted that, prior to their development, monchromatic X-rays were mostly generated from laser-matter interactions. The particular sources

used here are generally K-α sources, meaning that they are due to emissions from electrons moving from the L-shell ($J = 2$) to the K-shell ($J = 1$) [155].

Such emissions are generated when an intense, ultrashort (sub-ps) pulse is incident on a solid target; this is absorbed within the skin depth at the laser wavelength, heating the electrons to hundreds of eV and creating a plasma. Over the timescale of the laser pulse, the laser-plasma interaction drives fast electrons into the material and excites inner shell electrons. As these holes are filled, the characteristic line radiation is emitted [136].

Without other sources available, much work was done in improving the yields and conversion efficiencies of such sources. This found that the best results were obtained away from best focus [134] and with thin ($\sim \mu$m) foils [131], due to the significance of refluxing in generating the desired radiation [121]. This occurs when electrons are driven from the far side of the target, leaving a net positive charge in the target and attracting the electrons back into the sample, where they then emit further radiation [114]. This lengthens the duration of the emission, but also significantly increases the total flux.

These sources were used on many experiments in the warm dense and high energy density regime e.g. [122] [59] [97], including Thomson scattering experiments, and continue to be so used due to the scarcity of XFELs. The main drawback, apart from the lower brightness, is the other radiation produced, both in the form of *bremsstrahlung* X-rays across a broad range of energies, and charged particle radiation, both of which add significantly to the noise in any results obtained. Although shielding can be used to mitigate these effects, they do still present a significant challenge to experimental design and analysis.

5.1.2 Target Normal Sheath Acceleration

While the benefits of using charged particles to heat samples have already been expounded, the use of protons in particular is highly advantageous. The reasons for this include being easy to measure using diagnostics such as Thomson spectrometers or radiochromic film, and the deposition of energy in different materials being well understood [124].

Such beams can be generated in the lab by interacting a high-intensity laser with a solid target.The x-rays that we then use to probe the heated sample can be generated in a similar way and so this process, known as target normal sheath acceleration, is

frequently used in experiments where an incoming laser is split in a 'pump-probe' configuration. One part of the beam creates the heating source, and the other generates X-rays as a diagnostic.

Accelerating protons in this specific way was first observed by Hatchett *et. al.* in 2000 [74], although ion acceleration from ps laser interactions had been observed previously [45],[146]. Hatchett used beams of 1 μm light, delivering several hundred joules with intensities up to 3×10^{20} W cm^{-2} onto solid targets, and diagnosed the emitted photon, electron and ion beams. Nearly half of the laser energy was converted to a broad beam of hot electrons, but they also saw a highly luminous beam of ions, comprising mainly protons, that travelled almost exactly normal to the target rear surface, and containing particles up to several MeV. This was explained by the hot electrons forming a Debye sheath with fields of $\sim$MV/μm, accelerating protons and ions from contaminant layers of water vapour and hydrocarbons on the surface.

Target normal sheath acceleration (TNSA), is now a well-established (e.g. [12], [99]) method for creating highly collimated beams of protons with smooth angular distribution and very short duration (on the order of the drive beam, i.e. $\sim$ps). Further work by e.g. Fuchs *et al.* [52] and Passoni *et al.* [123] has looked at how the emitted spectra scale with laser energy, target thickness and other parameters. They found that a fluid model for the sample, derived from the work of Mora [109], can fit observed data with a good degree of reproducibility.

The results that they found relied on the fact that, in generating such a powerful laser pulse, the laser will also naturally produce amplified spontaneous emission, giving long-duration, lower energy laser irradiation before the main pulse. This ionizes the target, generating a pre-plasma, the electrons of which are then accelerated by the main pulse. Experimental results suggest that these electrons are accelerated thermally, with spectral temperature T_{hot} equal to the laser ponderomotive potential

$$T_p = m_e c^2 \left[(1 + I\lambda_{\mu m}^2 / 1.37 \times 10^{18})^{1/2} - 1 \right] \tag{5.1}$$

where I is the laser intensity in W cm^{-2} and $\lambda_{\mu m}$ the wavelength in microns, with m_e and c the electron mass and speed of light, as usual. The quantity $I\lambda^2$ appears frequently in work on laser-matter interactions, and is a significant scaling quantity in laser-matter interactions, as it is equal to the kinetic energy of a particle accelerated by the radiation field.

The form of the spectrum in the fluid model is:

$$dN/dE = \left[n_{e0} c_s t_{acc} S_{sheath}/(2ET_{hot})^{1/2}\right] \exp\left(-(2E/T_{hot})^{1/2}\right) \tag{5.2}$$

$$= \left[A/(2ET_{hot})^{1/2}\right] \exp\left(-(2E/T_{hot})^{1/2}\right) \tag{5.3}$$

where n_{e0} is the accelerated electron density, c_s the sound speed in the material, $t_{acc} = 1.3\, t_{laser}$ the effective acceleration time and $S_{sheath} = \pi(r_0 + d \times \tan\theta)^2$ the surface area of the 'sheath' of accelerated electrons on the target rear surface. The value A is fixed for a given laser intensity, and is later used as a fitting parameter.

The model also predicts a maximum proton energy depending on the effective acceleration time, normalized to the period of ion osciallations in the plasma. This maximum energy is equal to:

$$E_{max} = 2T_{hot}\left[\ln(t_p + (t_p^2 + 1)^{1/2})\right]^2 \tag{5.4}$$

$$t_p = \frac{\omega_{pi} t_{acc}}{(2e)^{1/2}} \tag{5.5}$$

At the laser energies and pulse lengths considered within this work, this model has been found to agree well with published results, and consequently is used as a model for fitting in the work on the experiment at Titan.

5.1.3 Debye-Waller Effect

In his book on X-ray diffraction [164], Warren describes the effect of temperature on diffraction results as 'a nuisance'. This is because it tends to reduce the intensity of the crystal reflections, and can be difficult to account for in determining crystal structure from obtained spectra. In the work carried out here, on the other hand, this reduction in intensity is incredibly useful, as it allows a direct measure of the lattice temperature in the sample being probed, at a temporal resolution equal to the duration of the X-ray pulse. This is because the relationship between the reduction in diffracted intensity and the temperature is well understood, although far from trivial to calculate, and so by observing this drop in intensity we obtain the temperature of the lattice.

To show this, we follow the derivation of Warren and begin with the definition of the diffracted intensity from a simple crystalline sample:

$$I_0 = I_{in} \sum_n F_n e^{i\mathbf{k}\cdot\mathbf{r}_n} \sum_n F_n' e^{-i\mathbf{k}\cdot\mathbf{r}_n'} \tag{5.6}$$

In this equation, F_n are the atomic form factors, describing the distribution of electrons around the atom, $\mathbf{r}_n$ are the (zero temperature) ion positions i.e. the lattice sites, and $\mathbf{k}$ is the wavevector of the diffraction, as defined in (1.6a).

Although it will not be considered in this discussion of the Debye-Waller factor, which accounts for the effect of ion motion on the diffracted intensity, the quantity F_n also varies directly with temperature; as the ion gains energy, the electrons favour more excited states and so the ion becomes, on average, more ionized. This effect is discussed, where relevant, in the results obtained from experiments but is found to be small on the temperature scales probed.

The direct effect of temperature on the above expression is introduced by allowing the atomic position to vary due to thermal motion such that $\mathbf{r}_n \to \mathbf{r}_n + \delta_n$ where δ_n is the instantaneous displacement due to thermal motion. In this case, the change in intensity due to considering the effect of thermal motion will be:

$$I/I_0 = \left\langle e^{i\mathbf{k}\cdot(\delta_n - \delta_{n'})} \right\rangle \tag{5.7a}$$

$$= \left\langle e^{ik(u_n - u_{n'})} \right\rangle \tag{5.7b}$$

where u_n is the component of the displacement parallel to the scattering vector $\mathbf{k}$, and therefore perpendicular to the diffracting plane.

In the case that the exponent in (5.7b) is small, identities for exponential functions allow us to write

$$\left\langle e^{ik\cdot(u_n - u_{n'})} \right\rangle = e^{-1/2 k^2 \langle u_n^2 \rangle} \times e^{-1/2 k^2 \langle u_{n'}^2 \rangle} \times e^{k^2 \langle u_n u_{n'} \rangle} \tag{5.8a}$$

$$= e^{-M} e^{-M'} e^{k^2 \langle u_n u_{n'} \rangle} \tag{5.8b}$$

This can then be incorporated into the expression for the intensity, with $M = M'$ for the case where only one type of atom is present, such as in the diffraction from elemental samples considered here. This leaves us with:

$$I/I_0 = e^{-2M} + e^{-2M} \left(e^{k^2 \langle u_n u_{n'} \rangle} - 1 \right) \tag{5.9}$$

with $M = -1/2\, k^2 \langle u_n^2 \rangle$. The first term describes the reduction in intensity of the main diffracted peak due to the lattice temperature: the Debye-Waller effect that we are most interested in. The second term represents temperature diffuse scattering and is itself a very interesting phenomenon which allows measurement of the spectrum of waves which can be supported by the lattice. However, the contributions are negligible in the situations considered here, and will therefore be ignored in this work.

We now have a relationship relating the diffracted intensity to the ion motion, but this is not, in and of itself, enough to give us a measure of the temperature. Indeed, relating the temperature of the system to the ion motion is not trivial, especially in crystals such as graphite with an anisotropic structure. To do so, we begin by considering any given wave in the sample to be composed of modes travelling parallel to the three base vectors of the crystal $\mathbf{e}_j$ with $j = 1, 2, 3$, with respective amplitudes a_j. The factor M then takes the form

$$M = \frac{1}{2} \sum_j (\mathbf{k} \cdot \mathbf{e}_j)^2 \langle a_j^2 \rangle \tag{5.10}$$

We can see from this that the reduction in intensity due to a given wave is greater when it is parallel to the wavevector of the diffraction, $\mathbf{k}$, and is proportional to the intensity, i.e. the average displacement of the atom out of the plane. Now, by assuming that the waves are sinusoidal with a frequency ω_j, we find that the average energy associated with a given wave is:

$$\langle E_j \rangle = \frac{1}{2} n_i m_i \omega_j^2 \langle a_j^2 \rangle \tag{5.11a}$$

$$= \left[\frac{1}{\exp(\hbar\omega_j / kT) - 1} + \frac{1}{2} \right] \hbar\omega_j \tag{5.11b}$$

with n_i, m_i the ion number density and mass, respectively, and the second expression written under the assumption that the energy per wave follows that of a simple harmonic oscillator.

Combining Equations (5.10) and (5.11) allows us to find an expression that relates the factor M to the ion temperature, by summing over all the waves in the lattice. Treating this directly as a sum is challenging, but the method of Debye, presented by James [84], allows this to be converted to an integral over the Brillouin zone, considered to be a sphere of radius g_m. Each wave is treated as either wholly transverse or longitudinal, and all waves of the same type assumed to have the same, averaged velocity V_j, a reasonable assumption in an isotropic crystal.

For each type of wave, the vibration direction $\mathbf{e}_j$ is oriented randomly relative to $\mathbf{k}$, and so for each wave terminating in the Brillouin zone, we can take the average for the term in (5.10):

$$\langle \mathbf{k} \cdot \mathbf{e}_j \rangle^2 = |\mathbf{k}|^2 \langle \cos^2(\theta) \rangle = \frac{k^2}{2} \tag{5.12}$$

With the volume[1] $V_{BZ} = \frac{4}{3}\pi g_m^3$, volume element $dV = 4\pi g^2 dg$ and density of points in the sphere N_i/V_{BZ}, the expression for M becomes:

$$2M = \frac{k^2\hbar}{N_i m_i} \sum_j \int_0^{g_m} \frac{1}{\omega_j} \left[\frac{1}{e^{(\hbar\omega_j/kT)} - 1} + \frac{1}{2} \right] \frac{3N_i}{4\pi g_m^3} 4\pi g^2 dg \tag{5.13}$$

To rewrite this equation such that the integral is performed over the frequency w_i, we note that, in terms of the constant velocity for each type of wave, $\omega_j = V_j \times 2\pi g$. The maximum frequency is therefore $\omega_{jm} = V_j \times 2\pi g_m$, which can be used to rewrite the equation in terms of ω_j.

$$2M = \frac{k^2\hbar}{m_i} \sum_j \frac{1}{\omega_{jm}^3} \int_0^{\omega_{jm}} \left[\frac{1}{e^{(\hbar\omega_j/kT)} - 1} + \frac{1}{2} \right] \omega_j d\omega_j \tag{5.14}$$

This is then simplified by expressing the frequencies in terms of characteristic energies for the (dummy) variable ω_j in the integral and for the maximum frequency, which now corresponds to a maximum energy mode, such that $\epsilon = \hbar\omega_j/k_B T$ and $x_j = \hbar\omega_{jm}/k_B T$, with k_B the usual Boltzmann constant. By substituting these into the equation, and with the definition of $\Phi(x)$ introduced by Debye:

$$\Phi(x) = \frac{1}{x} \int_0^x \frac{\epsilon d\epsilon}{e^\epsilon - 1} \tag{5.15}$$

Equation (5.14) becomes

$$2M = \frac{k^2 k_B T}{m} \sum_j \frac{1}{\omega_{mj}^2} \left[\Phi(x_j) + \frac{x_j}{4} \right] \tag{5.16}$$

This is now approaching a usable form, but the final step is to relate the maximum allowed energies ϵ_m to the characteristic temperatures, or Debye temperatures, $\Theta = \hbar\omega_m/k_B$. However, these temperatures depend on the lattice structure, and consequently can be different for longitudinal and transverse waves, and in the case of anisotropic crystals such as graphite, can also depend on the relative angle of the diffraction plane to the crystal.

To account for the types of wave, we define separate Debye temperatures $x_l = \Theta_l/T$, $x_t = \Theta_t/T$, and the expression for the factor $2M$ becomes

$$2M = \frac{k^2 k_B T}{m} \left\{ \frac{1}{\Theta_l^2} \left[\Phi(x_l) + \frac{x_l}{4} \right\} + \frac{2}{\Theta_t^2} \left[\Phi(x_t) + \frac{x_t}{4} \right] \right] \tag{5.17}$$

The factor 2 in the second term within the curly brackets is due to the fact that two of the three transverse wave directions give rise to particle motion normal to the

[1] NB This is a volume in the Brillouin Zone, and so has units $[m^{-3}]$

diffraction plane, as opposed to only one longitudinal wave direction. For simplicity, we use this fact to introduce an average Debye temperature Θ_M:

$$\frac{3}{\Theta_M^2} = \frac{1}{\Theta_l^2} + \frac{2}{\Theta_t^2} \tag{5.18}$$

This method of taking the average, while different from that in the Debye theory of specific heats, produces values which generally differ little from those obtained through the formal method, denoted Θ_D[2] We can then obtain a final expression for the Debye-Waller factor, with $x = \Theta_M/T$:

$$I/I_0 = e^{-2M} \tag{5.19a}$$

$$2M = k^2 \frac{3\hbar^2}{m k_B \Theta_M} \frac{1}{x} \left[\Phi(x) + \frac{x}{4}\right] \tag{5.19b}$$

One further consideration to note is that this calculation has been performed assuming only a small crystal sample, whereas in experiments the intensity measured will be the sum of diffraction from a larger crystal face. While accounting for this does change the value of the total diffracted intensity, it does not alter the change in intensity with increasing temperature - i.e. the intensity still decreases as e^{-2M}. Consequently, in experiments we can consider not the absolute value of diffracted radiation, but instead compare the intensities from heated and unheated regions of a sample to see the relative decrease. This also allows variation in the source intensity, which is often significant in laser-driven X-ray sources, to be accounted for.

5.1.3.1 Dynamic Diffraction

We now have an expression which described the change in diffracted intensity from a single crystalline layer; the effect of an extended face crystal is, as described above, accounted for and consequently the temperature can be extracted from diffracted X-rays if some part of the sample is at a known temperature. Another effect of the calculation above, though, is that this assumes that the crystal is only one single layer thick. This, perhaps surprisingly, remains a relatively good assumption for thick imperfect crystals with a high mosaicity. In these cases, a single X-ray is only likely to find one crystallite within the sample at the correct (Bragg) angle from which to diffract, so the other layers present have no effect, except to slightly decrease

[2]As Warren notes, the example of Germanium, where $\Theta_M \sim 0.8 \times \Theta_D$ is a significant exception, but as that element has not been used in any of this work, it will be ignored.

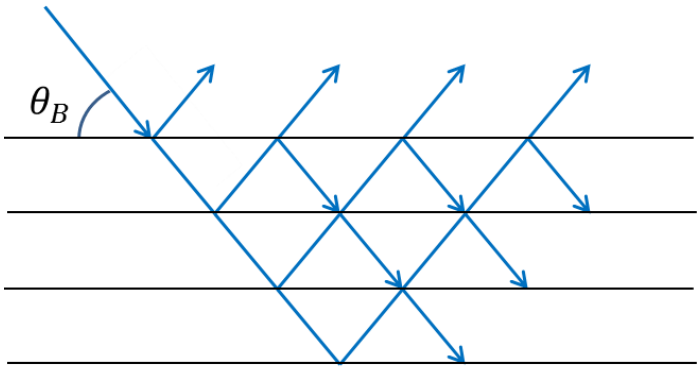

Figure 5.1: Illustration of the possible paths for a beam entering a perfect crystal. It can be seen that the intensity will be the sum of reflections off many planes.

the intensity due to absorption effects. These will be, on average, the same for any temperature and so the proportional decrease remains unchanged.

In the case of a perfect crystal, though, each plane of the crystal is at the same angle and consequently an X-ray which meets the Bragg condition with one layer will also do so with all the further layers below it, as illustrated in Figure 5.1. Using the above approximation, characteristic of the so-called 'kinematic' approach, can produce results which can deviate significantly in some crystals. Instead, a wholly different approach can be followed using a more rigorous 'dynamical' theory.

The full derivation will not be given here, but can be found in Warren, which itself takes it from the original work by Darwin in 1914 [30]. Much of the complexity comes from deriving the absolute value of the diffracted energy, which is found to be:

$$I/I_0 = \frac{8}{3\pi}\left(\frac{e^2}{mc^2}\right)\frac{N\lambda^2|Fe^{-M}|}{\sin 2\theta_B}\left(\frac{1+|\cos 2\theta_B|}{2}\right) \tag{5.20}$$

This accounts for the diffraction summed over small crystal cells, with N the number of cells per unit volume, and λ the wavelength, θ_B the Bragg angle and F the atomic form factor as before. It is interesting to note that the diffracted intensity from an entirely dynamic system is, in general, significantly less than that from the kinematic case due to the inherent angular dispersion of an incoming beam.

The most significant thing to note in Equation (5.20) is that the change in intensity with temperature, which is once again contained in the factor M, now only goes as e^{-M}. Therefore, not only do we have a small diffracted intensity, but it also changes less as the temperature increases.

5.2 Experiments

In the experiments here, the method of measuring the rate of temperature equilibration remains broadly similar. A laser beam is split between two arms in the 'pump-probe' configuration mentioned earlier in this chapter. One of these arms, the pump, heats the crystal target, either directly by laser irradiation, or by driving a beam of charged particles. The other arm, the probe, illuminates a thin metal foil to produce pseudo-monochromatic x-ray line radiation. This production takes place at a known delay after the probe beam has heated the target, and the strength of the diffracted signal is measured. This diffraction strength can then be related to the temperature of the ions in the target, as it decreases with temperature according to the Debye-Waller effect. This delay can be varied to give measurements of the evolution of the ion temperature over time. Correspondingly, the electron temperature can be calculated from simulations of the heating mechanism. As we will see in the analyses below, this is sufficient to define the electron-ion coupling parameter G.

5.2.1 Titan - August 2011

Although this experiment was carried out prior to my joining the experimental group, the results that were obtained are what motivated much of the work that follows, and so is included to give an appropriate context for the later results. Much of the discussion is taken from the paper by T. White *et al.* [170], who led the analysis of the results.

This experiment looked at the rate of electron-ion coupling in the high temperature limit of graphite - that is, close to the melting point but with the lattice structure still intact. This is significant because the structure of the ions potentially plays an important role in determining how quickly energy can be transferred, and because the structure of graphite gives it a variety of unique properties. Previous experiments which had investigated the interspecies energy transfer utilised an optical pump to heat the sample [83] [94] [151], creating a nonthermal distribution of electron in a nm-thick layer on the surface. As has already been mentioned, this method has a variety of potential drawbacks and so for this experiment a TNSA-driven proton beam was used instead.

The experiment took place on the Titan laser, using a 150 J beam in 10 ps, with a fundamental wavelength of $\lambda = 1054$ nm. 30% was incident onto a 10 μm thick Al foil, driving a proton beam through TNSA. These accelerated protons heated a graphite (HOPG) sample, below a 30 μm thick layer of polypropylene, used to stop

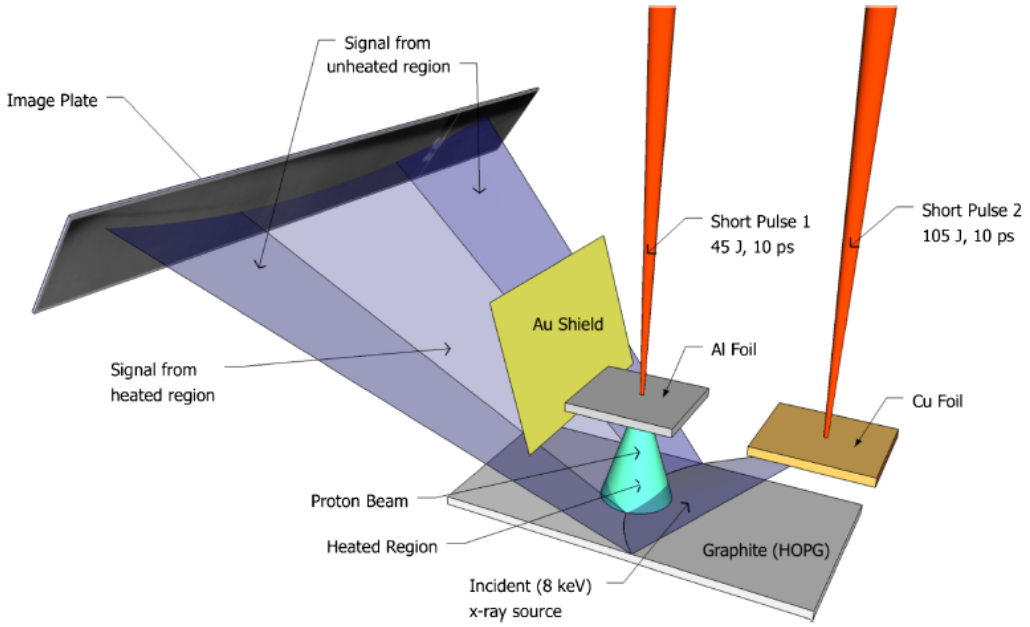

Figure 5.2: Schematic of experimental setup for Titan 2011 experiment.

low energy protons and heavy ions from giving additional heating, while also acting as a tamper to prevent expansion of the sample over the timescale of the experiment. The proton spectrum was measured on shots without a crystal in place, and scaled by the laser intensity. This spectrum was then used in a ray tracing simulation with energy deposition modelled with known stopping powers. This irradiation raised the electron temperature to $T_{max} \sim 1.5$ eV.

The remainder of the laser energy was focused onto a Cu foil, at a delay of 225 ps after proton creation, to drive the Cu K-α transition and give X-rays at $E_0 = 8047$ eV. These diffracted off the crystal sample at the Bragg angle of 27.4° and were detected on an image plate 30 cm away at a magnification of 138. The diffracted line on the detector was, as expected, observed to have a decrease in signal intensity in the regions corresponding to the heated area of the sample due to the Debye-Waller effect.

In these results, the intensity decreased to $\lesssim 20\%$ of that from the unheated regions. Using a Debye temperature of $\Theta_D = 800$ K taken from density functional theory calculations, it was found that the drop in intensity was consistent with an ionic temperature of around 0.3 eV at this delay. This was used in the two-temperature model, along with values for the heat capacities taken from PROPACEOS 4.2, an equation of state code based on a chemical model with additional adjustments taken from

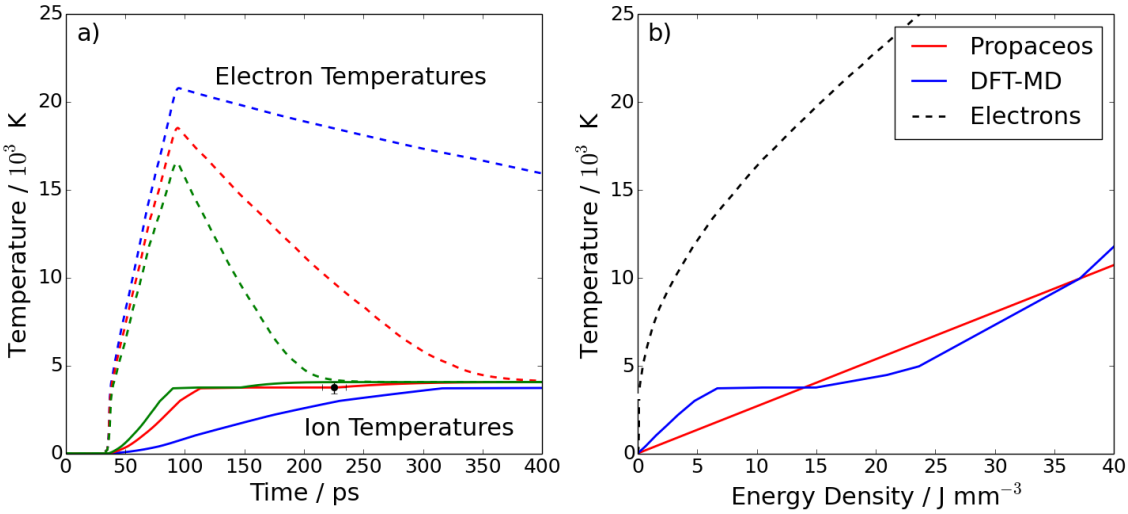

Figure 5.3: a) Electron and ion temperature evolution plotted for the best-fitting value for the electron-ion coupling (in red), and values a factor of two higher and lower (green and blue, respectively), with the experimental data point and error bars in black. b) EOS values for electrons and ions, calculated from PROPACEOS and DFT-MD. The flat region of the DFT-MD line is due to the latent heat of melting.

experimental data, and also from *ab initio* simulations of the electrons in a density functional theory calculation.

Figure 5.3 a) shows the evolution of the species temperatures from the proton arrival time at $t \sim 50$ ps. The best fit is found for $G = 0.54 - 0.66 \times 10^{16}$ W K^{-1} m^{-3}, with higher and lower values plotted for comparison. These results use the DFT-MD equation of state values for the lattice heat capacity, shown in 5.3 b), as those obtained from PROPACEOS do not account for the effect of latent heat, which is significant as the sample is close to melting.

Although the model used does not account for the variation of G with T_e over the timescale probed, the result can be reasonably interpreted as an average over this period. In Table 5.1 the results from the models outlined in the previous chapter, averaged over the temperatures probed, are presented. Those from the metallic coupling model are not included, due to the difficulty of accounting for the anisotropy of graphite in that model. It is clear that the models describe the behaviour of graphite very poorly. However, this cannot be considered to be entirely surprising - the Spitzer model should not work at solid densities, and the FGR and CM models depend on the existence of collective modes in both the electron and ion subsystems. While at least some of the electrons in graphite are delocalized, the ions are still in a lattice structure throughout the experiment, and so these models are also not appropriate

Model	**G (W K^{-1} m^{-3})**	**τ (ps)**
Spitzer	2×10^{18}	0.5
Fermi Golden Rule	6×10^{17}	1.5
Coupled Mode	5×10^{16}	18
Experimental	$6.0 \pm 0.6 \times 10^{15}$	150

Table 5.1: Predicted (averaged) values of G from models outlined in the previous chapter, compared to the experimental result obtained.

for the states probed. Adapting the metallic model for the more complex graphite hexagonal lattice could give better agreement, but such work is beyond the scope of this thesis.

5.2.2 PHELIX - May 2012

Following on from the work carried out at Titan, we wanted to once again probe the rate of energy exchange at the high-temperature limit of graphite, but with the addition of temporal resolution; that is, obtaining measurements of the ion temperature at a variety of delays to more accurately characterise the rate.

The experiment was carried out on the PHELIX laser (**P**etawatt **H**igh-**E**nergy **L**aser for Heavy **I**on **Ex**periments), at the GSI Helmholtz Institute in Darmstadt, Germany. As the name suggests, this is most often used in combination with the accelerator facility onsite (UNILAC), but also allows beam time for stand-alone laser beam experiments such as ours. The beam is a lower energy than that available at Titan (80 J vs. 150 J) but the shorter pulse length available (0.7 ps vs. 10 ps) makes for a significantly higher incident power.

As before, the beam was split in a pump-probe configuration, with the energy in this case split evenly between the heating drive and the Cu K-α X-ray source. Rather than protons, this experiment used electrons to heat the sample. Like protons, this avoids issues associated with direct laser heating, and also allows a more rapid creation of the heated state than that caused by proton time of flight effects. The drive beam was incident on the 200 μm thick Ti substrate in a 30 μm spot, driving electrons through the titanium and into a 50 μm thick highly oriented pyrolytic

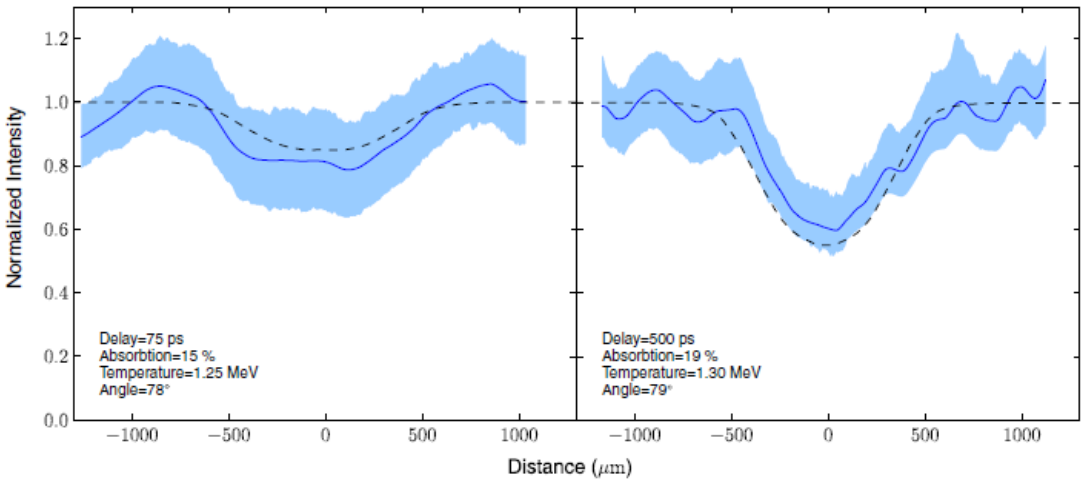

Figure 5.4: Relative Bragg scattering from heated region at delays of $t = 75$ ps and $t = 500$ ps, in blue, with experimental error indicated by the shaded region. The drop in intensity has grown significantly, indicating an increase in the temperature of the heated region. We can also see that it broadly agrees with the dashed line corresponding to predicted results from the ZEPHYROS code, using a value of $G = 0.20 \pm 0.05 \times 10^{16}$ W K^{-1} m^{-3} in the two-temperature model. The absorption, temperature and angle values characterise the fast electron distribution within the sample.

graphite layer on the rear surface (far side from the laser), which was the sample to be probed. The interaction of the pump laser arm with the Ti sets up strong radiation fields accelerating electrons to energies between 1 keV - 1 MeV. This non-thermal fast electron current passes into the sample, setting up resistive fields and return currents and losing energy to the surrounding material though collisions and Ohmic heating. At the same time, the energetic electrons produce x-ray radiation through bremsstrahlung and K-shell emission. This line radiation was detected on a spectrometer and used to derive an on-shot measurement of the temperature, energy and divergence of the hot electron population.

The second arm of the laser was delayed by up to 1 ns and irradiated a Cu foil in a 30 μm spot to drive the K-α transition at 8.047 keV. These x-rays then diffract off the target at first order ($\theta_B = 13.3°$) onto an image plate detector 10 cm away, at a magnification of 38. The foil was aligned such that it was edge-on to the target to reduce source broadening effects in the observed line. Similarly to the experiment at Titan, the reduced intensity from the heated region relative to the ambient surrounding gives a measure of the ionic temperature due to the Debye-Waller effect.

To fit the ion temperature data extracted from the diffraction, we use the 3D hybrid code Zephyros to model the energy deposition from the hot electrons in the sample, generating the source term in the two-temperature model. This code treats the electrons as the particles in a PIC (particle-in-cell) code, with the background of electrons and ions treated with a fluid model. The resistivity is taken from a reduced Lee-Moore model, matching room-temperature values in graphite. Zephyros also includes a K-shell emission rate, which was used to match the initial hot electron population to the K-α emission observed on the target rear surface. Since the absorbed energy, spectral temperature and angular divergence can be uniquely defined with this method, it can be used to generate the initial source term in the two temperature model.

This gives a source term of $S_R(t) \sim \delta(t) 6.9$ J mm^{-3}, and is assumed to be instantaneous compared to the timescale of equilibration, and homogeneous through the sample. Best agreement between the deposited energy from hot electrons and the measured ion temperatures was found with $G = 0.20 \pm 0.05 \times 10^{16}$ W K^{-1} m^{-3}.

The assumptions mde about the heating are worth examining in more detail, as the mechanisms for energy deposition in this case are significantly more complicated than in the previous case of protons [85]. Alongside the generation of the intense fast electron current, strong electric and magnetic fields are formed which could potentially produce large-scale instabilities and inhomogeneities in the sample heating. Despite these strong fields, though, the observed Ti K-α emission does not show the possible macro structure, and the simulations suggest that the current has decayed to negligible amounts within 2 ps, validating the assumption of instantaneity.

Once again, the measured value for the electron-ion equilibration is significantly lower than the predicted values. Although this is even lower than that obtained from the Titan experiment, this is to be expected from the lower electron temperatures as G is expected to increase with T_e. These results suggests that, while the energy relaxation does appear to be inhibited by the nonequilibrium condition of the sample, the mechanism by which it is put into such a condition may not affect the outcome.

5.2.3 Oxford Lab - October 2012

This experiment aimed to probe the rate of electron-ion equilibration in solid density gold, at near room-temperature conditions, using our own laser in the laboratory at Oxford. Rather than lasers delivering 10s of joules to heat systems, this delivers up to 40 mJ in a duration of 40-80 fs, giving an average power on the order of 1 TW. While this is still enough to give measurable effects on interacting with matter, and

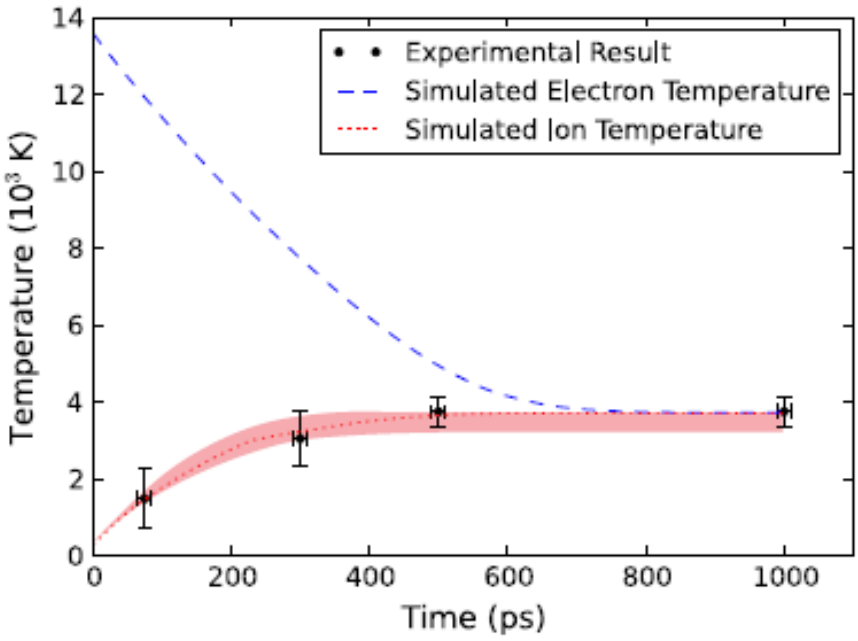

Figure 5.5: Electron and ion temperatures taken from the two temperature model with the best fit for the coupling coefficient. The red line was found with a source term of $S_R = 7$ J mm^{-3}, and the shaded region represents varying this value between $6 - 8$ J mm^{-3}.

crucially is still enough to drive the K-α transition and so give a usable X-ray probe, the range of conditions that it is possible to reach are significantly lower.

The experiment that we hoped to carry out was similar by that of Nicoul *et. al.* [116], from the University of Duisberg-Essen, albeit with the focus being on the electron-ion energy exchange. As shown in the schematic of the setup in Figure 5.6, the sample is a thin gold foil (∼200 nm), mounted on a mica substrate, heated by direct irradiation from the laser at 810 nm. The laser delivered 40 mJ per pulse, split equally between the pump and probe arms. The spot size on the gold foil was approximately 3 mm, giving an incoming laser fluence of 0.28 J/cm^2 and initial energy flux of 0.01 J/cm^2, after accounting for the high reflectivity of gold at 810 nm. The energy is initially deposited almost entirely into the electron subsystem, heating it isochorically and with thermalization of the electrons occurring over ∼0.25 ps. Energy is transferred from these heated electrons into the ion lattice modes, at a rate which we hoped to determine.

The other arm of the laser passed through a mechanical delay stage, with the difference in arrival time varying from -5 to +250 ps after the pump beam, with an error of ±1 ps (± 0.3 mm in the delay stage). It was focused by a $f/10$ parabola to

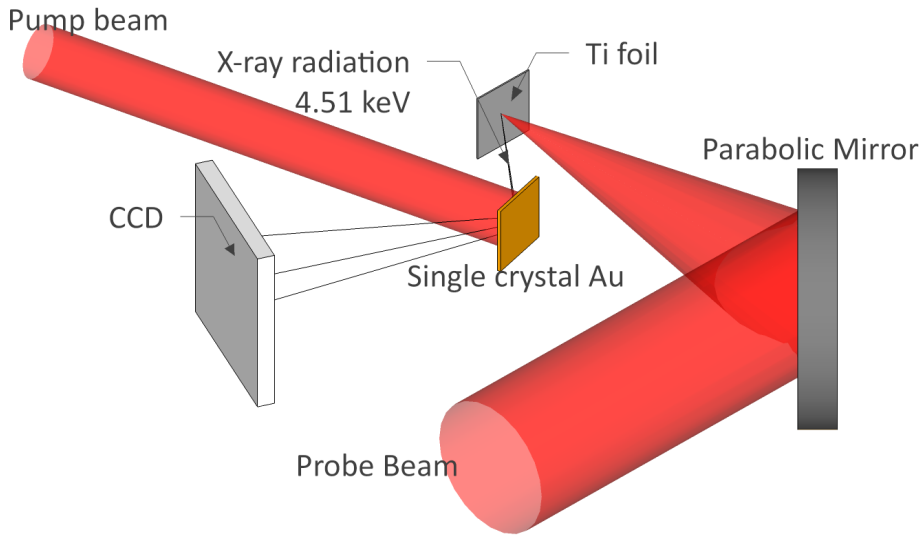

Figure 5.6: Schematic of the experimental setup used on our laser at Oxford. The pump beam heats the electrons in the single crystalline gold, and the plane separation is probed at a known delay by Ti K-α X-rays (4.51 keV) driven from a thin foil, and detected on a CCD.

a 50 μm spot on a 12.5 μm thick titanium foil, generating K-α X-rays at 4.51 keV. These then diffracted off the target, at a Bragg angle of 19.7°, and were detected on a CCD 10 cm from the crystal.

As the lattice gains energy and increases in temperature, the pressure correspondingly increases at a rate which, on the timescale of the ionic motion, is near instantaneous. This triggers a strain wave, giving an expansion in the material and consequently an increase in the lattice parameter a. This can be measured by observing a translation in the Bragg diffracted peak to smaller angles as the lattice expands, and then a periodic motion in the peak as the sound wave reverberates through the sample. For each shot, a Gaussian was fitted to the diffracted line and the central point used to calculate the diffraction angle. Multiple shots at each delay were used to estimate the uncertainty, with 12 shots taken for each delay from -5 ps to 40 ps, and 6 shots at other delays; these results are shown as the black points in Figure 5.7.

As in the earlier experiments, we use the two temperature model to describe the rate of energy flow from the heated electrons into the ions. Due to the very small changes of temperature involved, G was assumed to take a constant value. The heating was also assumed to be one-dimensional, as the pump laser spot was much larger than the thickness of the gold foil, giving a homogeneous sample for probing.

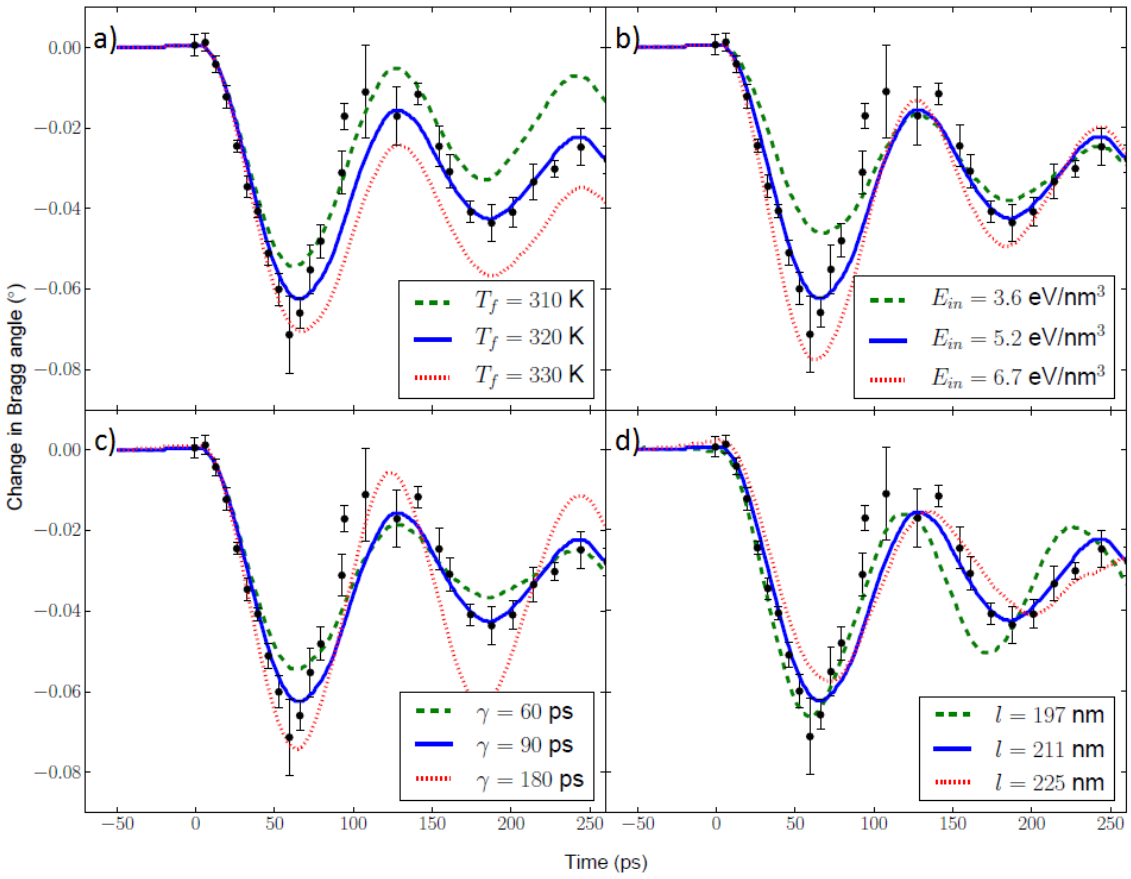

Figure 5.7: Observed change in angle of diffraction of the X-rays from the gold crystal, as a function of time and compared to MD simulations with different parameters varied. These are, respectively: a) final lattice temperature b) energy absorption by the sample c) the damping coefficient and d) the thickness of the gold. In each case, the solid line represents the best-fit value.

The response of the gold foil was modelled by a classical molecular dynamics simulation using the LAMMPS package. To match the experimental results, the rate at which energy is transferred into the ions was varied, with the result of the two temperature model assumed to be an exponential function such that the rate of energy deposition decreases as $e^{-\tau}$ with $\tau = C_e/G$ and the electron heat capacity $C_e = T_e * 67.6 \times 10^5$ J m^{-3} K^{-2}. At each time step, the predicted diffraction line is found from the Fourier transform of the ion positions.

Within the observed variation in the lattice parameter, there are two regions of interest. Initially, the behaviour is controlled by the parameter of interest, G, as energy flows from the electrons into the ions and the lattice expands. Once this has ceased, however, the long-term mechanical response is related to the reverberation of the wave caused by the initial perturbation.

For this longer-term response, there are a variety of parameters that must be varied to give the best fit; these are

- The final lattice temperature, T_f
- The total energy per cubic nanometre absorbed by the sample, E_{in}
- The damping coefficient, γ, used to account for the energy loss to the mica substrate
- The thickness of the gold, l, which is assumed to be within ± 20 % of the quoted value of 200 nm

The results of fitting the observed data to each of these parameters is seen in Figure 5.7, and the best fit values are found to be $T_f = 320$ K, $E_{in} = 5.2$ eV/nm^3, $\gamma = 90$ ps and $l = 211$ nm. With these values now determined, we can return to the short-timescale behaviour and see the effect of varying the rate of energy deposition τ, as shown in Figure 5.8. This shows that the best fit occurs for $\tau = 5$ ps, corresponding to a coupling coefficient of $G = 2 \pm 1.2 \times 10^{16}$ W m^{-3} K^{-1}.

We can compare this to the result calculated from the metallic model, which we would expect to agree in this low-temperature, solid density regime. Indeed, we see that the predicted value is $G_0 = 2.8 \times 10^{16}$ W m^{-3} K^{-1}, in very good agreement with the results obtained. This also agrees with other experiments on gold in this regime, such as Hohlfeld *et al.* [76] and Ligges *et al.* [95], which also used optical excitation to heat the sample.

While it is clear, from these citations, that this work is not wholly novel, it does serve to illustrate two important points. First, that the metallic model can accurately

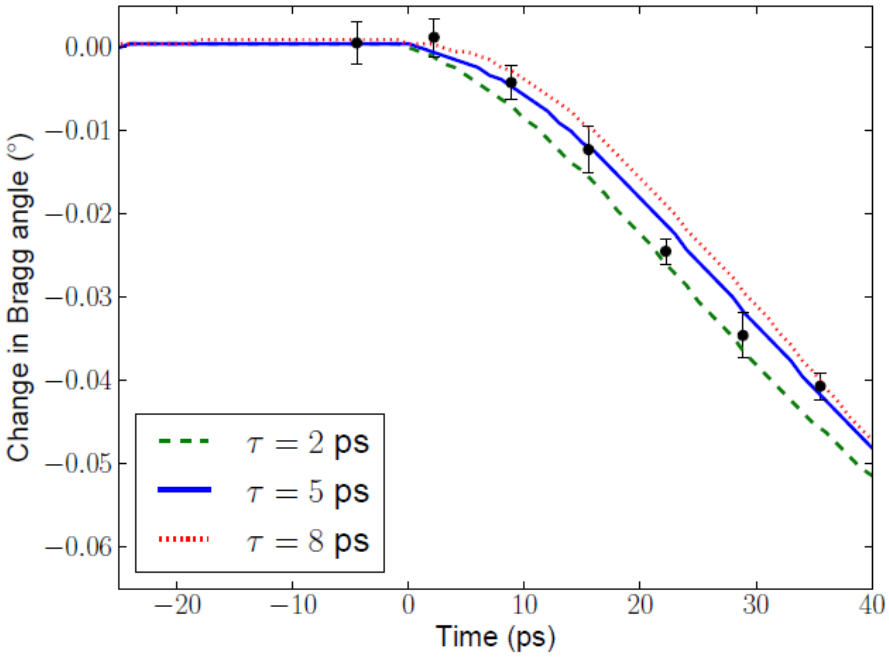

Figure 5.8: Results from MD fitted by varying the characteristic equilibration time for the electrons and ions, with the other values chosen as best fits from before (see Figure 5.7. The best fitting value of 5 ps corresponds to $G = 2.0 \pm 1.2 \times 10^{16}$ W m^{-3} K^{-1}.

describe electron-ion equilibration rates in room temperature materials. Secondly, it was an important proof-of-principle experiment for successfully carrying out an experiment on a much lower power laser system, and was the first published experimental results from our laboratory at Oxford.

5.2.4 Titan - August 2013

Having now obtained data from graphite with two different heating mechanisms, which both demonstrated significantly lower interspecies coupling in the high temperature limit of the material, an experimental campaign was planned to attempt to, first, reproduce the results in proton-heated graphite but with the temporal resolution that was possible on the experiment at GSI, and then to obtain similar data for diamond and metallic samples. Although we were successful in observing electron-ion coupling in a metallic sample, specifically tantalum, results from graphite and diamond proved harder to obtain. This was largely due to the inconsistency with which we could produce proton and x-ray sources for heating and probing the samples, and possible defects in the crystalline samples themselves.

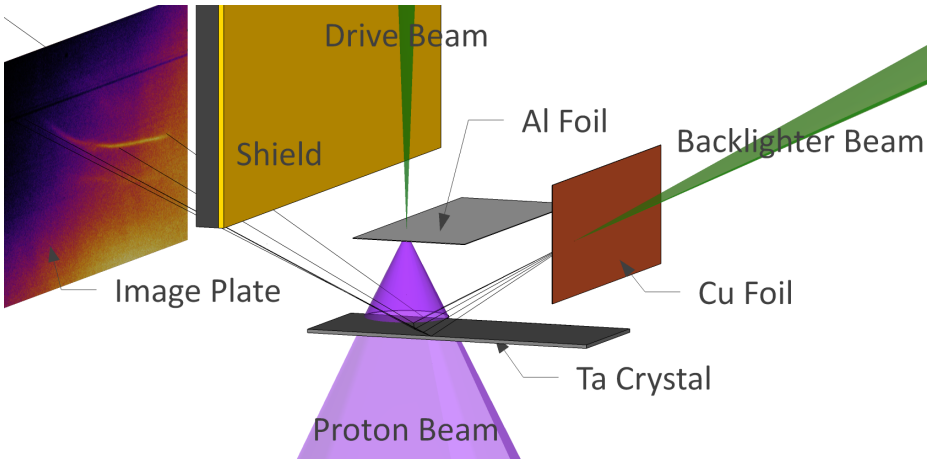

Figure 5.9: Schematic of experimental setup at Titan (August 2013). The incoming beam from above drives the proton beam (in purple) which heats the Ta sample. At a known delay, the backlighter beam strikes the Cu foil, driving the k-α transition and producing x-rays at 8.047 keV. These diffract from the sample and are detected on the image plate, with a Au-Pb shield to prevent direct illumination.

5.2.4.1 Experimental Setup

The setup was again similar to previous experiments, and is shown schematically in Figure 5.9. We split the Titan laser, operating at ~100 J in this experimental run and with a pulse length of 10 ps, in a pump-probe configuration. 40% is focused to a 50 μm spot on the Al foil, driving a proton beam through the TNSA mechanism. Half of this proton beam passed through a 30 μm polypropylene layer, removing low energy protons and giving more homogeneous heating through the sample, which was either 30 μm thick graphite or diamond, or 5 μm thick tantalum. The other half was detected on a stack of radiochromic film, which darkens in response to absorbed radiation dose. This allows an on-shot, energy-resolved image of the beam to be collected, as in [117], and used as the source term for the heating of the sample. An example of such data, in this case taken from a shot without a sample in place, is shown in Figure 5.10.

The RCF film is read out by scanning it with visible light through separate colour filters, which each respond differently to the same dose, with the relationship depending on both the type of film and the scanner used. For analysing this data, we used a scanner at the Rutherford Appleton Laboratory, calibrated with films irradiated by known doses. The results of this calibration are shown in Figure 5.11a. We can see that, at the doses relevant to this experiment, the red channel shows the highest sensitivity to incoming dose and consequently the fitting process took a greater weight

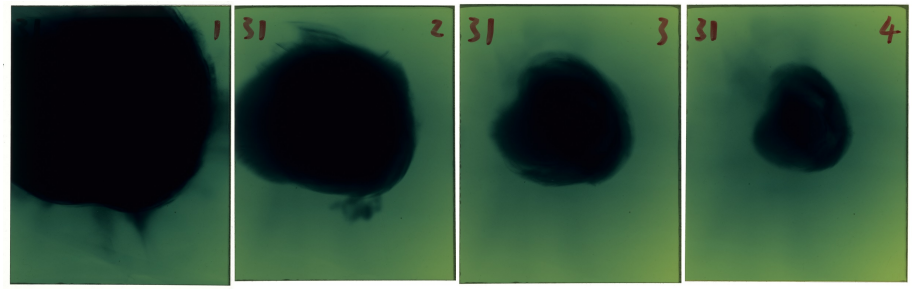

(a)

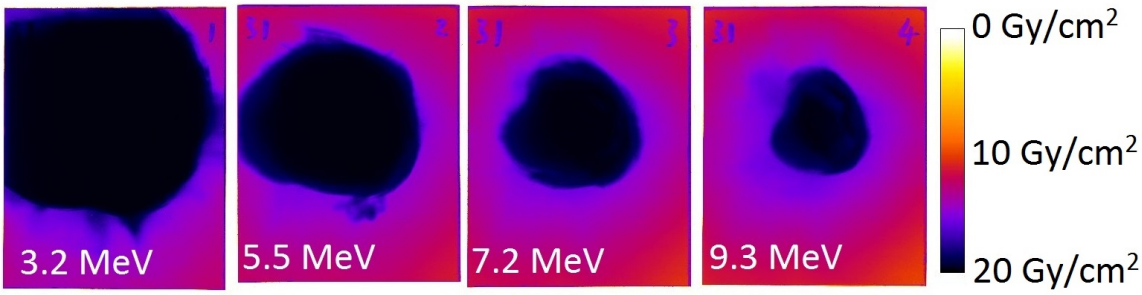

(b)

Figure 5.10: Raw image of radiochromic film after being exposed to raidation, and converted images with energies and areal dose at each layer. This data was taken without a sample in place in order to fully characterize the proton beam.

of these results.

This then allows us to convert the measured optical densities of the irradiated films shown in Figure 5.10a into an equivalent dose. The results of this conversion, from each of the colour channels separately, are shown in Figure 5.11b. Also shown is the dose from a best-fitted spectrum; this was found by taking the form of the spectrum from the fluid model used by Fuchs, Equation (5.3) above. The characteristic spectral temperature T_p and coefficient A were then varied, and for each spectrum the energy deposition into the stack modelled with known stopping powers in the different components of the RCF, taken from the SRIM database. This produced a dose in each layer, which could be compared to the doses observed in the real data. By minimizing the difference between the modelled and observed values, with the red channel more strongly weighted as outlined above, we obtained the best-fitting form of the spectrum, with $A = 6.4 \pm 0.8 \times 10^{14}$ and $T = 0.31 \pm 0.04$ MeV. The quoted error comes from comparison of the results from fitting to different colour channels.

With the proton spectrum now known, as well as the angular distribution also being measured from the RCF film data, the deposition of the energy in the sample can be modelled. As in the work from the previous Titan experiment, this used a

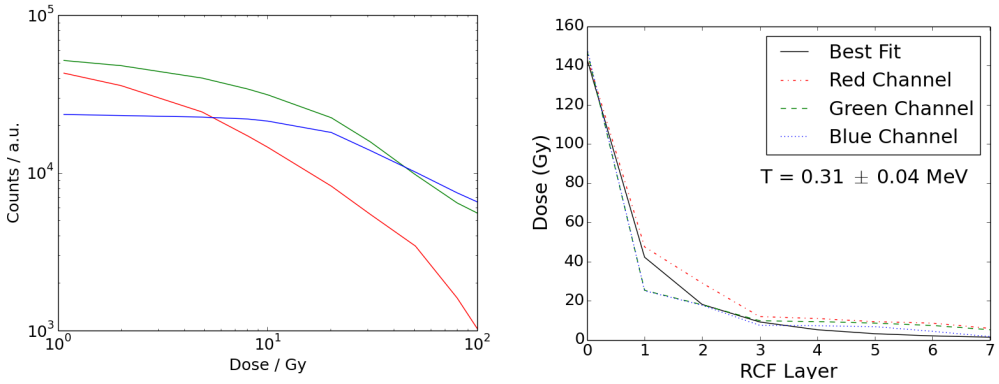

(a) (b)

Figure 5.11: a) Calibration data for the EBT2 film and scanner used
b) Observed dose on RCF, as measured by each colour channel, compared to dose calculated by varying A, T_{hot} in proton spectrum model Eq.(5.3), used with a ray-tracing simulation. Best fit with RCF data was found for $T_{hot} = 0.31 \pm 0.04$ MeV, $A = (6.4 \pm 0.8) \times 10^{14}$.

ray tracing simulation with known stopping powers of the protons in the materials. This gives the evolution of the energy in the electron subsystem as a function of time - effectively, the source term $S_R(t)$ in the two-temperature model - with the average heating rate being $\sim 2 \times 10^9$ W m^{-3} in tantalum, and around a factor of two lower in graphite and diamond due to the reduced stopping powers.

This can be converted into a temperature, as the heat capacity of the electrons can be calculated from the density of states (DOS), which is itself found from density functional theory calculations on a unit cell of tantalum with appropriate boundary conditions. The heat capacity is found from the DOS by

$$C_e(T_e) = \int_{-\infty}^{\infty} \frac{\partial f(\varepsilon, \mu, T_e)}{\partial T_e} g(\varepsilon) d\varepsilon \tag{5.21}$$

with $f(\varepsilon, \mu, T_e)$ the finite temperature Fermi distribution function and $g(\varepsilon)$ the DOS for the material. It is simple to see that, if $\int f \times g$ is the energy in the sample at a given temperature, $\frac{\partial(\int f \times g)}{\partial T_e}$ is the change in internal energy with temperature, which is the heat capacity, giving the relationship in (5.21). This gave a maximum electron temperature of $T_{max} \sim 4$ eV in tantalum.

While this proton heating occurred, the remaining energy from the Titan beam was focused onto a backlighter foil to a spot of around 30 μm, corresponding to an intensity of $\sim 6 \times 10^{16}$ W cm^{-2}. This drives the K-α transition - in this experiment, copper and zirconium backlighters were used, corresponding to x-ray energies of 8047 eV and 15775 eV, respectively. These diffracted off the heated target at a known

Figure 5.12: Examples of data taken from scanned image plates, with the scale giving the distance on the crystal sample.
a) Diffraction from tantalum crystal (002) plane, showing both K-α and K-β, with the difference in strength due to the source. The signal appearing to extend beyond the edge of the crystal is due to the finite X-ray source size.
b) Diffraction from a diamond sample in the (400) plane, taken without a proton source. The dark vertical line is due to a scanning error.

delay, and were observed using an image plate detector placed 200 mm away. The response of such image plates to X-rays, and their utility in experiments such as this, is discussed in [125].

As in the previous experiments at Titan and GSI, this diffracted line weakens in response to the increasing ion temperature, as energy is transferred from the electron subsystem into the ion phonon modes. We might also expect a change in the diffracted signal due to variation in the form factor F with increasing ionization, but calculations using a Thomas-Fermi equation of state model suggest that the change in average ionization is small, and consequently the change in the form factor is negligible.

Finally, using the DFT code ABINIT for the crystals probed in this experiment, and with appropriate band occupations and Fermi-Dirac smearing due to finite-temperature effects, we can see the effect on the Debye temperature Θ_D in the tantalum crystal. These results show changes in Θ_D of around 5% over the range of T_e probed. The effect of T_i as assumed to be negligible, as the Debye temperature characterises the potential 'well' around the ions; on the timescales considered the surrounding ions do not have time to move, and a tamper layer is used to prevent expansion, therefore the Debye temperature in the tantalum samples was considered to take a constant value of 225 K. Values in the other crystals were not considered, as we did not obtain diffraction data for analysis.

5.2.4.2 Results

Examples of the raw data from the scanned image plates with diffraction from tantalum (a) and diamond (b) targets are shown in Figure 5.12. The tantalum shot was at delay of 70 ps after the proton drive beam, whereas the diamond shot was taken without the pump (cold shot). Clear lines can be seen on both, with the curvature due to the geometry of the Bragg diffraction setup.

There are several things to note in comparing the data from the tantalum and diamond cases. Firstly, on shots with the protons also being driven, the noise on the image plate was significantly greater as any laser-matter interaction will produce

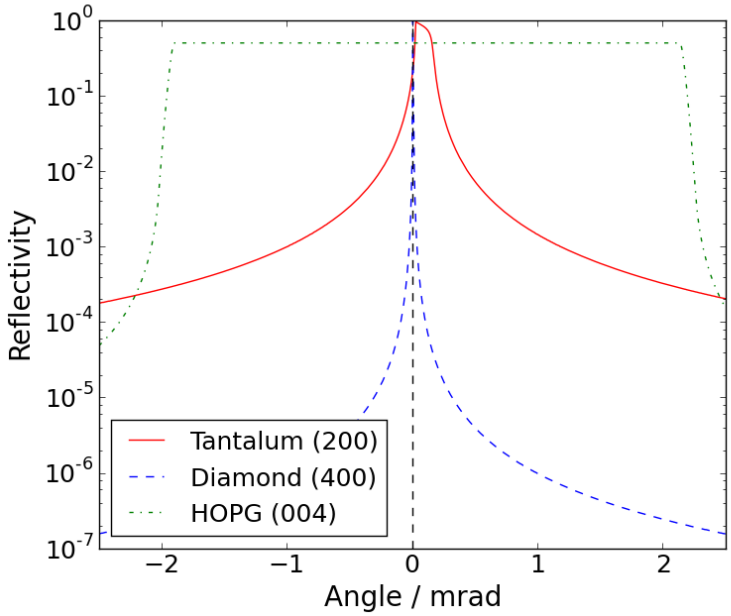

Figure 5.13: Theoretical diffraction profiles of tantalum, diamond and HOPG. Diamond has significantly lower values, and a narrower peak, than the single crystal tantalum. The wide HOPG peak assumes perfect mosaicity of 0.4° in the crystallites.

radiation of many different types. Although the TNSA process does drive a strong proton beam towards the sample target, x-rays and electrons are also emitted. Despite shielding being added to mitigate these effects, this needs to be balanced against still being able to observe the probe radiation. The diffraction orders are also significant, as the difference in reflectivity between the Ta (200) and diamond (400), the values of which can be seen in Figure 5.13, is very large, with the integrated reflectivity in tantalum around a factor of 100 larger. This also explains the difference in energy resolution on the image plates - while the tantalum produces very broad lines due to the shape of the reflectivity curve, in the case of diamond, with a very narrow peak, it is possible to distinguish the K-α_1 and K-α_2 peaks, due to the fine-structure splitting of the L-shell into $J = 1/2$ and $J = 3/2$ energy levels.

Finally, the conversion efficiency from laser energy to x-rays in the short pulse interactions used here to drive the probe beam also decreases with increasing photon energy - the empirical model of Green and Cosslet [63] suggests that the number of x-rays generated by an electron with energy E is:

$$N(E) = 4 \times 10^{-5}(E - E_0)^{1.63} \tag{5.22}$$

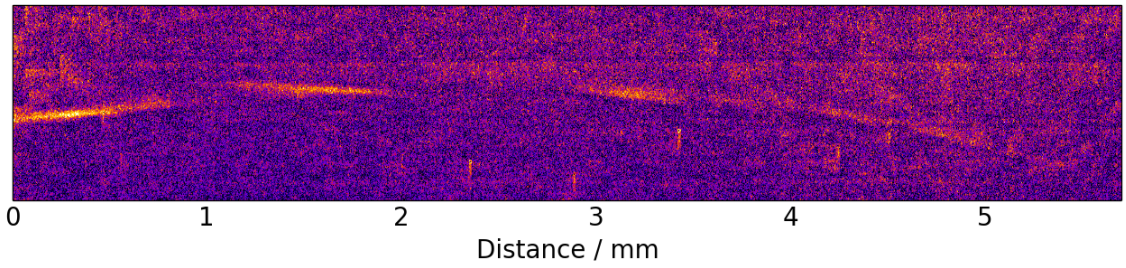

Figure 5.14: Diffraction of Cu K-α radiation from a graphite sample; the background has been subtracted to showthe signal more clearly and the scale is that of the crystal sample. Although the general shape of the Bragg line can be made out, with the curvature due to expected geometric effects, the breaking of the line, assumed to be due to misalinged crystallites, makes it unrealistic to observe weakening due to heating of the sample.

where E_0 is the K-shell ionization energy. With the ionization energies for Zr being twice that of Cu, the difference between the two materials will be significant except at temperatures well beyond those reached in this experiment.

We can consider how each of these effects explains what can be seen on the IPs shown in Figure 5.12. Despite the diamond data coming from a cold shot, it shows much lower contrast due to the weaker x-ray source and lower diffraction efficiency. Consequently, on shots with the protons being fired at the diamond sample, it was not possible to distinguish the diffracted line from the background signal on the IP, and therefore we did not obtain data for analysis from the diamond samples. The tantalum, on the other hand, is clearly visible, and in fact shows weakening towards the edge of the crystal beyond that due to the averaging over the source, and it was this data that was used for further analysis of the temperature evolution in the sample.

Before considering this further analysis, however, we will also note that we were not able to obtain data in the case of the graphite samples either. Unlike in diamond, there was visible diffraction on both cold and driven shots, which is expected due to the large integrated reflectivity found in highly oriented pyrolytic graphite (HOPG) samples. As can be seen in Figure 5.13, this is due to it exhibiting strong reflection over a broad range of angles.

However, this did not translate into observable weakening of the signal, due to poor crystal quality. Figure 5.14 shows an example of the diffraction pattern seen, and although the broad shape of a Bragg line is seen, with the curvature due to the

geometry of our setup, the line is broken several times. We would expect to see the signal weaken or even disappear near to the centre, where the protons are heating the crystal, but because of the line also disappearing at other points, it is not possible to confidently attribute the change in signal to the effect of lattice temperature.

Consequently, detailed analysis of the data obtained was only carried out for the tantalum samples. Even for these, the only data showing the temperature evolution was at a pump-probe delay of 70 ps, which is that shown in Figure 5.12. Data at 0ps delay showed no change in the diffracted signal from cold shots, although did still have a significant increase in noise due to the proton generation, and at 140ps there was no observable signal from the heated region, which we ascribe to the sample having entirely melted. From the lineout of the signal, we first account for geometric effects due to the variable source-detector distance, and for the filters placed in front of the image plate to reduce noise from other x-ray energies and charged particles.

To improve the signal to noise ratio on the image plate, we subtracted the averaged background on either side of the diffracted K-α line shown in Fig. 5.12. This was then further smoothed over a 30 μm length due to the finite size of the X-ray source. The signal was integrated across the width of the diffracted line, with different choices of the width giving only minor (<5%) corrections from the values shown in Fig. 5.14b). Imperfections in the crystal surface and inhomogeneities in the proton beam spectrum uniformity account for the spatial variation of the signal. From the deviation of the signal around a fitted curve, we estimate an overall error in this data of 11.8%.

This lineout is then normalized to the averaged signal from the unheated region because, as described in the section on the Debye-Waller effect, the approach used assesses relative diffractive strength rather than absolute values. For the Debye-Waller analysis, we are in the dynamic regime because the sample is a perfect crystal and multiples of the extinction length thick, such that any incoming beam will meet many layers at the correct Bragg angle. Consequently, the signal decreases much less than in the graphite cases in the previous experiments at GSI and Titan, with a maximum decrease of 33%, evaluated at the melt temperature of tantalum (3293 K) using Equation (5.19) and the factor e^{-M}. This temperature-dependant factor can be used for the observed decreases in intensity to obtain the temperature lineout at the delay of 70 ps, shown alongside the signal in Figure 5.15. The temperature is expected to decrease from a maximum to just above ambient temperature, and it can be seen that it does tend toward this value.

The ion temperature inferred from the decrease in Bragg diffraction intensity can also be compared to the results predicted by a two-temperature model by taking the

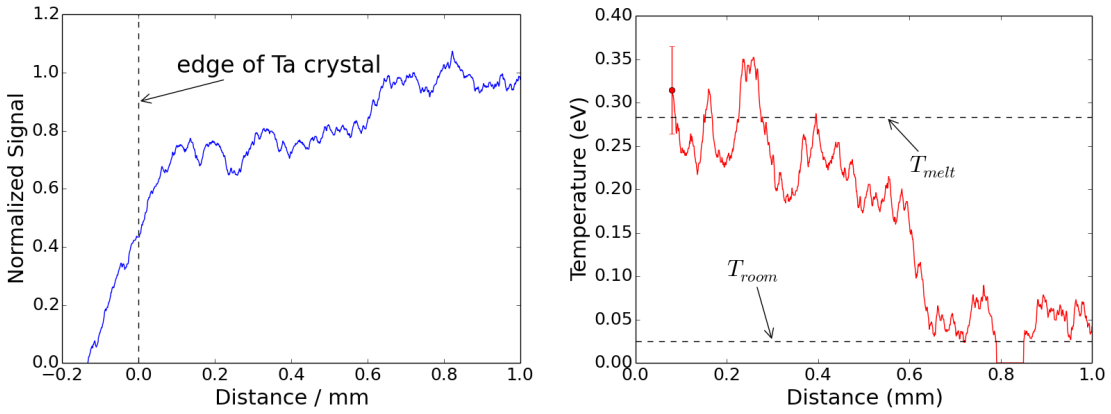

(a) (b)

Figure 5.15: a) Signal lineout, normalized to the unheated region at $r > 1$ mm. b) Equivalent temperatures calculated from the Debye-Waller factor e^{-M} under the assumption that the diffraction is fully dynamic. The error bar in the temperature graph is representative of the relevant errors for the temperature conversion, accounting for the Debye-Waller effect and uncertainty in the signal strength.

energy deposited into the electrons by the proton beam, along with values for the electron-ion coupling parameter taken from different models. The strength of the coupling predicted by the models at the temperatures reached in the experiment are are presented in Figure 5.16.

We can see from the results in Figure 5.17 that the values for the electron-ion coupling from both the metallic model and the Fermi Golden Rule imply temperatures which agree with the measured results to within the experimental error. The metallic model gives the value $G_0 = 3.08 \times 10^{17}$ W K^{-1} m^{-3}. Beyond the melt point, so at distances lower than ~ 0.3 mm, the sample is expected to have melted and so this diffractive diagnostic would not produce reliable results; instead, the apparent flattening off of the line could be due to the x-rays passing through the molten top layer and instead probing the still solid surface beneath.

The shape of the graph, with the rising temperature towards the centre of the spot, is due to proton time of flight (TOF) effects. The energy is deposited into the centre of the sample sooner than to the edges due to the greater path length to the spot edges. At the delay probed, the only protons to have reached the edges of the spot are the high-energy tail (>10 MeV) which do not deposit energy as efficiently as the low energy protons which have reached the centre, therefore the energy distribution across the spot is very inhomogeneous.

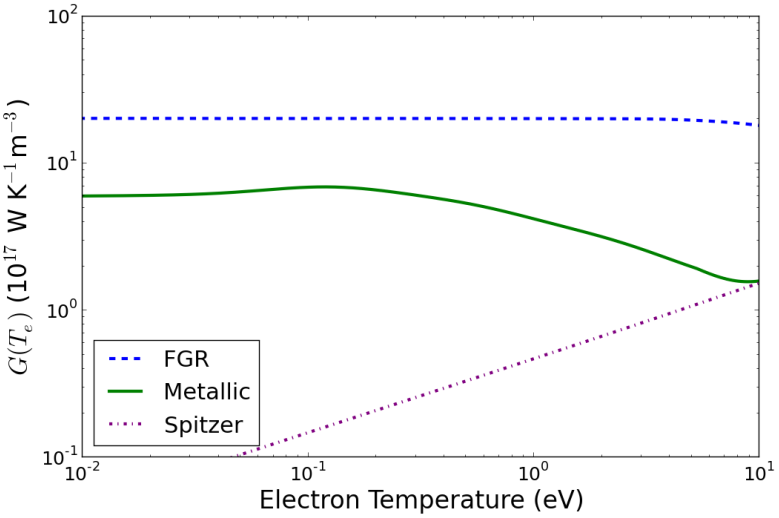

Figure 5.16: Values for the temperature-dependant coupling factor $G(T_e)$ in tantalum, over the temperature range relevant for the experiment as calculated by the quantum statistical Fermi Golden Rule approach (FGR), the metallic relaxation formalism and Spitzer's equation.

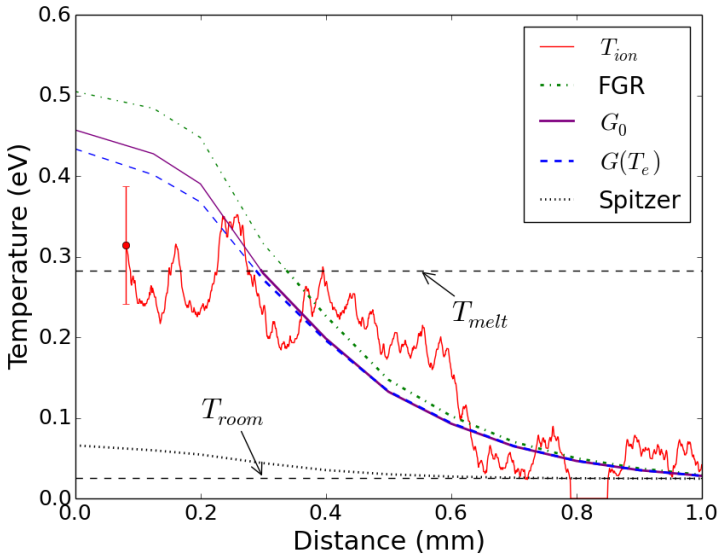

Figure 5.17: Ion temperature measured across the sample at a delay of 70 ps from proton creation, in red. Other lines show the expected temperatures from the measured proton spectrum and varying coupling models: Fermi Golden Rule (FGR), Spitzer, and the metallic formula with $\lambda = 0.65$ [102], with and without temperature dependence. Values above the melt temperature are calculated in the same way, neglecting the changes in C_e and $G(T_e)$ that would occur.

At lower coupling strengths, this effect would have little significance, as the timescale of the electron-ion energy transfer is 100s of ps, which is long compared to proton heating over $\sim$ 10 ps. In this case, however, the coupling timescale is sufficiently short, being on the order of picoseconds or even less, that it is comparable to the proton TOF and consequently the temperature evolution at a given point in the sample is dominated by the source term, rather than the coupling. Therefore the centre of the spot, having already experienced a greater proton flux, is at a much higher temperature than the edges of the spot because the energy is transferred from the heated electron to the ions so quickly.

Since the error bars on the data are large, care must be taken when drawing conclusions. We are confident in saying that the much lower coupling strengths predicted by Spitzer are incorrect, as the temperatures these predict in Figure 5.17 are well outside the error bars of data observed, which is very much expected given the solid density conditions probed. We are therefore confident in putting a lower limit on the coupling needed to explain the observed results. However, values from the metallic approach with higher values of λ made increasingly little difference and gave similarly good fits: at these coupling strengths, the electron and ion temperatures remain almost identical throughout the evolution, because the rate of energy deposition due to proton TOF is less than the coupling time.

5.3 Conclusions

From the theoretical results in the previous chapter, and the experimental results here, it is clear that the equilibration of electron and ion temperatures is a complex subject in WDM research. In Table I we have compiled a summary of our own, and other groups', experimental results. They show large differences in the equilibration rates and corresponding times, depending on the material probed and the heating mechanisms. The results we have obtained for the coupling strength in tantalum are high, although this is not unexpected from Eq. (4.9) as it has a high value of λ compared to other materials, as can be seen in Ref. [102].

As explained in detail in the appendix to Ref. [96], the metallic model assumes a high-temperature approximation to the Bose-Einstein distribution function, and would be significantly affected by changes to the density of states $g(E)$. The electron distribution changed from the assumed finite temperature Fermi distribution $f(E, T_e)$ would also make a difference [111], but only to the temperature-dependant part of Eq.

Sample	**Heating**	$\boldsymbol{\tau}$ **(ps)**	$\mathbf{G_0}$ $(\mathbf{WK^{-1}m^{-3}})$
Graphite	Protons	150	$5.4 - 6.6 \times 10^{15}$
Graphite	Electrons	450	2×10^{15}
Gold	Laser Irradiation	5	1.96×10^{16} (*)
Tantalum	Protons	<0.5	$> 3.08 \times 10^{17}$
Graphite [75]	X-rays	0.032 (*)	2.7×10^{19} (*)
Silicon [17]	Shock	200 (*)	1×10^{16}
Aluminium [135]	Shock	900 (*)	2.1×10^{15} (*)
Aluminium [133]	Laser Irradiation	< 1	3.1×10^{17} (*)
Gold [41]	Laser Irradiation	3.5 (*)	2.8×10^{16}

Table 5.2: Comparison of coupling strengths and corresponding characteristic equilibration times ($\tau = C_e/G_0$) from the work described, and previous work from other groups (in italics). Metals can be seen to generally couple more strongly, but drawing stronger conclusions is difficult.
(*) *Inferred from values given in the reference.*

(4.9). Although we are confident in these assumptions for our work here, situations where they are not applicable would require a different model.

Overall, the field is obviously still emerging, and experimental data is somewhat lacking. Although the work presented here contributes towards the necessary understanding of materials at these temperatures and densities, there are still many open questions to be resolved. The metallic model does seem, from our research, to be very good at describing materials both at the relatively low temperatures that it was originally envisged for, and at the high-temperature limit of the solid phase. Although some of the work on lower-Z materials - for instance the results from Riley [135] and Rethfeld [133] - shows that is it not universally applicable, it does appear to be one of the best options at the moment.

Although previous work has shown agreement between the quantum statistical approaches and results from MD simulations, there is a lack of experimental data from the warm dense regime due to the difficulty of probing electron and ion temperatures in such materials on these timescales. The diffractive techniques used here are no longer applicable, and there are few other methods to obtain temperatures at sufficient temporal resolution. Streaked optical pyrometery, such as that used in [43] or [110], could potentially give a measure of the electron temperature, but such techniques do not generally have a fast enough streak to resolve the electron cooling. In conclusion, progress in experimentally validating models for energy exchange in this regime looks to be gradual.

Chapter 6

Conclusions and Further Work

The work described in this thesis has considered, from a variety of perspectives, research into the behaviour of warm dense matter. This state, generally having temperatures in the range of eV and densities similar to those of solids, is characterised by having a coupling parameter on the order of unity, such that neither the interionic potential nor the ion kinetic energy dominates the behaviour of the system. Work on matter in this state is relevant in a variety of contexts, from studying states of matter and phase transitions inside astrophysical objects, to the evolution of DT capsules in ICF and heavy ions in nuclear fusion weapons.

In the first half of the thesis, the properties of structure factors in warm dense matter were considered from theoretical and experimental perspectives. Chapter 2 worked through the derivations of the static and dynamic structure factors of a sample. It then moved on to look at approaches to finding computational or modelled values for these quantities. Firstly, using molecular dynamics simulations with either a fixed potential (classical MD) or using density functional theory to better approximate physical systems, and then by describing the sample in liquid terms and using memory functions as an attempt to approximate the behaviour analytically.

This was continued in Chapter 3 with two experiments that aimed to experimentally measure structure factors in samples of warm dense aluminium. Both were carried out on the LCLS X-ray free electron laser, and consequently the chapter began with a description of the operation of such facilities. The first experiment measured the static structure factor at a wide range of angles, giving a well-resolved peak and estimates for the limiting value as $S(k \to 0)$, which allows the compressibility of the sample to be estimated. The experiment also included the use of spectrally resolved XRTS to estimate the plasma conditions, an increasingly important diagnostic for experiments on XFEL facilities.

The second experiment used a monochromator with the self-seeded beam, giving an exceptionally small bandwidth and allowing resolution of energy shifts due to ion acoustic waves in the sample. This was the first observation of such a phenomenon in a warm dense sample, and although the low photon flux gave significant errors in the data, the agreement between simulated values and experimental results was very encouraging. The presence of a central elastic peak, however, presents a challenge for explanation as it is not present in any of the predicted values. Although approaches can fit the data obtained, more experiments to see whether such a feature is reproduced, and work to look for alternative explanations, would be very productive in advancing the field and confirming the applicability of the models used.

The latter half of the thesis examined a very different question in the study of warm dense matter: that of the rate of energy exchange and temperature equilibration between the electrons and ions in recently-heated samples. In many studies of warm dense systems, a sample is heated using laser energy deposition, charged particle heating or shock heating. All of these methods deposit energy very inhomogeneously between the species, with direct laser irradiation and charged particles heating the electrons, and shocks heating the ions. Consequently, if an experiment using such a method probed the sample created before the species have been allowed to equilibrate, the results are unlikely to match those of an equilibrium system. Since many such experiments are aiming to reproduce the behaviour of the material in astrophysical objects, this would obviously be unphysical and lead to inaccurate conclusions.

Chapter 4 first looked at theoretical models for describing the rate of energy exchange, under the assumptions of the two temperature model; this requires that the individual species have well defined temperatures, and that the energy exchange can be contained within a single coupling term. The first model considers the primary source of energy exchange to be electron-phonon coupling, and derives an expression for the coupling parameter. Initially, this is restricted to low temperatures where scattering only occurs at the Fermi energy, and was then expanding to higher temperatures, but still in samples with an intact crystalline lattice. At the other extreme, the Spitzer model considers electron-ion collisions, with the initial assumption of an ideal gas or plasma, and an expression for the coupling was derived with this framework. Finally, a brief overview of methods considering collective oscillations with quantum statistical mechanics in a warm dense state was given, encompassing the Fermi golden rule approach and the full coupled mode theorem. Expressions for the coupling in these schemes were presented.

The final chapter dealt with experiments looking at measuring the rates of temperature equilibration in rapidly heated samples. To begin, some of the methods used were presented and explained, before moving on to the experiments themselves. The first measured the rate of equilibration in proton-heated graphite up to the melt point on the Titan laser at Livermore, California. This found an average value much below that predicted by the quantum statistical approaches, a result which was replicated in an experiment on the PHELIX laser in Darmstadt. The latter experiment used electron heating rather than proton, but found a result that agreed to within experimental error, given the different range of conditions probed. The lower coupling in graphite remains unexplained, although it does suggest that the models used may not be appropriate for graphite samples with an intact lattice.

The next experiment looked at gold, with direct laser irradiation causing heating of only a few kelvin. This probed the energy exchange by measuring the oscillation of the lattice constant in a perfect crystalline sample, deriving a value which agreed well with that predicted from the electron-phonon coupling model. The final experiment, which was led by the author, used proton heating on a variety of samples, but with the temperature equilibration rate only determined for single crystalline tantalum. This had a very high coupling constant, and although the results did agree with that of solid density metallic materials, they did not constrain it well.

What is clear from the work on temperature equilibration is that it is far from being fully understood. Consequently, experimentalists relying on models to determine the timescale needed between pump/probe should be aware that these are not necessarily trustworthy. Further experiments on samples, especially in the fully warm dense regime, and so beyond the melt point that was the limit in this work, would help constrain models and improve their reliability.

Appendix A

Thermostats in Molecular Dynamics

With particles in MD being defined solely by microscopic properties, the temperature is not an intrinsic property of the system, but can be extracted from the data at any given timestep by relation to the particles' instantaneous momenta

$$\sum_{i=1}^{N} \frac{|\mathbf{p}_i|^2}{2m_i} = \frac{k_B T}{2} (3N - N_c) \tag{A.1}$$

with N_c the number of constraints on the system, and so $3N - N_c = N_{df}$ the number of degrees of freedom.

An MD simulation will naturally remain in a microcanonical ensemble - also described as (NVE), it means that the number of particles, occupied volume and total particle energy will remain constant. This constraint is due to the physics of Newton's equations, in which all collisions are elastic and no energy can be gained or lost. However, in many situations this is not a good model for a physics system, which will, rather than behaving as an *isolated* system, behave as a *closed* one, in which energy can be exchanged with the surroundings, such that a constant temperature is maintained. This (NVT), or canonical, ensemble requires some form of thermostat to ensure that the system behaves as one at a constant temperature[80].

A.1 Velocity Rescaling

The simplest approach to this is by velocity scaling. If the velocities in a system are scaled by a factor χ then the consequent temperature change can be found by application of Eq. (A.1)

$$\begin{aligned}\Delta T &= \frac{1}{2}\sum_{i=1} 2\frac{m_i\left(\chi v_i\right)^2}{N_{df}k_B} - \frac{1}{2}\sum_{i=1} 2\frac{m_i v_i^2}{N_{df}k_B} \\ &= \left(\chi^2 - 1\right)T \end{aligned} \tag{A.2}$$

This then suggests that, if the temperature at a given timestep $T(t)$ is different from the inital temperature T_0, the required velocity scaling to correct for this change is

$$\chi = \sqrt{T_0/T(t)} \tag{A.3}$$

While this does, as required, maintain a constant temperature, it does not allow for the fluctuation in temperature which would naturally be present. One way to correct this is using the Berendsen thermostat. Rather than setting the temperature to that of the heat 'bath', this scales the change by the temperature difference between the bath and the system, giving a rate of change equal to

$$\frac{dT(t)}{dt} = \frac{1}{\tau}\left(T_0 - T(t)\right) \tag{A.4}$$

where τ determines the strength of the bath-system coupling, giving an exponential decay towards the desired temperature. Eqs. (A.2) and (A.3) therefore become

$$\Delta T = \frac{\delta t}{\tau}\left(T_0 - T(t)\right) \tag{A.5}$$

$$\chi^2 = 1 + \frac{\delta t}{\tau}\left[\frac{T_0}{T(t-\frac{\delta t}{2})} - 1\right] \tag{A.6}$$

This uses the leapfrog algorithm to evolve the temperatures, hence the presence of the $T(t-\frac{\delta t}{2})$, for evolving the system.

In the case that the coupling parameter $\tau = \delta t$ this reduces to the simple velocity scaling, and for $\tau \to \infty$ it becomes a microcanonical ensemble, with no velocity scaling occurring. Between these extremes, however, the parameter can be chosen empirically to alter the strength of the coupling and reproduce observed temperature fluctuations. It is worth noting that, while this thermostat can recreate physical behaviour, the ensemble it generates is definitively not canonical.

A.2 Nosé-Hoover Thermostat

Whil the previous method describes how a system relaxes to a target temperature, it is ineffective at probing the behaviour at equilibrium. The central concept of Nosé's work, which was then further developed by Hoover, is the introduction of an additional co-ordinate s, behaving as an imaginary extra particle in the system with a corresponding 'mass' Q, which acts as the necessary heat bath.

$$\begin{aligned}\mathscr{L}_0 &= \sum_{i=1}^{N} \frac{1}{2} m_i \dot{\mathbf{r}}_i^2 - V(\mathbf{r}^N) \\ \mathscr{L}_{ext} &= \sum_{i=1}^{N} \frac{1}{2} m_i \dot{s}^2 \dot{\mathbf{r}}_i^2 - V(\mathbf{r}^N) + \frac{Q}{2}\dot{s}^2 - \frac{g}{\beta}\ln s \end{aligned} \tag{A.7}$$

Taking the initial Lagrangian for the system $\mathscr{L}_0$ we can see that the addition of the extra coordinate results in the extended Lagrangian in Eq. (A.7). With $s = 1$ this easily reduces to the original form.

The momenta follow from $\mathscr{L}$ as

$$p = \frac{\partial \mathscr{L}(q, \dot{q})}{\partial \dot{q}} \tag{A.8}$$

$$\mathbf{p}_i = \frac{\partial \mathscr{L}_{ext}}{\partial \dot{\mathbf{r}}_i} = m_i s^2 \dot{\mathbf{r}}_i \tag{A.9}$$

$$p_s = \frac{\partial \mathscr{L}_{ext}}{\partial \dot{s}} = Q\dot{s} \tag{A.10}$$

with (A.8) the general definition in terms of arbitrary co-ordinate q, and the further equations the values for the relevant co-ordinates within this sytem. From the definitions of the momenta, we can construct the Hamiltonian for the extended system, containing as it does N particles, giving $6N$ degrees of freedom, and a further two from the co-ordinate s.

$$\mathscr{H} = \sum_i \dot{q}_i p_i - \mathscr{L} \tag{A.11}$$

$$\mathscr{H}_{ext} = \sum_{i=1}^{N} \frac{1}{2} \frac{\dot{\mathbf{p}}_i}{m_i s^2} + V(\mathbf{r}^N) + \frac{p_s^2}{2Q} + g\frac{\ln s}{\beta} \tag{A.12}$$

With the definition of the microncanonical partition function as

$$Z_{ext} = \frac{1}{N!}\int dp_s ds d\mathbf{p}^N d\mathbf{r}^N \delta(E - \mathscr{H}_{ext}) \tag{A.13}$$

and defining $\mathbf{p}' = \mathbf{p}/s$ this becomes:

$$Z_{ext} = \frac{1}{N!}\int dp_s ds d\mathbf{p}'^N d\mathbf{r}^N s^{3N} \times \delta\left[\sum_{i=1}^{N}\frac{1}{2}\frac{\mathbf{p}_i'^2}{m_i} + V(\mathbf{r}^N) + \frac{p_s^2}{2Q} + g\frac{\ln s}{\beta} - E\right] \tag{A.14}$$

$$= \frac{1}{N!}\int dp_s ds d\mathbf{p}'^N d\mathbf{r}^N s^{3N} \times \delta\left[\mathscr{H}(\mathbf{p}', \mathbf{r}) + \frac{p_s^2}{2Q} + g\frac{\ln s}{\beta} - E\right] \tag{A.15}$$

By treating the argument of the delta function as a function of s, $h(s)$, with a root at $s = s_0$, we can use the relationship

$$\delta\left[h(s)\right] = \frac{\delta(s - s_0)}{h'(s)} \tag{A.16}$$

In the case considered here

$$h(s) = \frac{g}{\beta}\ln s + \mathscr{H}(\mathbf{p}', \mathbf{r}) + \frac{p_s^2}{2Q} - E \tag{A.17}$$

$$\equiv \frac{g}{\beta}\ln s + X \tag{A.18}$$

where X has no direct s dependance. This gives a root at

$$s_0 = \exp\left[-\frac{\beta}{g}X\right] \tag{A.19}$$

which means that Eq. (A.16) becomes

$$\delta\left[h(s)\right] = \delta(s - s_0)\frac{\beta s}{g} \tag{A.20}$$

Returning to the partition function in Eq (A.13) we see that this can now be written as

$$Z_{ext} = \frac{1}{N!}\int dp_s ds d\mathbf{p}'^N d\mathbf{r}^N s^{3N} \quad \times \delta\left\{s - \exp\left[-\frac{\beta}{g}\left(\mathscr{H}(\mathbf{p}', \mathbf{r}) + \frac{p_s^2}{2Q} - E\right)\right]\right\} \tag{A.21}$$

$$= \frac{1}{N!}\frac{\beta}{g}\exp\left[\frac{\beta}{g}E(3N+1)\right] \quad \times \int dp_s \exp\left[-\frac{\beta}{g}\frac{p_s^2}{2Q}(3N+1)\right] \tag{A.22}$$

$$\times \int d\mathbf{p}'^N d\mathbf{r}'^N \exp\left[-\frac{\beta}{g}\mathscr{H}(\mathbf{p}', \mathbf{r})(3N+1)\right]$$

The second equation is obtained by integrating over the co-ordinate s. In the equation obatined, the integration over p_s is a Gaussian integration, which will take a constant value, leaving an extended ensemble equal to:

$$Z_{ext} = C\frac{1}{N!}\int d\mathbf{p}'^N d\mathbf{r}^N \exp\left[-\beta\mathscr{H}(\mathbf{p}',\mathbf{r})\frac{3N+1}{g}\right] \tag{A.23}$$

This ensemble is now suitable to be used in a simulation, with N particles and the additional parameter s.

A given quantity within the system, $A = A(\mathbf{p}',\mathbf{r})$, will then take an expectation value

$$\lim_{\tau\to\infty}\frac{1}{\tau}\int_0^\infty A[\mathbf{p}(t)/s(t),\mathbf{r}(t)]dt = \langle A[\mathbf{p}/s,\mathbf{r}]\rangle_{ext} \tag{A.24}$$

We have not used $\mathbf{p}'(t)$ because, as we will see, the value of the timesteps in the extended system is not necessarily constant. This ensemble average (within the defined microcanonical ensemble) is given by

$$\langle A[\mathbf{p}/s,\mathbf{r}]\rangle_{ext} = \frac{\int d\mathbf{p}'^N d\mathbf{r}^N A[\mathbf{p}',\mathbf{r}]\exp\left[-\beta\mathscr{H}(\mathbf{p}',\mathbf{r})\frac{3N+1}{g}\right]}{\int d\mathbf{p}'^N d\mathbf{r}^N \exp\left[-\beta\mathscr{H}(\mathbf{p}',\mathbf{r})\frac{3N+1}{g}\right]} \tag{A.25}$$

If we now choose to define the parameter $g = 3N+1$ this becomes

$$\langle A[\mathbf{p}/s,\mathbf{r}]\rangle_{ext} = \frac{\int d\mathbf{p}'^N d\mathbf{r}^N A[\mathbf{p}',\mathbf{r}]\exp\left[-\beta\mathscr{H}(\mathbf{p}',\mathbf{r})\right]}{\int d\mathbf{p}'^N d\mathbf{r}^N \exp\left[-\beta\mathscr{H}(\mathbf{p}',\mathbf{r})\right]} \tag{A.26}$$

We can see that this quantity, which is the average in the defined ensemble, is exactly equal to the canonical average of the quantity, in the phase space spanned by $\mathbf{p}'$ and $\mathbf{r}$. Conversely, if we had remained in the original microcanonical ensemble then this expectation value would be:

$$\langle A[\mathbf{p}/s,\mathbf{r}]\rangle_{ext} = \frac{\int d\mathbf{p}'^N d\mathbf{r}^N A[\mathbf{p}',\mathbf{r}]\,\delta\left[E-\mathscr{H}(\mathbf{p}',\mathbf{r})\right]}{\int d\mathbf{p}'^N d\mathbf{r}^N\,\delta\left[E-\mathscr{H}(\mathbf{p}',\mathbf{r})\right]} \tag{A.27}$$

From this, we see that carrying out a simulation with this newly defined ensemble will produce results which replicate those of a canonical system. If we return to look at the kinetic energy term in the Hamiltonian, we see that it has the form

$$\frac{1}{2}ms^2\dot{\mathbf{r}}^2 = \frac{\mathbf{p}'^2}{2m} = frac12m\dot{\mathbf{r}}'^2 \tag{A.28}$$

Therefore, the factor s can, rather being seen as an extra co-ordinate, instead be interpreted as a scaling to the timestep, such that the timestep used in the simulation will vary as s does.

To use this ensemble for an equation, we need to derive the equations of motion, both for the real and virtual variables. These can be derived in by standard methods from the definitions of the Hamiltonian and Lagrangian, giving results as follows:

$$\frac{d\mathbf{r}_i}{dt} = \frac{\partial \mathscr{H}_{ext}}{d\mathbf{p}_i} = \frac{\mathbf{p}_i}{m_i s^2} \tag{A.29a}$$

$$\frac{d\mathbf{p}_i}{dt} = -\frac{\partial \mathscr{H}_{ext}}{\partial \mathbf{r}_i} = -\frac{\partial V(\mathbf{r}^N)}{\partial \mathbf{r}_i} \tag{A.29b}$$

$$\frac{ds}{dt} = \frac{\partial \mathscr{H}_{ext}}{\partial \mathbf{r}_i} = \frac{p_s}{Q} \tag{A.29c}$$

$$\frac{dp_s}{dt} = -\frac{\partial \mathscr{H}_{ext}}{\partial s} = \frac{1}{s}\left[\sum_N^{i=1} \frac{\mathbf{p}_i^2}{m_i s^2} - \frac{g}{\beta}\right] \tag{A.29d}$$

With the simulation now proceeding in units of virtual time, corresponding to a varying amount of real time, new expressions are obtained for the time averages with no great complexity. Hoover insight to simplify the calculation was introduce the value $\xi = s' p'_s / Q$, giving expressions for the equations of motion with no explicit s dependance:

$$\dot{\mathbf{r}}'_i = \mathbf{p}'_i / m_i \tag{A.30a}$$

$$\dot{\mathbf{p}}'_i = -\frac{\partial V(\mathbf{r}'^N)}{d\mathbf{r}'_i} - \xi \mathbf{p}'_i \tag{A.30b}$$

$$\dot{\xi} = \frac{1}{Q}\left[\sum_N^{i=1} \frac{\mathbf{p}_i'^2}{m_i} - \frac{g}{\beta}\right] \tag{A.30c}$$

$$\frac{\dot{s}'}{s'} = \frac{d \ln s'}{dt'} = \xi \tag{A.30d}$$

A.3 Langevin Dynamics

Langevin dynamics use a stochastic approach, rather than the analytic equations above, to maintain a constant temperature. This is done by introducing additional force terms, one a friction term and the other a random force $\mathbf{R}$. Such a description can, for instance, reproduce the effects of a viscous solvent. The equation of motion for the particles in this model is:

$$\mathbf{F}_i - \gamma m_i \dot{\mathbf{r}}_i + \mathbf{R}_i(t) = m_i \ddot{\mathbf{r}}_i \tag{A.31}$$

$\mathbf{F}_i$ is the sum of forces from the other atoms, calculated as described in Chapter 2. The second term is the friction term, proportional to the aprticle velocity and controlled by the quantity γ. The random force, to account for the energy lost through the friction, is a Gaussian random force with mean 0 and variance $2\gamma m_i k_B T$.

Appendix B

Laser Driven Compression

As mentioned in the main text, HEDP samples can be created by driving a high-pressure shock wave in a sample with a long-pulse ($\sim$ ns) laser beam, for example on the National Ignition Facility[11]. If the incident laser beam has an intensity on or above the order of 10^9 W cm^{-2}, this will rapidly heat the sample, the outer layer of which expands to produce a plasma. This can either be done by directly heating and ablating the sample to be compressed [154], or by using a separate ablator layer[153], frequently consisting of a plastic, which then delivers the shock into the sample.

A shock is defined as a near-discontinuity in one or more thermodynamic variables in a flow. The behaviour of material across the shock front is governed by the Rankine-Hugoniot relations [130] [79]:

$$\rho_1 u_s = \rho_2 (u_s - u_2) \tag{B.1a}$$

$$p_2 - p_1 = \rho_2 u_2 (u_s - u_2) = \rho_1 u_s u_2 \tag{B.1b}$$

$$p_2 u_2 = \rho_1 u_s \left(\frac{u_2^2}{2} + E_2 - E_1 \right) \tag{B.1c}$$

In these equations, u_s is the shock speed, and the subscripts denote values upstream ($_1$) and downstream ($_2$) of the shock for the density, ρ, pressure, p, fluid particle velocity, u, and specific internal energies, E. The equations can be derived from conservation of mass, momentum and energy, respectively. The final equation requires the equation of state for the material, such that the internal energy can be expressed as a function of the other properties of the system. This is generally a non-trivial calculation, and some of the contributions to the energy must be approximated. Interestingly, this relationship also means that measurement of a shock can be used as a diagnostic for the EOS of a material, as in the work by Celliers *et al.* [18].

In general, however, determining the EOS of a material under shock compression is a significant challenge, and a large body of work exists studying precisely this problem through a variety of different methods - see for example [38] [43].

For a given material, and for defined values of the internal energy, there exists a one-to-one relationship between the density and temperature as implied by the Hugoniot relations [115]. This means that, for a shock compressed sample, a measurement of one value is enough to give a measure for the other, within experimental error. However, this also means that one a single 'line' of points of the $\rho - T$ phase space are accessible in shock compression experiments.

Other approaches to creating HEDP states include using ramp compression, where the pressure increases more gradually than in the shock case [152], albeit still on ns scales. This allows the material to be compressed quasi-isentropically, keeping the temperature much lower while still reaching high pressures and densities. In the other extreme, the methods outlined in the text, including direct laser irradiation and charged particle heating, allow creation of states with high temperatures without compression of the sample.

Appendix C

List of Publications

- N J Hartley, P Belancourt, D Chapman, T Döppner, R P Drake, D O Gericke, S H Glenzer, D Khaghani, S LePape, T Ma, P Neumayer, A Pak, L Peters, S Richardson, J Vorberger, T G White, G Gregori, Electron-Ion Temperature Equilibration in Warm Dense Tantalum, HEDP **14** (2015).

- T G White, P Mabey, D O Gericke, N J Hartley, H W Doyle, D McGonegle, DS Rackstraw, A Higginbotham, G Gregori, Electron-phonon equilibration in laser-heated gold films, Physical Review B **90** 1 014305(2014).

- T G White, N J Hartley, B Borm, B J B Crowley, J W O Harris, D C Hochhaus, T Kämpfer, K Li, P Neumayer, L K Pattison, F Pfeifer, S Richardson, A P L Robinson, I Uschmann, G Gregori, Electron-Ion Equilibration in Ultrafast Heated Graphite, Physical Review Letters **112** 14 145005 (2014).

- V Hilbert, C Rdel, G Brenner, T Döppner, S Düsterer, S Dziarzhytski, L Fletcher, E Frster, S H Glenzer, M Harmand, N J Hartley, L Kazak, D Komar, T Laarmann, H J Lee, T Ma, M Nakatsutsumi, A Przystawik, H Redlin, S Skruszewicz, P Sperling, J Tiggesbumker, S Toleikis and U Zastrau, Spatio-temporal coherence of free-electron laser radiation in the extreme ultraviolet determined by a Michelson interferometer, Applied Physics Letters **105** 101102 (2014).

- J Helfrich, D Kraus, A Ortnera, S Frydrycha, G Schaumanna, N J Hartley, G Gregori, B Kettle, D Riley, D C Carroll, M M Notley, C Spindloe and M Roth, Investigation of the solid-liquid phase transition of carbon at 150 GPa with spectrally resolved X-ray scattering, HEDP (accepted) (2015)

- D Kraus, J Vorberger, J Helfrich, D O Gericke, B Bachmann, V Bagnoud, B Barbrel, A Blažević, D C Carroll, W Cayzac, T. Döppner, L B Fletcher, A Frank, S Frydrych, E J Gamboa, M Gauthier, S Göde, E Granados, G Gregori, N J Hartley, B Kettle, H J Lee, B Nagler, P Neumayer, M M Notley, A Ortner, A Otten, A Ravasio, D Riley, F Roth, G Schaumann, D Schumacher, W Schumaker, K Siegenthaler, C Spindloe, F Wagner, K Wünsch, S H Glenzer, M Roth and R W Falcone, The complex ion structure of warm dense carbon measured by spectrally resolved x-ray scattering,

Bibliography

[1] P. B. Allen. Theory of thermal relaxation of electrons in metals. *Physical Review Letters*, 59(13):1460–1463, Sept. 1987.

[2] J. Amann, W. Berg, V. Blank, F.-J. Decker, Y. Ding, P. Emma, Y. Feng, J. Frisch, D. Fritz, J. Hastings, Z. Huang, J. Krzywinski, R. Lindberg, H. Loos, A. Lutman, H.-D. Nuhn, D. Ratner, J. Rzepiela, D. Shu, Y. Shvyd'ko, S. Spampinati, S. Stoupin, S. Terentyev, E. Trakhtenberg, D. Walz, J. Welch, J. Wu, A. Zholents, and D. Zhu. Demonstration of self-seeding in a hard-X-ray free-electron laser. *Nature Photonics*, 6(10):693–698, 2012.

[3] J. Andruszkow, B. Aune, V. Ayvazyan, N. Baboi, R. Bakker, V. Balakin, D. Barni, A. Bazhan, M. Bernard, A. Bosotti, J. C. Bourdon, W. Brefeld, R. Brinkmann, S. Buhler, J. P. Carneiro, M. Castellano, P. Castro, L. Catani, S. Chel, Y. Cho, S. Choroba, E. R. Colby, W. Decking, P. Den Hartog, M. Desmons, M. Dohlus, D. Edwards, H. T. Edwards, B. Faatz, J. Feldhaus, M. Ferrario, M. J. Fitch, K. Flöttmann, M. Fouaidy, A. Gamp, T. Garvey, C. Gerth, M. Geitz, E. Gluskin, V. Gretchko, U. Hahn, W. H. Hartung, D. Hubert, M. Hüning, R. Ischebek, M. Jablonka, J. M. Joly, M. Juillard, T. Junquera, P. Jurkiewicz, A. Kabel, J. Kahl, H. Kaiser, T. Kamps, V. V. Katelev, J. L. Kirchgessner, M. Körfer, L. Kravchuk, G. Kreps, J. Krzywinski, T. Lokajczyk, R. Lange, B. Leblond, M. Leenen, J. Lesrel, M. Liepe, A. Liero, T. Limberg, R. Lorenz, L. H. Hua, L. F. Hai, C. Magne, M. Maslov, G. Materlik, A. Matheisen, J. Menzel, P. Michelato, W. D. Möller, A. Mosnier, U. C. Müller, O. Napoly, A. Novokhatski, M. Omeich, H. S. Padamsee, C. Pagani, F. Peters, B. Petersen, P. Pierini, J. Pflüger, P. Piot, B. Phung Ngoc, L. Plucinski, D. Proch, K. Rehlich, S. Reiche, D. Reschke, I. Reyzl, J. Rosenzweig, J. Rossbach, S. Roth, E. L. Saldin, W. Sandner, Z. Sanok, H. Schlarb, G. Schmidt,

P. Schmüser, J. R. Schneider, E. A. Schneidmiller, H. J. Schreiber, S. Schreiber, P. Schütt, J. Sekutowicz, L. Serafini, D. Sertore, S. Setzer, S. Simrock, B. Sonntag, B. Sparr, F. Stephan, V. A. Sytchev, S. Tazzari, F. Tazzioli, M. Tigner, M. Timm, M. Tonutti, E. Trakhtenberg, R. Treusch, D. Trines, V. Verzilov, T. Vielitz, V. Vogel, G. V. Walter, R. Wanzenberg, T. Weiland, H. Weise, J. Weisend, M. Wendt, M. Werner, M. M. White, I. Will, S. Wolff, M. V. Yurkov, K. Zapfe, P. Zhogolev, and F. Zhou. First Observation of Self-Amplified Spontaneous Emission in a Free-Electron Laser at 109 nm Wavelength. *Physical Review Letters*, 85(18):3825–3829, 2000.

[4] S. I. Anisimov, B. L. Kapeliovich, and T. L. Perel'man. Electron emission from metal surfaces exposed to ultrashort laser pulses. *Sov. Phys.-JETP*, 39(2):375–377, 1975.

[5] T. Ao, Y. Ping, K. Widmann, D. Price, E. Lee, H. Tam, P. T. Springer, and A. Ng. Optical Properties in Nonequilibrium Phase Transitions. *Physical Review Letters*, 96(5):055001, Feb. 2006.

[6] U. Balucani, G. Ruocco, A. Torcini, and R. Vallauri. Fast sound in liquid water. *Physical Review E*, 47(3):1677–1684, Mar. 1993.

[7] G. Bannasch, J. Castro, P. McQuillen, T. Pohl, and T. C. Killian. Velocity relaxation in a strongly coupled plasma. *Physical Review Letters*, 109(18):185008, 2012.

[8] M. Baus and J. P. Hansen. Statistical mechanics of simple coulomb systems. *Physics Reports*, 59(1):1–94, 1980.

[9] F. N. Beg, A. R. Bell, A. E. Dangor, C. N. Danson, A. P. Fews, M. E. Glinsky, B. A. Hammel, P. Lee, P. A. Norreys, and M. Tatarakis. A study of picosecond laser-solid interactions up to 10(19) W cm(-2). *Physics of Plasmas*, 4(1997):447–457, 1997.

[10] E. Bevillon, J. P. Colombier, V. Recoules, and R. Stoian. Metal free electron properties under ultrafast laser-induced electron-phonon nonequilibrium: A first-principles study. *Physical Review B*, 89(11):115117, 2014.

[11] T. R. Boehly, V. N. Goncharov, W. Seka, M. A. Barrios, P. M. Celliers, D. G. Hicks, G. Collins, S. X. Hu, J. A. Marozas, and D. D. Meyerhofer. Velocity and Timing of Multiple Spherically Converging Shock Waves in Liquid Deuterium. *Physical Review Letters*, 106(19):195005, May 2011.

[12] M. Borghesi, J. Fuchs, S. V. Bulvanoc, A. J. MacKinnon, P. K. Patel, and M. Roth. Fast Ion Generation by High-Intensity Laser Irradiation of Solid Targets and Applications. *Fusion Science and Technology*, 49(3):412–439, 2006.

[13] R. Bredow, T. Bornath, W.-D. Kraeft, M. W. C. Dharma-Wardana, and R. Redmer. Classical-Map Hypernetted Chain Calculations for Dense Plasmas. *Contributions to Plasma Physics*, 55(2):222–229, 2015.

[14] J.-L. Bretonnet and A. Derouiche. Analytic form for the one-component plasma structure factor. *Physical Review B*, 38(13):9255–9256, 1988.

[15] H. Brysk. Electron-Ion equilibration in a Partially Degenerate Plasma. *Plasma Physics*, 16:927–932, 1974.

[16] A. Calisti, S. Ferri, M. Marciante, and B. Talin. Warm dense matter through classical molecular dynamics. *High Energy Density Physics*, 13:1–8, July 2014.

[17] P. Celliers, A. Ng, G. Xu, and A. Forsman. Thermal equilibration in a shock wave. *Physical Review Letters*, 68(15):2305–2308, Apr. 1992.

[18] P. M. Celliers, G. Collins, D. K. Bradley, S. J. Moon, D. H. Munro, R. Cauble, D. M. Gold, L. B. Da Silva, F. A. Weber, R. J. Wallace, B. A. Hammel, and W. W. Hsing. VISAR for measuring equation of state and shock propagation in liquid deuterium (abstract). *Review of Scientific Instruments*, 72(1):1038, 2001.

[19] D. A. Chapman and D. O. Gericke. Analysis of Thomson scattering from nonequilibrium plasmas. *Physical Review Letters*, 107(16):165004, 2011.

[20] D. A. Chapman, D. Kraus, A. L. Kritcher, B. L. Bachmann, G. Collins, R. W. Falcone, J. A. Gaffney, D. Gericke, S. H. Glenzer, T. M. Guymer, J. A. Hawreliak, O. L. Landen, S. Le Pape, T. Ma, P. Neumayer, J. Nilsen, A. Pak, R. Redmer, D. C. Swift, J. Vorberger, and T. Döppner. Simulating x-ray Thomson scattering signals from high-density, millimetre-scale plasmas at the National Ignition Facility. *Physics of Plasmas*, 21(8):082709, Aug. 2014.

[21] D. A. Chapman, J. Vorberger, and D. Gericke. Reduced coupled-mode approach to electron-ion energy relaxation. *Physical Review E*, 88(1):013102, July 2013.

[22] D. K. Chaturvedi, M. Rovere, G. Senatore, and M. P. Tosi. Liquid alkali metals and alloys as electron-ion plasmas. *Physica 111B*, 111(1):11–23, 1981.

[23] Z. Chen, B. Holst, S. Kirkwood, V. Sametoglu, M. Reid, Y. Y. Tsui, V. Recoules, and A. Ng. Evolution of ac Conductivity in Nonequilibrium Warm Dense Gold. *Physical Review Letters*, 110(13):135001, Mar. 2013.

[24] Z. Chen, V. Sametoglu, Y. Y. Tsui, T. Ao, and A. Ng. Flux-Limited Nonequilibrium Electron Energy Transport in Warm Dense Gold. *Physical Review Letters*, 108(16):165001, Apr. 2012.

[25] J. Chihara. Interaction of photons with plasmas and liquid metals - photoabsorption and scattering. *Journal of Physics: Condensed Matter*, 12(3):231–247, Jan. 2000.

[26] O. Ciricosta, S. M. Vinko, H.-K. Chung, B. I. Cho, C. R. D. Brown, T. Burian, J. Chalupský, K. Engelhorn, R. W. Falcone, C. Graves, V. Hájková, A. Higginbotham, L. Juha, J. Krzywinski, H. J. Lee, M. Messerschmidt, C. D. Murphy, Y. Ping, D. S. Rackstraw, A. Scherz, W. Schlotter, S. Toleikis, J. J. Turner, L. Vysin, T. Wang, B. Wu, U. Zastrau, D. Zhu, R. W. Lee, P. Heimann, B. Nagler, and J. S. Wark. Direct measurements of the ionization potential depression in a dense plasma. *Physical Review Letters*, 109(6):065002, 2012.

[27] R. S. Cohen, L. Spitzer, and P. McRoutly. The Electrical Conductivity of an Ionized Gas. *Physical Review*, 80(2):640–644, 1950.

[28] J. E. Cross, B. Reville, and G. Gregori. Scaling of Magneto-Quantum-Radiative Hydrodynamic Equations: From Laser-Produced Plasmas To Astrophysics. *The Astrophysical Journal*, 795(59), 2014.

[29] J. Daligault and G. Dimonte. Correlation effects on the temperature-relaxation rates in dense plasmas. *Physical Review E*, 79(5):–564–3, 2009.

[30] C. G. Darwin. XXXIV: The Theory of X-Ray Reflexion. *The London, Edinburgh, and Dublin Philosophical Magazine and Journal of Science*, 27(158):315–333, 1914.

[31] J. M. Dawson. Particle simulation of plasmas. *Reviews of Modern Physics*, 55(2):403–447, Apr. 1983.

[32] M. W. C. Dharma-Wardana. Electron-ion and ion-ion potentials for modeling warm dense matter: Applications to laser-heated or shock-compressed Al and Si. *Physical Review E*, 86(3):036407, Sept. 2012.

[33] M. W. C. Dharma-Wardana and F. Perrot. Energy relaxation and the quasiequation of state of a dense two-temperature nonequilibrium plasma. *Physical Review E*, 58(3):3705–3718, Sept. 1998.

[34] P. A. M. Dirac. The Quantum Theory of the Emission and Absoprtion of Radiation. *Proceedings of the Royal Society of London A: Mathematical, Physical and Engineering Sciences*, 114(767), 1927.

[35] Z. Donkó and P. Hartmann. Thermal conductivity of strongly coupled Yukawa liquids. *Physical Review E*, 69(1):016405, 2004.

[36] T. Döppner, A. L. Kritcher, D. Kraus, S. H. Glenzer, B. L. Bachmann, D. A. Chapman, G. Collins, R. W. Falcone, J. Hawreliak, O. L. Landen, H. J. Lee, S. LePape, T. Ma, P. Neumayer, R. Redmer, and D. C. Swift. X-ray Thomson scattering as a temperature probe for Gbar shock experiments. *Journal of Physics: Conference Series*, 500:192019, 2014.

[37] R. P. Drake. *High-Energy-Density Physics*. Springer-Verlag, Berlin, 2006.

[38] G. Dyer, A. Bernstein, B. Cho, J. Osterholz, W. Grigsby, A. Dalton, R. Shepherd, Y. Ping, H. Chen, K. Widmann, and T. Ditmire. Equation-of-State Measurement of Dense Plasmas Heated With Fast Protons. *Physical Review Letters*, 101(1):015002, July 2008.

[39] F. R. Elder, A. M. Gurewitsch, and R. V. Langmuir. Radiation from Electrons in a Synchotron. *Physical Review*, 71(11):829–830, 1947.

[40] H. Elsayed-Ali, T. Norris, M. Pessot, and G. Mourou. Time-resolved observation of electron-phonon relaxation in copper. *Physical Review Letters*, 58(12):1212–1215, Mar. 1987.

[41] R. Ernstorfer, M. Harb, C. T. Hebeisen, G. Sciaini, T. Dartigalongue, and R. J. D. Miller. The formation of warm dense matter: experimental evidence for electronic bond hardening in gold. *Science*, 323(5917):1033–7, Feb. 2009.

[42] D. E. Evans and J. Katzenstein. Laser light scattering in laboratory plasmas. *Reports on Progress in Physics*, 32:207–271, 1969.

[43] K. Falk, E. Gamboa, G. Kagan, D. Montgomery, B. Srinivasan, and J. Benage. Equation of State Measurements of Warm Dense Carbon Using Laser-Driven Shock and Release Technique. *Physical Review Letters*, 112(15):155003, Apr. 2014.

[44] Y. Feng, J. Goree, and B. Liu. Longitudinal viscosity of two-dimensional Yukawa liquids. *Physical Review E*, 87(1):013106, 2013.

[45] A. P. Fews, P. A. Norreys, F. N. Beg, A. R. Bell, A. E. Dangor, C. N. Danson, P. Lee, and S. Rose. Plasma Ion Emission from High Intensity Picosecond Laser Pulse Interactions with Solid Targest. *Physical Review Letters*, 73(13):1801–1805, 1994.

[46] L. Fletcher, H. J. Lee, B. Barbrel, M. Gauthier, E. Galtier, B. Nagler, T. Döppner, S. LePape, T. Ma, A. Pak, D. Turnbull, T. G. White, G. Gregori, M. Wei, R. W. Falcone, P. Heimann, U. Zastrau, J. B. Hastings, and S. H. Glenzer. Exploring Mbar shock conditions and isochorically heated aluminum at the Matter in Extreme Conditions end station of the Linac Coherent Light Source. *Review of Scientific Instruments*, 85(11):11E702, Nov. 2014.

[47] L. B. Fletcher, E. Galtier, P. Heimann, H. J. Lee, B. Nagler, J. Welch, U. Zastrau, J. B. Hastings, and S. H. Glenzer. Plasmon measurements with a seeded x-ray laser. *Journal of Instrumentation*, 8(11):C11014, 2013.

[48] L. B. Fletcher, A. L. Kritcher, A. Pak, T. Ma, T. Döppner, C. Fortmann, L. Divol, O. S. Jones, O. L. Landen, H. A. Scott, J. Vorberger, D. A. Chapman, D. O. Gericke, B. A. Mattern, G. T. Seidler, G. Gregori, R. W. Falcone, and S. H. Glenzer. Observations of Continuum Depression in Warm Dense Matter with X-Ray Thomson Scattering. *Physical Review Letters*, 112(14):145004, Apr. 2014.

[49] L. B. Fletcher, H. J. Lee, T. Döppner, E. Galtier, B. Nagler, P. Heimann, C. Fortmann, S. LePape, T. Ma, M. Millot, A. Pak, D. Turnbull, D. A. Chapman, D. O. Gericke, J. Vorberger, T. G. White, G. Gregori, M. Wei, B. Barbrel, R. W. Falcone, C. Kao, H. Nuhn, J. Welch, U. Zastrau, P. Neumayer, J. B. Hastings, and S. H. Glenzer. Ultrabright X-ray laser scattering for dynamic warm dense matter physics. *Nature Photonics*, 9(4):274–279, 2015.

[50] C. Fortmann, T. Bornath, R. Redmer, H. Reinholz, G. Röpke, V. Schwarz, and R. Thiele. X-ray Thomson scattering cross-section in strongly correlated plasmas. *Laser and Particle Beams*, 27:311–319, 2009.

[51] J. M. Foster, B. H. Wilde, P. A. Rosen, R. J. R. Williams, B. E. Blue, R. F. Coker, R. P. Crake, A. Frank, P. A. Keiter, A. M. Khokhlov, J. P. Knauer, and T. S. Perry. High-Energy-Density Laboratory Astrophysics Studies of Jets and Bow Shocks. *The Astrophysical Journal Letters*, 634(1):L77, 2005.

[52] J. Fuchs, P. Antici, E. DHumières, E. Lefebvre, M. Borghesi, E. Brambrink, C. A. Cecchetti, M. Kaluza, V. Malka, M. Manclossi, S. Meyroneinc, P. Mora, J. Schreiber, T. Toncian, H. Pépin, and P. Audebert. Laser-driven proton scaling laws and new paths towards energy increase. *Nature Physics*, 2(1):48–54, Dec. 2005.

[53] J. Fujimoto, J. Liu, E. Ippen, and N. Bloembergen. Femtosecond Laser Interaction with Metallic Tungsten and Nonequilibrium Electron and Lattice Temperatures. *Physical Review Letters*, 53(19):1837–1840, Nov. 1984.

[54] S. Galam and J. P. Hansen. Statistical mechanics of dense ionized matter VI. *Physical Review A*, 14(2):816–832, 1976.

[55] S. Galambosi. *Electronic Excitations in Solids Studied using Inelastic X-ray Scattering*. PhD thesis, University of Helsinki, 2007.

[56] E. García Saiz, G. Gregori, D. Gericke, J. Vorberger, B. Barbrel, R. J. Clarke, R. R. Freeman, S. H. Glenzer, F. Y. Khattak, M. Koenig, O. L. Landen, D. Neely, P. Neumayer, M. M. Notley, A. Pelka, D. Price, M. Roth, M. Schollmeier, C. Spindloe, R. L. Weber, L. van Woerkom, K. Wünsch, and D. Riley. Probing warm dense lithium by inelastic X-ray scattering. *Nature Physics*, 4(12):940–944, Oct. 2008.

[57] D. O. Gericke, M. S. Murillo, and M. Schlanges. Dense plasma temperature equilibration in the binary collision approximation. *Physical Review E*, 65(3):036418, 2002.

[58] S. H. Glenzer, G. Gregori, F. J. Rogers, J. M. Foster, S. W. Pollaine, R. S. Wallace, and O. L. Landen. X-ray scattering from solid density plasmas. *Physics of Plasmas*, 10(6):2433, 2003.

[59] S. H. Glenzer, O. L. Landen, P. Neumayer, R. W. Lee, K. Widmann, S. W. Pollaine, R. J. Wallace, G. Gregori, A. Höll, T. Bornath, R. Thiele, V. Schwarz, W.-D. Kraeft, and R. Redmer. Observations of plasmons in warm dense matter. *Physical Review Letters*, 98(6):065002, 2007.

[60] S. H. Glenzer, P. Neumayer, T. Döppner, O. L. Landen, R. W. Lee, R. J. Wallace, S. Weber, H. J. Lee, A. L. Kritcher, R. W. Falcone, S. P. Regan, H. Sawada, D. D. Meyerhofer, G. Gregori, C. Fortmann, V. Schwarz, and R. Redmer. Compton scattering measurements from dense plasmas. *Journal of Physics: Conference Series*, 112:032071, 2008.

[61] S. H. Glenzer and R. Redmer. X-ray Thomson scattering in high energy density plasmas. *Reviews of Modern Physics*, 81(4):1625–1663, Dec. 2009.

[62] X. Gonze, B. Amadon, P.-M. Anglade, J.-M. Beuken, F. Bottin, P. Boulanger, F. Bruneval, D. Caliste, R. Caracas, M. Côté, T. Deutsch, L. Genovese, P. Ghosez, M. Giantomassi, S. Goedecker, D. R. Hamann, P. Hermet, F. Jollet, G. Jomard, S. Leroux, M. Mancini, S. Mazevet, M. J. T. Oliveira, G. Onida, Y. Pouillon, T. Rangel, G.-M. Rignanese, D. Sangalli, R. Shaltaf, M. Torrent, M. J. Verstraete, G. Zerah, and J. W. Zwanziger. ABINIT: First-principles approach to material and nanosystem properties. *Computer Physics Communications*, 180(12):2582–2615, Dec. 2009.

[63] M. Green and V. E. Cosslett. Measurements of K , L and M shell x-ray production efficiencies. *British Journal of Applied Physics*, 1(2):425–436, 1968.

[64] G. Gregori and D. O. Gericke. Low frequency structural dynamics of warm dense matter. *Physics of Plasmas*, 16(5):056306, 2009.

[65] G. Gregori, S. H. Glenzer, W. Rozmus, R. W. Lee, and O. L. Landen. Theoretical model of x-ray scattering as a dense matter probe. *Physical Review E*, 67(2):026412, Feb. 2003.

[66] G. Gregori, U. Kortshagen, J. Heberlein, and E. Pfender. Analysis of Thomson scattered light from an arc plasma jet. *Physical Review E*, 65(4):046411, Apr. 2002.

[67] G. Gregori, A. Ravasio, A. Höll, S. H. Glenzer, and S. Rose. Derivation of the static structure factor in strongly coupled non-equilibrium plasmas for X-ray scattering studies. *High Energy Density Physics*, 3(1-2):99–108, May 2007.

[68] J. P. Hansen. Statistical Mechanics of Dense Ionized Matter I. *Physical Review A*, 8(6):3096–3109, 1973.

[69] J. P. Hansen and I. R. McDonald. *Theory of Simple Liquids*. Academic Press, London, 2nd edition, 1986.

[70] J. P. Hansen, I. R. McDonald, and E. L. Pollock. Statistical mechanics of dense ionized matter III. *Physical Review A*, 11(3):1025–1039, 1975.

[71] L. E. Hargrove, R. L. Fork, and M. A. Pollack. Locking of He-Ne laser modes induced by synchronous intracavity modulation. *Applied Physics Letters*, 5(1):4–5, 1964.

[72] N. M. Harrison. *An Introduction to Density Functional Theory*. NATO Science Series III Computer and Science Systems, 2003.

[73] N. J. Hartley, P. Belancourt, D. A. Chapman, T. Doeppner, R. P. Drake, D. O. Gericke, S. H. Glenzer, D. Khaghani, S. LePape, T. Ma, P. Neumayer, A. Pak, L. Peter, S. Richardson, J. Vorberger, T. G. White, and G. Gregori. Electron-Ion Temperature Equilibration in Warm Dense Tantalum. *High Energy Density Physics*, 14:1–5, 2015.

[74] S. P. Hatchett, C. G. Brown, T. E. Cowan, E. A. Henry, J. S. Johnson, M. H. Key, J. A. Koch, A. B. Langdon, B. F. Lasinski, R. W. Lee, A. J. Mackinnon, D. M. Pennington, M. D. Perry, T. W. Phillips, M. Roth, T. C. Sangster, M. S. Singh, R. A. Snavely, M. A. Stoyer, S. C. Wilks, and K. Yasuike. Electron, photon, and ion beams from the relativistic interaction of Petawatt laser pulses with solid targets. *Physics of Plasmas*, 7(5):2076, 2000.

[75] S. Hau-Riege, A. Graf, T. Döppner, R. London, J. Krzywinski, C. Fortmann, S. H. Glenzer, M. Frank, K. Sokolowski-Tinten, M. Messerschmidt, C. Bostedt, S. Schorb, J. Bradley, A. Lutman, D. Rolles, A. Rudenko, and B. Rudek. Ultrafast Transitions from Solid to Liquid and Plasma States of Graphite Induced by X-Ray Free-Electron Laser Pulses. *Physical Review Letters*, 108(21):217402, May 2012.

[76] J. Hohlfeld, S.-S. Wellershoff, J. Güdde, U. Conrad, V. Jähnke, and E. Matthias. Electron and lattice dynamics following optical excitation of metals. *Chemical Physics*, 251:237–258, 2000.

[77] A. Höll, T. Bornath, L. Cao, T. Döppner, S. Düsterer, E. Förster, C. Fortmann, S. H. Glenzer, G. Gregori, T. Laarmann, K. H. Meiwes-Broer, A. Przystawik, P. Radcliffe, R. Redmer, H. Reinholz, G. Röpke, R. Thiele, J. Tiggesbäumker, S. Toleikis, N. X. Truong, T. Tschentscher, I. Uschmann, and U. Zastrau. Thomson scattering from near-solid density plasmas using soft X-ray free electron lasers. *High Energy Density Physics*, 3:120–130, 2007.

[78] B. Holst, V. Recoules, S. Mazevet, M. Torrent, A. Ng, Z. Chen, S. E. Kirkwood, V. Sametoglu, M. Reid, and Y. Y. Tsui. ¡i¿Ab initio¡/i¿ model of optical properties of two-temperature warm dense matter. *Physical Review B*, 90(3):035121, July 2014.

[79] H. Hugoniot. Memoire sur la propagation du mouvement dans un fluide indefini. *Journal de mathematquies pures et appliquees*, 4(4):153–168, 1888.

[80] P. H. Hünenberger. Thermostat Algorithms for Molecular Dynamics Simulations. *Advanced Computer Simulation*, Spring-Berlin-Heidelberg:105–149, 2005.

[81] O. A. Hurricane, D. A. Callahan, D. T. Casey, P. M. Celliers, C. Cerjan, E. L. Dewald, T. R. Dittrich, T. Döppner, D. E. Hinkel, L. F. Berzak Hopkins, J. L. Kline, S. Le Pape, T. Ma, A. G. MacPhee, J. L. Milovich, A. Pak, H.-S. Park, P. K. Patel, B. A. Remington, J. D. Salmonson, P. T. Springer, and R. Tommasini. Fuel gain exceeding unity in an inertially confined fusion implosion. *Nature*, 506(7488):343–8, Feb. 2014.

[82] S. Ichimaru. Strongly coupled plasmas: high-density classical plasmas and degenerate electron liquids. *Reviews of Modern Physics*, 54(4):1017–1059, 1982.

[83] Y. Ishida, T. Togashi, K. Yamamoto, M. Tanaka, T. Taniuchi, T. Kiss, M. Nakajima, T. Suemoto, and S. Shin. Non-thermal hot electrons ultrafastly generating hot optical phonons in graphite. *Scientific reports*, 1, 2011.

[84] R. W. James. *The Optical Principles of the Diffraction of X-rays*. G. Bell and Sons Ltd., London, 1962.

[85] T. Kluge, T. Cowan, A. Debus, U. Schramm, K. Zeil, and M. Bussmann. Electron temperature scaling in laser interaction with solids. *Physical Review Letters*, 107(20):205003, 2011.

[86] W. Kohn and L. J. Sham. Self-Consistent Equations Including Exchange and Correlation Effects. *Physical Review*, 140(4A):1133–1138, 1965.

[87] D. Kraus, J. Vorberger, D. Gericke, V. Bagnoud, A. Blažević, W. Cayzac, A. Frank, G. Gregori, A. Ortner, A. Otten, F. Roth, G. Schaumann, D. Schumacher, K. Siegenthaler, F. Wagner, K. Wünsch, and M. Roth. Probing the Complex Ion Structure in Liquid Carbon at 100 GPa. *Physical Review Letters*, 111(25):255501, Dec. 2013.

[88] A. L. Kritcher, T. Döppner, D. Swift, J. Hawreliak, G. Collins, J. Nilsen, B. L. Bachmann, E. Dewald, D. Strozzi, S. Felker, O. L. Landen, O. Jones, C. Thomas, J. Hammer, C. Keane, H. J. Lee, S. H. Glenzer, S. Rothman, D. A. Chapman, D. Kraus, P. Neumayer, and R. W. Falcone. Probing matter at Gbar pressures at the NIF. *High Energy Density Physics*, 10:27–34, 2014.

[89] A. L. Kritcher, P. Neumayer, J. Castor, T. Döppner, R. W. Falcone, O. L. Landen, H. J. Lee, R. W. Lee, E. C. Morse, A. Ng, S. Pollaine, D. Price, and S. H. Glenzer. Ultrafast x-ray Thomson scattering of shock-compressed matter. *Science*, 322(5898):69–71, Oct. 2008.

[90] S. Kurth, J. P. Perdew, and P. Blaha. Molecular and solid-state tests of density functional approximations: LSD, GGAs, and meta-GGAs. *International Journal of Quantum Chemistry*, 75:889, 1999.

[91] K. W. D. Ledingham and W. Galster. Laser-driven particle and photon beams and some applications. *New Journal of Physics*, 12:045005, 2010.

[92] H. J. Lee, P. Neumayer, J. Castor, T. Döppner, R. W. Falcone, C. Fortmann, B. A. Hammel, A. L. Kritcher, O. L. Landen, R. W. Lee, D. D. Meyerhofer, D. H. Munro, R. Redmer, S. P. Regan, S. Weber, and S. H. Glenzer. X-ray thomson-scattering measurements of density and temperature in shock-compressed beryllium. *Physical Review Letters*, 102(11):115001, 2009.

[93] R. W. Lee, D. Kalantar, and J. Molitoris. Warm Dense Matter : An Overview. *The LLNL Warm Dense Matter Workshop*, 2004.

[94] C. Leem, B. Kim, C. Kim, S. Park, T. Ohta, A. Bostwick, E. Rotenberg, H.-D. Kim, M. K. Kim, and H. Choi. Effect of Linear Density of States on the Quasiparticle Dynamics and Small Electron-Phonon Coupling in Graphite. *Physical Review Letters*, 100(1):016802, Jan. 2008.

[95] M. Ligges, I. Rajkovic, P. Zhou, O. Posth, C. Hassel, G. Dumpich, and D. von der Linde. Observation of ultrafast lattice heating using time resolved electron diffraction. *Applied Physics Letters*, 94(10):101910, 2009.

[96] Z. Lin, L. Zhigilei, and V. Celli. Electron-phonon coupling and electron heat capacity of metals under conditions of strong electron-phonon nonequilibrium. *Physical Review B*, 77(7):075133, Feb. 2008.

[97] J. D. Lindl, P. Amendt, R. L. Berger, S. G. Glendinning, S. H. Glenzer, S. W. Haan, R. L. Kauffman, O. L. Landen, and L. J. Suter. The physics basis for ignition using indirect-drive targets on the National Ignition Facility. *Physics of Plasmas*, 11(2):339, 2004.

[98] T. Ma, L. B. Fletcher, A. Pak, D. A. Chapman, R. W. Falcone, C. Fortmann, E. Galtier, D. O. Gericke, G. Gregori, J. Hastings, O. L. Landen, S. Le Pape, H. J. Lee, B. Nagler, P. Neumayer, D. Turnbull, J. Vorberger, T. G. White, K. Wünsch, U. Zastrau, S. H. Glenzer, and T. Döppner. Observations of strong ion-ion correlations in dense plasmas. *Physics of Plasmas*, 21(5):056302, 2014.

[99] A. Macchi, M. Borghesi, and M. Passoni. Ion acceleration by superintense laser-plasma interaction. *Reviews of Modern Physics*, 85(2):751–793, May 2013.

[100] T. H. Maiman. Stimulated Optical Radiation in Ruby. *Nature*, 187(4736):1048–1049, 1960.

[101] F. J. McClung and R. W. Hellwarth. Giant optical pulsations from Ruby. *Journal of Applied Physics*, 33(3):828–829, 1962.

[102] W. L. McMillan. Transition Temperature of Strong-Coupled Superconductors. *Physical Review*, 167(2):331–344, 1968.

[103] J. Meinecke, H. W. Doyle, F. Miniati, A. R. Bell, R. Bingham, R. Crowston, R. P. Drake, M. Fatenajad, M. Koenig, Y. Kuramitsu, C. C. Kuranz, D. Q. Lamb, D. Lee, M. J. MacDonald, C. D. Murphy, H.-S. Park, A. Pelka, A. Ravasio, Y. Sakawa, A. A. Schekochihin, A. Scopatz, P. Tzeferacos, W. C. Wan, N. C. Woolsey, R. Yurchak, B. Reville, and G. Gregori. Turbulent amplification of magnetic fields in laboratory laser-produced shock waves. *Nature Physics*, 10(7):520–524, 2014.

[104] B. Militzer, W. B. Hubbard, J. Vorberger, I. Tamblyn, and S. A. Bonev. A Massive Core in Jupiter Predicted from First-Principles Simulations. *The Astrophysical Journal*, 688:L45–L48, 2008.

[105] J. P. Mithen. *Molecular dynamics simulations of the equilibrium dynamics of non-ideal plasmas*. PhD thesis, University of Oxford, 2012.

[106] J. P. Mithen, J. Daligault, B. Crowley, and G. Gregori. Density fluctuations in the Yukawa one-component plasma: An accurate model for the dynamical structure factor. *Physical Review E*, 84(4):046401, Oct. 2011.

[107] J. P. Mithen, J. Daligault, and G. Gregori. Extent of validity of the hydrodynamic description of ions in dense plasmas. *Physical Review E*, 83(1):015401, Jan. 2011.

[108] J. P. Mithen, J. Daligault, and G. Gregori. Comparative merits of the memory function and dynamic local-field correction of the classical one-component plasma. *Physical Review E*, 85(5):056407, May 2012.

[109] P. Mora. Plasma expansion into a vacuum and ion acceleration. *Physical Review Letters*, 90(18):185002, 2003.

[110] A. Morace, L. Fedeli, D. Batani, S. Baton, F. N. Beg, S. Hulin, L. C. Jarrott, A. Margarit, M. Nakai, M. Nakatsutsumi, P. Nicolai, N. Piovella, M. S. Wei, X. Vaisseau, L. Volpe, and J. J. Santos. Development of x-ray radiography for high energy density physics. *Physics of Plasmas*, 21(10):102712, Oct. 2014.

[111] B. Mueller and B. Rethfeld. Relaxation dynamics in laser-excited metals under nonequilibrium conditions. *Physical Review B*, 87(3):035139, Jan. 2013.

[112] N. Nettelmann. Predictions on the core mass of Jupiter and of giant planets in general. *Astrophysics and Space Science*, 336(1):47–51, Mar. 2011.

[113] N. Nettelmann, A. Becker, B. Holst, and R. Redmer. Jupiter Models With Improved Ab Initio Hydrogen Equation of State (H-Reos.2). *The Astrophysical Journal*, 750(1):52, 2012.

[114] P. Neumayer, B. Aurand, M. Basko, B. Ecker, P. Gibbon, D. C. Hochhaus, A. Karmakar, E. Kazakov, T. Kühl, C. Labaune, O. Rosmej, A. Tauschwitz, B. Zielbauer, and D. Zimmer. The role of hot electron refluxing in laser-generated K -alpha sources. *Physics of Plasmas*, 17(10):103103, 2010.

[115] A. Ng, D. Parfeniuk, and L. DaSilva. Hugoniot measurements for laser-generated shock waves in aluminum. *Physical Review Letters*, 54(24):2604–2607, 1985.

[116] M. Nicoul, U. Shymanovich, A. Tarasevitch, D. von der Linde, and K. Sokolowski-Tinten. Picosecond acoustic response of a laser-heated gold-film studied with time-resolved x-ray diffraction. *Applied Physics Letters*, 98(19):191902, 2011.

[117] F. Nürnberg, M. Schollmeier, E. Brambrink, A. Blažević, D. C. Carroll, K. Flippo, D. C. Gautier, M. Geissel, K. Harres, B. M. Hegelich, O. Lundh, K. Markey, P. McKenna, D. Neely, J. Schreiber, and M. Roth. Radiochromic film imaging spectroscopy of laser-accelerated proton beams. *The Review of Scientific Instruments*, 80(3):033301, Mar. 2009.

[118] H. Ohta and S. Hamaguchi. Molecular dynamics evaluation of self-diffusion in Yukawa systems. *Physics of Plasmas*, 7(2000):4506, 2000.

[119] K. O'Nions, R. Pitman, and C. Marsh. Science of nuclear warheads. *Nature*, 415(6874):853–7, Feb. 2002.

[120] L. Ornstein and F. Zernike. Accidental deviations of density and opalescence at the critical point of a single substance. *Proc. Akad. Sci.*, 17:793, 1914.

[121] H.-S. Park, D. M. Chambers, H.-K. Chung, R. J. Clarke, R. Eagleton, E. Giraldez, T. Goldsack, R. Heathcote, N. Izumi, M. H. Key, J. A. King, J. A. Koch, O. L. Landen, A. Nikroo, P. K. Patel, D. F. Price, B. A. Remington, H. F. Robey, R. A. Snavely, D. A. Steinman, R. B. Stephens, C. Stoeckl, M. Storm, M. Tabak, W. Theobald, R. P. J. Town, J. E. Wickersham, and B. B. Zhang. High-energy Kα radiography using high-intensity, short-pulse lasers. *Physics of Plasmas*, 13(5):056309, 2006.

[122] H.-S. Park, N. Izumi, M. H. Key, J. A. Koch, O. L. Landen, P. K. Patel, T. W. Phillips, and B. B. Zhang. Characteristics of high energy Kα and Bremsstrahlung sources generated by short pulse petawatt lasers. *Review of Scientific Instruments*, 75(10):4048, 2004.

[123] M. Passoni, L. Bertagna, and A. Zani. Target normal sheath acceleration: theory, comparison with experiments and future perspectives. *New Journal of Physics*, 12(4):045012, Apr. 2010.

[124] P. Patel, A. J. MacKinnon, M. Key, T. Cowan, M. Foord, M. Allen, D. Price, H. Ruhl, P. T. Springer, and R. Stephens. Isochoric Heating of Solid-Density Matter with an Ultrafast Proton Beam. *Physical Review Letters*, 91(12):125004, Sept. 2003.

[125] I. J. Paterson, R. J. Clarke, N. C. Woolsey, and G. Gregori. Image plate response for conditions relevant to laserplasma interaction experiments. *Measurement Science and Technology*, 19(9):095301, Sept. 2008.

[126] Y. Ping, D. Hanson, I. Koslow, T. Ogitsu, D. Prendergast, E. Schwegler, G. Collins, and A. Ng. Broadband Dielectric Function of Nonequilibrium Warm Dense Gold. *Physical Review Letters*, 96(25):255003, June 2006.

[127] N. R. C. Plasma Science Committee. *Frontiers in High Energy Density Physics: The X-Games of Contemporary Science*. The National Academies Press, Washington, D.C., 2003.

[128] E. L. Pollock and J. P. Hansen. Statistical Mechnics of Dense Ionized Matter II. *Physical Review A*, 8(6):3110–3122, 1973.

[129] S. Ranganathan and S. Yip. Memory functions for kinetic theory models of density fluctuations in fluids. *Physica A: Statistical and Theoretical Physics*, 100(1):127–139, 1980.

[130] W. J. M. Rankine. On the Thermodynamic Theory of Waves of Finite Longitudinal Disturbance. *Philosophical Transactions of the Royal Society of London*, 160(January):277–288, 1870.

[131] C. Reich, P. Gibbon, I. Uschmann, and E. Forster. Yield optimization and time structure of femtosecond laser plasma kalpha sources. *Physical Review Letters*, 84(21):4846–9, May 2000.

[132] B. A. Remington, D. Arnett, R. P. Drake, and H. Takabe. Modeling Astrophysical Phenomena in the Laboratory with Intense Lasers. *Science*, 284(5419):1488–1493, 1999.

[133] B. Rethfeld, A. Kaiser, M. Vicanek, and G. Simon. Ultrafast dynamics of nonequilibrium electrons in metals under femtosecond laser irradiation. *Physical Review B*, 65(21):214303, May 2002.

[134] D. Riley, J. Angulo-Gareta, F. Y. Khattak, M. Lamb, P. S. Foster, E. Divall, C. Hooker, A. Langley, R. Clarke, and D. Neely. Kα yields from Ti foils irradiated with ultrashort laser pulses. *Physical Review E*, 71(1):016406, Jan. 2005.

[135] D. Riley, N. C. Woolsey, D. McSherry, I. Weaver, A. Djaoui, and E. Nardi. X-Ray diffraction from a dense plasma. *Physical Review Letters*, 84(8):1704–7, Feb. 2000.

[136] A. Rousse, P. Audebert, J. P. Geindre, F. Falliès, J. C. Gauthier, A. Mysyrowicz, G. Grillon, and A. Antonetti. Efficient \textit{K} α{} x-ray source from femtosecond laser-produced plasmas. *Physical Review E*, 50(3):2200–2207, 1994.

[137] T. Saigo and S. Hamaguchi. Shear viscosity of strongly coupled Yukawa systems. *Physics of Plasmas*, 9(4):1215–1218, 2002.

[138] E. Saldin, E. A. Schneidmiller, and M. V. Yurkov. The physics of free electron lasers. An introduction. *Physics Reports*, 260:187–327, 1995.

[139] E. L. Saldin, E. A. Schneidmiller, and M. V. Yurkov. Coherence properties of the radiation from X-ray free electron laser. *Optics Communications*, 148:383–403, 2006.

[140] K. Y. Sanbonmatsu and M. S. Murillo. Shear viscosity of strongly coupled Yukawa systems on finite length scales. *Physical Review Letters*, 86(7):1215–1218, 2001.

[141] R. Schmidt, B. J. B. Crowley, J. P. Mithen, and G. Gregori. Quantum hydrodynamics of strongly coupled electron fluids. *Physical Review E*, 85(4):046408, 2012.

[142] J. Schneider, C. Dedieu, P. Le Sidaner, R. Savalle, and I. Zolotukhin. Defining and cataloging exoplanets: The exoplanet.eu database. *Astronomy & Astrophysics*, 532(A79), 2011.

[143] R. Schoenlein, W. Lin, J. Fujimoto, and G. Eesley. Femtosecond studies of nonequilibrium electronic processes in metals. *Physical Review Letters*, 58(16):1680–1683, Apr. 1987.

[144] V. Schwarz, B. Holst, T. Bornath, C. Fortmann, W.-D. Kraeft, R. Thiele, R. Redmer, G. Gregori, H. J. Lee, T. Döppner, and S. H. Glenzer. Static ion structure factor for dense plasmas: Semi-classical and ab initio calculations. *High Energy Density Physics*, 6(3):305–310, 2010.

[145] J. Sheffield. *Plasma Scattering of Electromagnetic Radiation*. Academic Press, New York, 1975.

[146] R. Snavely, M. Key, S. Hatchett, T. Cowan, M. Roth, T. Phillips, M. Stoyer, E. Henry, T. Sangster, M. Singh, S. Wilks, A. MacKinnon, A. Offenberger, D. Pennington, K. Yasuike, A. Langdon, B. Lasinski, J. Johnson, M. Perry, and E. Campbell. Intense High-Energy Proton Beams from Petawatt-Laser Irradiation of Solids. *Physical Review Letters*, 85(14):2945, Oct. 2000.

[147] D. K. Spaulding, R. S. McWilliams, R. Jeanloz, J. H. Eggert, P. M. Celliers, D. G. Hicks, G. W. Collins, and R. F. Smith. Evidence for a phase transition in silicate melt at extreme pressure and temperature conditions. *Physical Review Letters*, 108(6):065701, 2012.

[148] L. Spitzer. *Physics of Fully Ionized Gases*. Interscience, New York, 1962.

[149] J. C. Stewart and K. D. Pyatt. Lowering of Ionization Potentials in Plasmas. *Astrophys. J.*, 144:1203, 1966.

[150] D. Strickland and G. Mourou. Compression of Ampified Chirped Optical Pulses. *Optics Communications*, 55(6):447–449, 1985.

[151] K. Sugawara, T. Sato, S. Souma, T. Takahashi, and H. Suematsu. Anomalous quasiparticle lifetime and strong electron-phonon coupling in graphite. *Physical Review Letters*, 98(1):036801, 2007.

[152] D. C. Swift and R. P. Johnson. Quasi-isentropic compression by ablative laser loading : Response of materials to dynamic loading on nanosecond time scales. *Physical Review E*, 71(6):066401, 2005.

[153] D. C. Swift and R. G. Kraus. Properties of plastic ablators in laser-driven material dynamics experiments. *Physical Review E*, 77(6):066402, 2008.

[154] D. C. Swift, T. E. Tierney, R. A. Kopp, and J. T. Gammel. Shock pressures induced in condensed matter by laser ablation. *Physical Review E*, 69(3):036406, 2004.

[155] A. C. Thompson. *X-ray Data Booklet*. Lawrence Berkeley National Laboratory, Berkeley, California, 3rd edition, 2009.

[156] T. Togashi, E. J. Takahashi, K. Midorikawa, M. Aoyama, K. Yamakawa, T. Sato, A. Iwasaki, S. Owada, T. Okino, K. Yamanouchi, F. Kannari, A. Yagishita, H. Nakano, M. E. Couprie, K. Fukami, T. Hatsui, T. Hara, T. Kameshima, H. Kitamura, N. Kumagai, S. Matsubara, M. Nagasono, H. Ohashi, T. Ohshima, Y. Otake, T. Shintake, K. Tamasaku, H. Tanaka, T. Tanaka, K. Togawa, H. Tomizawa, T. Watanabe, M. Yabashi, and T. Ishikawa. Extreme ultraviolet free electron laser seeded with high-order harmonic of Ti:sapphire laser. *Optics express*, 19(1):317–324, 2011.

[157] M. Torrent, F. Jollet, F. Bottin, G. Zérah, and X. Gonze. Implementation of the projector augmented-wave method in the ABINIT code: Application to the study of iron under pressure. *Computational Materials Science*, 42(2):337–351, Apr. 2008.

[158] L. van Hove. Correlations in Space and Time Approximation Scattering in Systems of Interacting Particles. *Physical Review*, 95(1):246–262, 1954.

[159] J. Vorberger, Z. Donkó, I. M. Tkachenko, and D. Gericke. Dynamic Ion Structure Factor of Warm Dense Matter. *Physical Review Letters*, 109(22):225001, Nov. 2012.

[160] J. Vorberger and D. Gericke. Comparison of electronion energy transfer in dense plasmas obtained from numerical simulations and quantum kinetic theory. *High Energy Density Physics*, 10:1–8, Mar. 2014.

[161] J. Vorberger and D. O. Gericke. Coupled mode effects on energy transfer in weakly coupled, two-temperature plasmas. *Physics of Plasmas*, 16(8):082702, 2009.

[162] J. Vorberger, D. O. Gericke, T. Bornath, and M. Schlanges. Energy relaxation in dense, strongly coupled two-temperature plasmas. *Physical Review E*, 81(4):046404, 2010.

[163] X. Wang, D. Riffe, Y.-S. Lee, and M. Downer. Time-resolved electron-temperature measurement in a highly excited gold target using femtosecond thermionic emission. *Physical Review B*, 50(11):8016, Sept. 1994.

[164] B. E. Warren. *X-ray Diffraction*. Addison-Wesley, Reading, MA, 1969.

[165] S. White, G. Nersisyan, B. Kettle, T. W. J. Dzelzainis, K. McKeever, C. L. S. Lewis, A. Otten, K. Siegenthaler, D. Kraus, M. Roth, T. G. White, G. Gregori, D. O. Gericke, R. Baggott, D. A. Chapman, K. Wünsch, J. Vorberger, and D. Riley. X-ray scattering from warm dense iron. *High Energy Density Physics*, 9(3):573–577, Sept. 2013.

[166] T. G. White. *Study of High Energy Density Matter through Quantum Molecular Dynamics and Time Resolved X-ray Scattering*. PhD thesis, University of Oxford, 2015.

[167] T. G. White, N. Hartley, B. Borm, B. Crowley, J. Harris, D. Hochhaus, T. Kaempfer, K. Li, P. Neumayer, L. K. Pattison, F. Pfeifer, S. Richardson, A. P. L. Robinson, I. Uschmann, and G. Gregori. Electron-Ion Equilibration in Ultrafast Heated Graphite. *Physical Review Letters*, 112(14):145005, Apr. 2014.

[168] T. G. White, P. Mabey, D. O. Gericke, N. J. Hartley, H. W. Doyle, D. Mcgonegle, D. Rackstraw, A. Higginbotham, and G. Gregori. Electron-ion equilibration in laser heated gold films. *Physical Review B*, 90(1):014305, 2014.

[169] T. G. White, S. Richardson, B. Crowley, L. K. Pattison, J. Harris, and G. Gregori. Orbital-Free Density-Functional Theory Simulations of the Dynamic Structure Factor of Warm Dense Aluminum. *Physical Review Letters*, 111(17):175002, Oct. 2013.

[170] T. G. White, J. Vorberger, C. R. D. Brown, B. J. B. Crowley, P. Davis, S. H. Glenzer, J. W. O. Harris, D. C. Hochhaus, S. Le Pape, T. Ma, C. D. Murphy, P. Neumayer, L. K. Pattison, S. Richardson, D. O. Gericke, and G. Gregori. Observation of inhibited electron-ion coupling in strongly heated graphite. *Scientific reports*, 2, Nov. 2012.

[171] E. P. Wigner and F. Seitz. On the Constitution of Metallic Sodium. *Physical Review*, 43:804–810, 1933.

[172] K. Wünsch, J. Vorberger, and D. O. Gericke. Ion structure in warm dense matter: Benchmarking solutions of hypernetted-chain equations by first-principle simulations. *Physical Review E*, 79(1):010201, 2009.

[173] K. Wünsch, J. Vorberger, G. Gregori, and D. O. Gericke. Ion structure in dense plasmas: MSA versus HNC. *Journal of Physics A*, 42(21):214053, May 2009.

[174] U. Zastrau, P. Sperling, A. Becker, T. Bornath, R. Bredow, T. Döppner, S. Dziarzhytski, T. Fennel, L. Fletcher, E. Förster, C. Fortmann, S. H. Glenzer, S. Göde, G. Gregori, M. Harmand, V. Hilbert, B. Holst, T. Laarmann, H. J. Lee, T. Ma, J. P. Mithen, R. Mitzner, C. D. Murphy, M. Nakatsutsumi, P. Neumayer, A. Przystawik, S. Roling, M. Schulz, B. Siemer, S. Skruszewicz, J. Tiggesbäumker, S. Toleikis, T. Tschentscher, T. G. White, M. Wöstmann, H. Zacharias, and R. Redmer. Equilibration dynamics and conductivity of warm dense hydrogen. *Physical Review E*, 90(1):013104, July 2014.

[175] U. Zastrau, P. Sperling, M. Harmand, A. Becker, T. Bornath, R. Bredow, S. Dziarzhytski, T. Fennel, L. B. Fletcher, E. Förster, S. Göde, G. Gregori, V. Hilbert, D. C. Hochhaus, B. Holst, T. Laarmann, H. J. Lee, T. Ma, J. P. Mithen, R. Mitzner, C. D. Murphy, M. Nakatsutsumi, P. Neumayer, A. Przystawik, S. Roling, M. Schulz, B. Siemer, S. Skruszewicz, J. Tiggesbäumker, S. Toleikis, T. Tschentscher, T. G. White, M. Wöstmann, H. Zacharias, T. Döppner, S. H. Glenzer, and R. Redmer. Resolving ultrafast heating of dense cryogenic hydrogen. *Physical Review Letters*, 112(10):105002, 2014.

[176] J. Zhu and P. Ji. Dispersion relation and Landau damping of waves in high-energy density plasmas. *Plasma Physics and Controlled Fusion*, 54:065004, 2012.

[177] J. M. Ziman. *Electrons and Phonons*. Oxford University Press, Oxford, 1960.

[178] R. Zimmermann. Dynamical Screening and Self-Energy of Excitons. 175:175–187, 1978.